Terrestrial Laser Scanning for Forest Inventories

Dissertation
zur
Erlangung der naturwissenschaftlichen Doktorwürde
(Dr. sc. nat.)
vorgelegt der
Mathematisch-naturwissenschaftlichen Fakultät
der
Universität Zürich

von
Meinrad Abegg
von
Küsnacht ZH

Promotionskommission
Prof. Dr. Michael E. Schaepman
(Vorsitz der Dissertation)
Dr. Felix Morsdorf (Leitung der Dissertation)
Dr. Ruedi Bösch
Prof. Dr. Ross Purves

Zürich, 2020

Summary

Forest inventories are an essential instrument for forest monitoring worldwide. They deliver information on forests for political, practical or research applications on the national and international level. Fieldwork still provides the most important collection of data for these monitoring projects where precise and reproducible measurements are crucial. The rapid methodological and technological development of portable terrestrial laser scanning devices and their applications in the context of forest inventories in recent years, lead to the question whether they can be used for national forest inventories (NFI), e.g., in Switzerland, to improve their informative value, especially where direct measurements are very expensive or impossible. Terrestrial laser scanning (TLS) is now well established and laser - object interactions have been studied using theoretical, modelling and experimental approaches. Still, little is known on the influence of TLS scan and survey properties on point clouds in complex scattering environments such as forests. However, the understanding of new potential measurements is paramount for an implementation in the NFI workflow.

In this thesis, we used an open source 3D software package to simulate forest environments to different levels of abstraction. We examined three state-of-the-art terrestrial laser scanners and implemented the observed behaviour in terms of signal triggering in our simulation environment. NFI sample plot data was used to derive parameters to describe various diameter distributions allowing the analysis of TLS properties in a horizontal view. Additionally, tree dimensions and their locations on sample plots were used so simulate 3D forest environments with varying understorey densities. In these environments, simulated laser scanning from five positions was performed, which enabled us to investigate single and multiple scan point clouds.

In the first study, we show that mostly the tree density in addition with Weibull shape parameter, describing a stand, and the mean diameter of the dominant 100 trees per hectare, have a significant and relevant influence on the visibility of the sample plot. Furthermore, we show the effectiveness and the efficiency of 40 scanner location patterns. The most efficient scanner location in terms of visibility is the centre of the sample plot. If multiple locations are used, our results show that an even distribution of the scanner locations over the sample plot, with even distances to the edge of the sample plot and to other scanner locations, delivers the best visibility for deriving properties of the stand. A local adjustment of the scanner location considering the surrounding trees could contribute to an even better visibility.

In the second study within this thesis, we analysed three laser scanners, which revealed various effects of signal triggering, when a laser pulse intersects with multiple objects (edge or mixed pixel effects). These effects are prefiltering of points based on ambiguous echoes, distance deviation patterns at edges of objects, lacking separation of objects and triggering of multiple points per range measurement. The

simulation of horizontal scans in stands with 684 different tree diameter distributions and tree densities reveals the extent of the influence of laser beam diameter and signal triggering approach on point cloud quality. The main implications are that objects with “small” diameters can hardly be depicted by TLS in a reasonable way since they are either not visible in the point cloud, they are represented by very few echoes and/or they are subject to severe measurement errors due to edge effects. The actual threshold for “small” depends on the objective of the TLS application and the used point cloud evaluation algorithms.

In a third study within this thesis, we demonstrate a simulation workflow to evaluate TLS for forest inventories on the basis of 18 sample plots with a total of 102 sample trees under different scanning circumstances. We can show that the volume estimation from point clouds are biased throughout. Especially small tree parts with diameters < 7 cm are lacking a precise estimation. For the implemented scanning system with prefiltering and edge noise, we could not find an influence of the understorey. However, multiple scanning leads to higher variation of the applied quantitative structure models (QSM), possibly due to additional edge noise from multiple scanning perspectives.

This thesis shows the potential of simulations to evaluate TLS applications for forest inventories. With simulations, we could prove that small objects can not be measured appropriately with TLS and that interactions between scanner placement, stand properties, TLS device, and point cloud evaluation routines can be investigated and understood. We could point out open issues to be cleared before TLS can be integrated in the common Swiss NFI workflow.

Zusammenfassung

Waldinventuren haben sich weltweit als wichtiges Intrument der Waldbeobachtung etabliert. Sie liefern Informationen über Wälder für politische, praktische, aber auch forschungsorientierte Anwendungen auf nationaler und internationaler Ebene. Feldaufnahmen liefern nach wie vor den grössten und wichtigsten Teil der Daten für diese Monitoringprojekte, bei denen genaue und reproduzierbare Messungen von höchster Wichtigkeit sind. Die jüngsten methodischen und technologischen Fortschritte bei tragbaren terrestrischen Laserscannern und ihren Anwendungsmöglichkeiten im Bereich von Waldinventuren, führen zur Frage, ob diese Geräte für nationale Waldinventuren, z.B. dem Schweizerischen Landesforstinventar (LFI), verwendet werden können, um deren Aussagekraft zu verbessern, insbesondere, wo direkte Messungen sehr teuer oder unmöglich sind. Terrestrisches Laserscanning (TLS) ist mittlerweile eine etablierte Technologie und Laser-Objekt-Interaktionen wurden mittels theoretischen, modellbasierten und experimentellen Ansätzen verschiedentlich untersucht. Dennoch ist bisher wenig über den Einfluss von Scanner- und Aufnahmedesign auf die Punktwolken, generiert in komplexen Umgebungen, wie Wäldern, bekannt. Für eine nationale Waldinventur ist es jedoch überaus wichtig, dass neue Messansätze im Detail verstanden werden, bevor sie in reguläre Feldaufnahmen integriert werden.

In dieser Dissertation haben wir eine open-source 3D Software benutzt, um waldähnliche Umgebungen, in verschiedenen Abstraktionsleveln, zu simulieren. Wir haben drei dem aktuellen Stand der Technik entsprechenden Laserscanner untersucht und haben das beobachtete Verhalten bezüglich Auslösung eines Signals (eines Punktes der Punktwolke) in einer Simulationsumgebung implementiert. Ausserdem haben wir Stichprobendaten verwendet, um Bestandesparameter, welche die Durchmesserverteilung und Stammzahl beschreiben, abzuleiten. Diese konnten benutzt werden, um das Verhalten von TLS bei einem horizontalen Scan zu studieren. Des Weiteren haben wir die Baumdurchmesser und genauen Baumstandorte auf den Probeflächen benutzt, um dreidimensionale Waldprobeflächen mit unterschiedlichen Deckungsgraden in der Unterschicht zu simulieren. In diesen simulierten Umgebungen, konnte Laserscanning auf jeweils fünf verschiedenen Positionen und Kombinationen davon untersucht werden.

In der ersten Studie haben wir gezeigt, dass vor allem die Stammzahl und zusätzlich ein die Form der Durchmesserverteilung beschreibender Parameter, sowie der Durchmesser der dominanten 100 Bäume pro Hektare einen signifikanten und relevanten Einfluss auf die Sichtbarkeit einer Probefläche haben. Ausserdem konnten wir die Effizienz und den Zusatznutzen von 40 verschiedenen Scanneraufstellungen, kombiniert aus mehreren Scannerpositionen, aufzeigen. Werden mehrere Scannerpositionen kombiniert, so liefern gleichmässig verteilte Scannerpositionen mit ähnlichen Abständen zueinander und zum Rand der Probefläche die besten Resultate bezüglich Sichtbarkeit der Probefläche. Eine lokale Verschiebung von einzelnen Scannerposi-

tionen unter Berücksichtigung der benachbarten Bäume kann zu einer zusätzlichen Verbesserung der Sichtbarkeit der Probefläche beitragen.

In der zweiten Studie dieser Dissertation haben wir drei Laserscanner analysiert. Diese brachten verschiedene Effekte der Signalauslösung, wenn ein Laserpuls mehrere Objekte schneidet, zu Tage. Diese Effekte sind Vorfilterung von LiDAR Punkten basierend auf unklaren LiDAR Echos, Distanzabweichung an Kanten von Objekten, fehlende Trennung von Objekten und Auslösung von mehreren Punkten. Die Simulation von horizontalen Scans in Beständen mit 684 unterschiedlichen Durchesserverteilungen und Stammzahlen haben den Einfluss von Laserstrahldurchmesser und Art der Auslösung von Punkten auf die Qualität von Punktwolken gezeigt. Das wichtigste Fazit aus diesen Simulationen ist, dass kleine Objekte kaum in einer sinnvollen Weise von einem Laserscanner abgebildet werden können. Der Grund dafür ist, dass sie entweder überhaupt nicht in der Punktwolke sichtbar sind oder durch sehr wenige Punkte repräsentiert werden und/oder wegen Kanteneffekten starken Messfehlern unterliegen. Die Grenze jedoch, was als “zu klein“ gilt, hängt stark von den Zielen der TLS Anwendung und den verwendeten Methoden ab.

In einer dritten Studie im Rahmen dieser Dissertation stellen wir eine Vorgehensweise vor, um TLS für Waldinventuren zu simulieren. Dazu wurden 18 Probeflächen mit total 102 Probebäumen unter verschiedensten Scanszenarien simuliert. Wir konnten aufzeigen, dass die Volumenschätzung, basierend auf TLS Punktwolken, durchwegs mit einem Bias behaftet sind. Besonders kleine Baumteile mit einem Durchmesser < 7 cm lassen eine präzise Volumenschätzung vermissen. Der Unterwuchs hingegen hatte bei dem in diesem Versuch angewendeten TLS System (Vorfilterung und Kantenrauschen) keinen Einfluss auf die Volumenschätzung. Interessanterweise führte jedoch die Kombination von Punkten aus mehreren Scannerpositionen zu mehr Variabilität der Volumenschätzung. Dies könnte an zusätzlichem Kantenrauschen aus den unterschiedlichen Perspektiven der kombinierten Scannerpositionen liegen.

Diese Dissertation zeigt das Potential von Simulationen zur Evaluation von TLS Anwendungen für Waldinventuren auf. Mittels Simulationen konnten wir zeigen, dass kleine Objekte mit TLS nicht befriedigend gemessen werden können und dass Interaktionen zwischen Scannerplatzierung, Bestandeseigentschaften, TLS-Geräten und Point-Cloud Auswerteroutinen untersucht und verstanden werden können. Wir konnten auf verschiedene offene Probleme hinweisen, die vor einer Einbindung von TLS in die Feldaufnahmen des Schweizerischen Landesforstinventars geklärt werden müssen.

Table of Contents

List of Abbreviations

2D	Two Dimensional
3D	Three Dimensional
CPU	Central Processing Unit
DBH	Diameter at Breast Height
DTM	Digital Terrain Model
FWHM	Full Width at Half Maximum
GIS	Geographical Information System
LFI	Landesforstinventar, nationale Waldinventur
LiDAR	Light Detection And Ranging
NFI	National Forest Inventory
QSM	Quantitative Structure Model/Modelling
RANSAC	Random Sample Consensus
TLS	Terrestrial Laser Scanning
WSL	Swiss Federal Institute for Forest, Snow and Landscape Research

Chapter

1

Introduction

1.1 Forest inventories: possibilities and limitations

National forest inventories (NFI) deliver information on the forest area, the amount and change of forest resources, the development of the biotope forest in general, additionally the carbon balance of a country (FOREST EUROPE, 2015; MacDicken *et al.*, 2016; Pan *et al.*, 2011) and other ecosystem services (Shvidenko *et al.*, 2005). In the Swiss NFI, the data collection is based on aerial interpretation, forest service interviews and field measurements (Brassel & Lischke, 2001). Field measurements provide the largest and most important collection of data for an NFI. On a national level they comprise measurements of several thousand sample plots, in Switzerland over 6 500, of which each has to be visited by a field team (Tomppo *et al.*, 2010).
Since direct measurement of all roughly 500 million trees in Swiss forests would take huge effort (Lanz *et al.*, 2019), statistical sampling is applied, to obtain the needed information most efficiently. Hence, the number of sample plots is based on the objective to estimate forest area and volume with a precision of 0.5 % (relative standard error) (Brändli & Hägeli, 2019). The idea of the statistical sampling is to eliminate selection bias by random sampling (Särndal *et al.*, 2003). Therefore, the sample plots are distributed on a regular grid over the country area of Switzerland and methods for measuring are applicable on all accessible forest sample plots equally.
The standard error serves as measure for the precision of the estimation. Assuming the target variable, e.g., stem number, can be measured without bias, the standard error provides a measure for the variation of the target variable, in case of independent repetitions of the same forest inventory. Hence, the standard error describes the uncertainty of the estimation, answering the question “in what range lies the true value with what probability”.
Tree volume, is one of the most important target variables, besides stem number and forest area. Tree volume describes the forest in terms of economical values as well as breeding/feeding material for forest dwelling animals, plants and fungi. Furthermore tree volume is very closely connected to tree biomass which draws more and more attention in the discussion of climate change. However, unlike stem number and forest area, which are perfectly measurable under almost any forest conditions, tree volume can not be measured directly without destructive sampling, which is additionally connected to very high measuring costs per tree.
Individual tree volume is usually estimated by means of volume equations, respectively mathematical models (Brassel & Lischke, 2001). In Switzerland these models use tree diameter, tree species and site parameters as input variables. The inherent problem of this approach are a possible model bias and an underestimation of the true variability, since models are usually smoothed compared to true values. In the Swiss NFI this problem is tackled with a two stage approach (Mandallaz, 2006). Its concept is to measure a sub-sample of the tally trees more intensively, i.e. additionally measuring an upper diameter at 7 m above ground and tree height. Based on these

three variables the volume of the stem, which usually is of a conical shape, can be calculated with a very high precision ($R^2 > 98.7$) (Brassel & Lischke, 2001). Due to the high precision, this three-variable volume is assumed to represent (nearly) the true volume of the tree stem. Based of this assumption, the deviation between the three-variable volume and the normal volume model can be used, by means of weighting, to estimate a bias free tree volume in an area of interest. The variation (standard error) of this two stage estimate is usually higher, since the variability of the underlying sample is higher than the smoothed model values. Nevertheless this higher standard error reflects (nearly) true variability.
There are two drawbacks on this approach, even though being the best method available so far. One is that the three-variable tree stem volume is not precisely the true stem volume. However, model performance is very high (nearly perfect), since the tree stem has a relatively simple shape and hence, is easy to describe with few parameters. The second drawback is that the total tree volume, needed e.g., for biomass estimation, is far more complex, making the prediction of branch wood far more prone to unexplained variation (Herold *et al.*, 2019). Moreover, models for total tree volume (including branches) are based on destructively sampled trees from experimental sites, not completely representative for the whole of Switzerland. Hence, estimates for total tree volume or biomass have a clear potential for improvements.
As Morsdorf *et al.* (2018), Calders *et al.* (2015) and Wilkes *et al.* (2017) point out, terrestrial laser scanning (TLS) has the potential to retrieve detailed and precise information on complete trees. Hence, TLS might provide an approach to measure tree volume directly on NFI sample plots.

1.2 Terrestrial laser scanning for forest inventories: state of current research

The application of terrestrial laser scanning (TLS) for forestry applications is visible in literature since 2003 (Simonse *et al.*, 2003). Since then, a wide range of procedures and approaches were presented, some of the algorithms are even freely available. The workflow for a TLS application to estimate tree volume in an NFI comprises of the following steps: Derivation of a digital terrain model (DTM), identification of trees, respectively the segmentation of point clouds of a forest stand with semantic labelling into single tree point clouds, derivation of classical inventory parameters for allometric volume equations or derivation of tree architecture including a volume estimation. The following sections point out the current state of research in these fields of processing point clouds.

1.2.1 Derivation of a digital terrain model (DTM)

For a proper identification of trees from point clouds the terrain of the forest must be known. Therefore, the first step of point clouds processing is to derive a digital terrain model (DTM), mostly by triangulating "lowest" points identified as follows. Simonse *et al.* (2003); Aschoff & Spiecker (2004); Aschoff *et al.* (2004); Thies *et al.* (2006) and similarly Cabo *et al.* (2018) define a 0.5 x 0.5 m horizontal raster of the point cloud and use the lowest z-value as the height of that raster cell. To exclude outliers the authors define a maximal slope to neighbouring raster cells and exclude cells lying above a specific angle over the scanner position. Othmani *et al.* (2011) follow a similar approach, additionally checking the number of points per square metre, whereas Yang *et al.* (2013) exclude outliers using a RANSAC algorithm. Bienert *et al.* (2006) and Maas *et al.* (2008) analyse the density distribution within horizontal raster cells of the point cloud and assume the terrain height of each cell as the peak of the vertical point distribution after a neighbourhood consistency check. Kelbe *et al.* (2012) run a moving window over the point cloud finding local minima. Outliers are plotwise excluded considering a maximal slope.

1.2.2 Tree identification and point cloud segmentation

Identification of trees, enabling a semantic labelling of the point cloud of forest stands into single tree point clouds, is the preceding step for individual tree volume calculations.
Simonse *et al.* (2003), and similar Tansey *et al.* (2009) or Seidel *et al.* (2013), extract a 0.1 m slice from the point cloud at a height of 1.3 m above the DTM. This point cloud slice is transformed to a 1 cm horizontal raster. Trees are detected by applying a Hough transform (Hough, 1962), searching for circle like structures in the raster. Aschoff & Spiecker (2004) and Aschoff *et al.* (2004) refined this procedure by including additional point cloud slices, evaluating neighbouring relations. Bienert *et al.* (2006) first identify connected clusters of raster cells, which are used as input for a Hough transform. Additional information on the quality of the circle fit are used to decide on tree presence or absence in the respective cluster. Wezyk *et al.* (2007) identify trees from similar clusters by analysing the angle and distance relation to the respective cluster centre. Schilling *et al.* (2011) and similarly Heinzel & Huber (2017a) or Cabo *et al.* (2018) analyse the vertical connection of voxels containing a minimal number of points. The tree points, identified that way, are used to fit circles using Hough transform or a nonlinear least squares approach.
Othmani *et al.* (2011) identify clusters of points in horizontal layers to fit circles with a least square fit and compare these to circles from layers above. If vertically subsequent circles show a similar horizontal extent they are connected. This procedure has the potential to extract simple tree architecture, but is presented as an approach to identify trees (at a mean rate of 90 %). Liang & Hyyppä (2013), Liang *et al.* (2012) and Liang *et al.* (2014) analyse the spatial properties (eigenvectors and eigenvalues)

of points within their neighbourhoods. Tree stem points are identified if their normal vector points in a horizontal direction and if the local distribution of points is very low. Circles are fitted into these stem points.
Burt *et al.* (2018) present an open-source software utilising generic point cloud processing approaches to segment point clouds of large forest stands into single trees. The approaches include techniques like Euclidean clustering, principal component analysis, region-based segmentation, shape fitting and connectivity testing. Heinzel & Huber (2018) describe an approach to segment trees from stand point clouds in difficult forest situations (concerning TLS applications). The approach consists of morphological detection of tree stems, the construction of a similarity graph and the computation of a weighted eigenspectrum labelling of tree point clouds in a Markov random field framework.

1.2.3 Classical inventory parameters for allometric volume equations

The derivation of classical inventory parameters on trees, such as diameter at breast height (DBH) and tree height, from TLS point clouds enable the use of conventional allometric equations to estimate the tree volume.
Many authors (Simonse *et al.*, 2003; Aschoff & Spiecker, 2004; Hopkinson *et al.*, 2004; Tansey *et al.*, 2009; Bienert *et al.*, 2006; Kelbe *et al.*, 2012; Seidel *et al.*, 2012; Liang & Hyyppä, 2013; Seidel *et al.*, 2013; Heinzel & Huber, 2017b; Cabo *et al.*, 2018) derive the DBH from fitted circles or cylinders in the point cloud or a derived 2D or 3D raster. Wezyk *et al.* (2007) derive the DBH from the basal area (intersection area at the height of 1.3 m) of the tree. They calculate basal area by weighting the ratio of the visible basal area (the part of the basal area within the TLS points on the tree surface and the tree centre from a horizontal slice of the point cloud). Yao *et al.* (2011), Lovell *et al.* (2011) and Yang *et al.* (2013) consider the horizontal viewing angle of the trunk's edges, acquired with a full waveform terrestrial laser scanner. Kiraly & Brolly (2010) compare different approaches of diameter estimations, besides circle fitting a "free form polygon determination" is evaluated, which turns out to be more robust and flexible than the others.
Tree height is derived from the difference between the lowest point of the ground (DTM) under the tree and the highest point from the tree point cloud, as presented by various authors (Hopkinson *et al.*, 2004; Bienert *et al.*, 2006; Yang *et al.*, 2013; Liang & Hyyppä, 2013).

1.2.4 Quantitative structure modelling (QSM)

The derivation of tree architecture accompanied with volume estimation has the potential to provide detailed information on the shape and the volume distribution within a tree. We refer to this approach here as quantitative structure modelling (QSM) (Calders *et al.*, 2015). Most of the approaches derive the tree architecture which can be used to control cylinder fitting, spline fitting or, in case tree parts are

regularly covered with TLS points, to triangulate the surface of the tree.
Many approaches comprise a step of converting the point cloud to voxels (Gorte & Pfeifer, 2004; Gorte & Winterhalder, 2004), octree cells or cover sets (Raumonen *et al.*, 2013; Hackenberg *et al.*, 2014). Bienert *et al.* (2014) use the voxel information to directly derive a volume by summing up the further processed voxels. Other authors (e.g. Bucksch *et al.*, 2010; Bucksch & Lindenbergh, 2008; Gorte & Pfeifer, 2004; Gorte & Winterhalder, 2004; Gatziolis *et al.*, 2010; Côté *et al.*, 2011) apply a graph/shortest path approach or analyse connected components to derive a tree skeleton after some intermediate steps. Raumonen *et al.* (2013) or Bremer *et al.* (2013) on the other hand, analyse the shape of point groups describing a similar structure (e.g., with eigenvalues), which can be iteratively connected to a complete tree architecture.

1.3 Evaluation approaches of TLS tree volume estimations

There are two ways of validating TLS based tree volume estimations: destructive sampling and simulation. For a volume measurement the method of water displacement would deliver precise information on the tree volume. If a tree can be weighed, its biomass can directly be deduced, once the water content of the tree is known and if the wood density is available as well, the volume could be calculated. However, for both methods, trees have to be cut down, whereas the measurement involves large machinery in case of "normal" size trees. If additionally the volume/biomass distribution within the tree is of interest, labour-intensive work is needed as well. Several authors describe such approaches, e.g., Calders *et al.* (2015) harvested a total of 75 eucalyptus trees and weighed them in addition to sample wood density and water content. But as the authors state, destructive sampling can only be conducted on a limited basis. A similar approach was followed by Holopainen *et al.* (2011) and Hauglin *et al.* (2013) who sampled 20 respectively 39 trees. Astrup *et al.* (2014) sampled a total of over 2000 trees, mostly spruce, pine and birch, in Norway to compare stem volume, estimated by TLS, allometric equations and harvester weighing. If stands are accessible for harvesters and trees are suitable to be harvested in such a way, this can be an efficient option to sample trees for TLS validation. As for water displacement, Seidel *et al.* (2011) and Keightley & Bawden (2010) measured beech saplings or winegrapes by submerging parts of the plants in water tubs. However the total plant volume in both approaches was very low and far below a fully grown adult tree.
Saarinen *et al.* (2017) describe a third approach to measure the volume of trees: section-wise measurements, in which the diameter of a tree is measured along the stem and branches in specific step sizes. This approach was commonly used to develop allometric equations for allometric volume models in NFIs (e.g. Brassel & Lischke, 2001). However, as Saarinen *et al.* (2017) point out, this approach is used

to fit cubic splines depicting the shape of the tree stem. Hence, it can not handle stem shape irregularities, such as knobs. Additionally the section-wise measurement does not cover the whole tree, but e.g., cross-wise calliper measurements in steps of a specific distance, e.g., 0.1 m. Therefore, these measurements will not provide a true volume, but an (unknown) approximation of it.
Another approach to evaluate TLS volume estimations is simulation. It has the potential to overcome the drawbacks of heavy machinery, tedious manual measurement or the lack of a real ground truth. Many LiDAR simulation platforms are described in literature (e.g. Lovell *et al.*, 2005; Lewis, 1999; Van der Zande *et al.*, 2008; Gastellu-Etchegorry *et al.*, 2015; Kukko & Hyyppä, 2007). However, most of these approaches are focussed on airborne LiDAR with its specific problems. Nevertheless, some authors (e.g. Disney *et al.*, 2012; Binney & Sukhatme, 2009), simulate TLS of one tree (respectively tree part) to validate approaches of tree reconstruction from TLS tree point clouds.

1.4 Terrestrial laser scanning for forest inventories: challenges

Forest inventories rely on a representative sample of forest sample plots to infer their estimates (see section 1.1). The condition for estimations, based on statistical sampling, is that the whole sample can be measured equally, or, based on the work of Horvitz & Thompson (1952), that the selection probability for each measured individual has to be known in advance. A not measured fraction of the sample leads to possibly biased estimate on the whole population of interest (e.g., trees). Thus applications of TLS for forest inventories have to be applicable on all sample plots in the same way. As for the measurement itself, it has to be bias-free as well, whereas the precision (the variation) of the measurement has no influence on the bias of the estimate, but on the standard error. Nevertheless, for a national forest inventory, with the pretension to deliver objective and "true" information on forests for policy and scientific purposes, it is indispensable to rely on unbiased measurements of a complete statistical sample.
For the estimation of tree number (e.g., by diameter and tree species), this is already possible, since measurements with calliper and measuring tape are highly reliable under any forest condition, delivering unbiased measurements. However, as pointed out in section 1.1 the estimation of tree volume needs a closer look, since tree volume can not be measured directly with traditional tools. Using models, a certain amount of uncertainty, and hence possible bias, remains. As for stem volume (volume of the main tree axis), the model performance is so high, that improvements are hard to achieve and existing biases due to model application might be irrelevant. As stated in section 1.1 new measurement approaches, such as terrestrial laser scanning could improve the estimation of total tree volume/biomass, since tree volume models lack

a comparable performance as for stem volume. Nevertheless, the accuracy (bias) and the precision (variability) of the TLS volume estimation, which is a volume model as well, has to be understood in detail, to quantify estimates based on it. Both bias and variability can arise at different steps of the TLS volume estimation: TLS device, measurement setup, point cloud segmentation in to tree point clouds, choice of quantitative structure model and their starting parameters. Whereas for the statistical estimators, their influence on the precision is known (Mandallaz, 2006). As other authors point out (e.g. Saarinen *et al.*, 2017) too, TLS applications for forest inventories have to be understood in terms of their behaviour on accuracy and precision on specific target variables (e.g., tree volume), before integration in NFI campaigns.

1.5 Thesis aims and structure

The aim of this thesis is to understand the interaction of forest stands, data acquisition with terrestrial laser scanning (TLS) and volume estimation when applying TLS in forest inventories. This research goal leads to the following three main research questions.

1.5.1 Research questions

In this thesis, we address the following three research questions:

> *1) How do the properties of a forest stand, the placement of the laser scanner and the combination of scanner placements influence the technically unblocked observable area of a sample plot?*

In Swiss forests, a wide range of stand properties can be encountered. This research question aims at understanding the influence of stand properties, namely its tree diameter distribution and tree density, on the area of a sample plot, that is unobstructedly visible from possible scanner locations. Further the influence of the scanner placement and the combination of scanner locations should be investigated. Using sample plot information from the Swiss NFI, we defined virtual sample plots with cylinders as proxy for sample trees. A horizontal high resolution scan in combination with a voxel traversal algorithm allowed us to assess the horizontal visibility on the simulated sample plots. As a side-product of this implementation, we derived a model to calculate the number of possible points on an object of a specific size, placed in any location within a 50 x 50 x 50 m cube around the scanner. The findings support decisions on suitable scanner placement patterns for TLS measurements in forest inventories.

> *2) How do laser scanners handle echoes from multiple objects and what is the influence of such echo-handling (signal triggering) in combination with*

the laser beam diameter and the (scanned) object size on the quality of the point cloud?

Terrestrial laser scanners provide point clouds with specific properties. These might have an influence on the quality of the point clouds. The goal of this research question is to understand how laser scanners handle laser pulses intersecting with multiple objects. Furthermore, this knowledge should be mathematically described and implemented in a simulation environment, explain the influence of signal triggering approach and laser beam diameter on the quality, how objects (branches/trees) of different sizes are represented in the point clouds. The answers to this research question provide a rationale for decisions regarding the appropriate choice of TLS devices and survey objectives (e.g., minimal object size) for forest inventories.

3) What can we learn from the implementation of a simulation environment for TLS applications for forest inventories in terms of the influence of scanner placement and understorey density on the quality of tree volume estimation from point clouds?

The main goal of this research question is to describe a simulation environment in which a realistic TLS scanning campaign for tree volume estimation can be evaluated. The objective of the simulation study is to quantify the influence of understorey and wood assortment on the quality of volume estimation using TLS in a forest inventory. We therefore describe an easily configurable simulation environment. The variation of understorey and the combination of scanner locations in the simulation provide a deeper understanding on the abilities and limitations estimating the tree volume, using an established quantitative structure model (QSM). Findings from the first and second research question are used for the design of this study. The findings of the third research question support decisions on the feasibility to estimate tree volume (or part of the tree volume) in a forest inventory.

1.5.2 Structure of the thesis

Chapter 1 provides the general context of the thesis, explains the relevance of the approach and introduces the objectives and research questions of this thesis.

Chapter 2 addresses the first research question based on a peer-reviewed article in Forests (Abegg *et al.*, 2017). It evaluates the connection between stand parameters and scanner placement and provides a basis for the design of the experiments in chapter 4.

Chapter 3 addresses the second research question with an article under review in IEEE Transactions on Geoscience and Remote Sensing. It explains the signal triggering approaches of three state-of-the-art terrestrial laser scanners and analyses the influence of signal triggering, laser beam diameter on the quality of point clouds.

Chapter 4 addresses the third research question with an article currently under review in Agricultural and Forest Meteorology. It demonstrates a simulation environment for forest inventories and evaluates issues related to volume estimation with TLS. It supports findings of chapter 3.

Chapter 5 discusses the main findings of the thesis and general contributions to the research field, and presents an outlook to possible future research.

1.6 References

(2004a) *Laser-Scanners for Forest and Landscape Assessment*, vol. XXXVI - 8/W2 of *International Archives of the Photogrammetry, Remote Sensing and Spatial Information Sciences*. Freiburg, Germany.

(2004b) *XX ISPRS Congress, Commission V*, vol. XXXV-B5 of *International Archives of the Photogrammetry, Remote Sensing and Spatial Information Sciences*. Istanbul, Turkey.

(2010) *Silvilaser 2010*. Freiburg, Germany.

(2012) *Silvilaser 2012*. Vancouver, Canada.

Abegg M, Kükenbrink D, Zell J, Schaepman ME, Morsdorf F (2017) Terrestrial laser scanning for forest inventories - tree diameter distribution and scanner location impact on occlusion. *Forests*, **8**, 1 – 29.

Aschoff T, Spiecker H (2004) Algorithms for the automatic detection of trees in laser scanner data. In: ISP (2004a), pp. 66–70.

Aschoff T, Thies M, Spiecker H (2004) Describing forest stands using terrestrial laser scanning. In: ISP (2004b), pp. 237–241.

Astrup R, Ducey M, Granhus A, Ritter T, von Lpke N (2014) Approaches for estimating stand-level volume using terrestrial laser scanning in a single-scan mode. *Canadian Journal of Forest Research*.

Bienert A, Hess C, Maas HG, von Oheimb G (2014) A voxel-based technique to estimate the volume of trees from terrestrial laser scanner data. In: *The International Archives of the Photogrammetry, Remote Sensing and Spatial Information Sciences*, vol. XL-5. Riva del Garda, Italy.

Bienert A, Scheller S, Keane E, Mullooly G, Mohan F (2006) Application of terrestrial laser scanners for the determination of forest inventory parameters. In: *Commission V Symposium 'Image Engineering and Vision Metrology'*, vol. XXXVI part 5 of *International Archives of the Photogrammetry, Remote Sensing and Spatial Information Sciences*, p. 5. Dresden, Germany.

Binney J, Sukhatme GS (2009) 3d tree reconstruction from laser range data. In: *Robotics and Automation, ICRA'09 IEEE international Conference*. Kobe, Japan.

Brändli UB, Hägeli M (2019) *Swiss National Forest Inventory Methods and Models of the Fourth Assessment*, chap. LFI at a glance, pp. 3 – 29. In: Fischer & Traub (2019).

Brassel P, Lischke H (2001) *Swiss National Forest Inventory: Methods and Models of the Second Assessment*. WSL Swiss Federal Research Institute, Birmensdorf, Switzerland.

Bremer M, Rutzinger M, Wichmann V (2013) Derivation of tree skeleton and error assessment using lidar point cloud data of varying quality. *ISPRS Journal of Photogrammetry and Remote Sensing*, **80**, 39 – 50.

Bucksch A, Lindenbergh R (2008) Campino - a skeletonization method for point cloud processing. *ISPRS Journal of Photogrammetry and Remote Sensing*, **63**, 115 – 127.

Bucksch A, Lindenbergh R, Menenti M (2010) Robust skeleton extraction from imperfect point clouds. *The Visual Computer*, **26**, 1283–1300.

Burt A, Disney M, Calders K (2018) Extracting individual trees from lidar point clouds using treeseg. *Methods in Ecology and Evolution*, **10**, 438 – 445.

Cabo C, Ordóñez C, López-Sánches CA, Armesto J (2018) Automatic dendrometry: Tree detection, tree height and diameter estimation using terrestrial laser scanning. *International Journal of Applied Earth Observation and Geoinformation*, **69**, 164 – 174.

Calders K, Newnham G, Burt A, *et al.* (2015) Nondestructive estimates of above-ground biomass using terrestrial laser scanning. *Methods in Ecology and Evolution*, **6**, 198 – 208.

Côté JF, Fournier RA, Egli R (2011) An architectural model of trees to estimate forest structural attributes using terrestrial lidar. *Environmental Modelling & Software*, **26**, 761–777.

Disney M, Lewis P, Raumonen P (2012) Testing a new vegetation structure retrieval algorithm from terrestrial lidar scanner data using 3d models. In: Sil (2012).

Fischer C, Traub B (2019) *Swiss National Forest Inventory Methods and Models of the Fourth Assessment*. Springer Nature Switzerland.

FOREST EUROPE (2015) *State of Europe's Forests 2015*. FOREST EUROPE.

Gastellu-Etchegorry JP, Yin T, Lauret N, *et al.* (2015) Discrete anisotropic radiative transfer (dart 5) for modeling airborne and satellite spectroradiometer and lidar acquisitions of natural and urban landscapes. *Remote Sensing*, **7**, 1667–1701.

Gatziolis D, Popescub S, Sheridanb R, Kub NW (2010) Evaluation of terrestrial lidar technology for the development of local tree volume equations. In: Sil (2010), pp. 197–205.

Gorte B, Pfeifer N (2004) Structuring laser-scanned trees using 3d mathematical morphology. In: ISP (2004b), pp. 929–933.

Gorte B, Winterhalder D (2004) Reconstruction of laser-scanned trees using filter operations in the 3d raster domain. In: ISP (2004a), pp. 39–44.

Hackenberg J, Morhart C, Sheppard J, Spiecker H, Disney M (2014) Highly accurate tree models derived from terrestrial laser scan data: A method description. *Forests*, **5**, 1069 – 1105.

Hauglin M, Astrup R, Gobakken T, Naesset E (2013) Estimating single-tree branch biomass of norway spruce with terrestrial laser scanning using voxelbased and crown dimension features. *Scandinavian Journal of Forest Research*.

Heinzel J, Huber MO (2017a) Detecting tree stems from volumetric tls data in forest environments with rich understory. *Remote Sensing*, **9**.

Heinzel J, Huber MO (2017b) Tree stem diameter estimation from volumetric tls image data. *remote sensing*, **9**.

Heinzel J, Huber MO (2018) Constrained sspectra clustering of individual trees in dense forest using terrestrial laser scanning data. *remote sensing*, **10**.

Herold A, Zell J, Rohner B, Didion M, Thürig E, Rösler E (2019) *Swiss National Forest Inventory Methods and Models of the Fourth Assessment*, chap. State and change of forest resources, pp. 202 – 235. In: Fischer & Traub (2019).

Holopainen M, Vastaranta M, Kankare V, *et al.* (2011) Biomass estimation of individual trees using stem and crown diameter tls measurements. In: *ISPRS Workshop Laser Scanning 2011*, vol. XXXVIII-5/W12 of *International Archives of the Photogrammetry, Remote Sensing and Spatial Information Sciences*, pp. 91–95. Calgary, Canada.

Hopkinson C, Chasmer L, Young-Pow C, Treitz P (2004) Assessing forest metrics with a ground-based scanning lidar. *Canadian Journal of Forest Research*, **34**, 573–583.

Horvitz D, Thompson D (1952) A generalization of sampling without replacement from a finite universe. *Journal of the American Statistical Association*, **47**, 663 – 685.

Hough PVC (1962) Method and means for recognizing complex patterns.

Keightley KE, Bawden GW (2010) 3d volumetric modeling of grapevine biomass using tripos lidar. *Computers and Electronics in Agriculture*, **74**, 305 – 312.

Kelbe D, Romanczyk P, vanAardt J, Cawse-Nicholson K, Krause K (2012) Automatic extraction of tree stem models from single rerrestrial lidar scans in structurally heterogeneous forest environments. In: Sil (2012), pp. 1–8.

Kiraly G, Brolly G (2010) Volume calculations of single trees based on terrestrial laser scanning. In: Sil (2010), pp. 15–22.

Kukko A, Hyyppä J (2007) Laser scanner simulator for system analysis and algorithm development: A case with forest measurements. In: *Laser Scanning 2007 and SilviLaser 2007*.

Lanz A, Fischer C, Abegg M (2019) *Swiss National Forest Inventory Methods and Models of the Fourth Assessment*, chap. Sampling Design and Estimation Procedures, pp. 29 – 90. In: Fischer & Traub (2019).

Lewis P (1999) Three-dimensional plant modelling for remote sensing simulation studies using the botanical plant modelling system. *Agronomie*, **19**, 185 – 210.

Liang X, Hyyppä J (2013) Automatic stem mapping by merging several terrestrial laser scans at the feature and decision levels. *Sensors*, **13**, 1614 – 1634.

Liang X, Kankare V, Yu X, Hyyppä J, Holopainen M (2014) Automated stem curve measurement using terrestrial laser scanning. *IEEE Transactions on Geoscience and Remote Sensing*, **52**, 1739 – 1748.

Liang X, Litkey P, Hyyppä J, Kaartinen H, Vastaranta M, Holopainen M (2012) Automatic stem mapping using single-scan terrestrial laser scanning. *IEEE Transactions on Geoscience and Remote Sensing*, **50**, 661 – 670.

Lovell J, Jupp D, Newnham G, Coops N, Culvenor D (2005) Simulation study for finding optimal lidar acquisition parameters for forest height retrieval. *Forest Ecology and Management*, **214**, 398 – 412.

Lovell J, Jupp D, Newnham G, Culvenor D (2011) Measuring tree stem diameters using intensity profiles from ground-based scanning lidar from a fixed viewpoint. *ISPRS Journal of Photogrammetry and Remote Sensing*, **66**, 46–55.

Maas HG, Bienert A, Scheller S, Keane E (2008) Automatic forest inventory parameter determination from terrestrial laser scanner data. *International Journal of Remote Sensing*, **29**, 1579–1593.

MacDicken K, Jonsson O, Piña L, *et al.* (2016) *Global Forest Resources Assessment 2015: How are the world's forests changing?* Food and Agriculture Organistation of the United Nations (FAO), Roma, Italy.

Mandallaz D (2006) *Sampling Techniques for Forest Inventories*. Chapman & Hall/CRC Applied Environmental Statistics. Chapman and Hall/CRC, Boca Raton, USA.

Morsdorf F, Kükenbrink D, Schneider D, Abegg M, Schaepman ME (2018) Close-range laser scanning in forests: towards physically based semantics across scales. *Interface focus*, **8**.

Othmani A, Piboule A, Krebs M, Stolz C, Lew Yan Voon L (2011) Towards automated and operational forest inventories with t-lidar. In: *Silvilaser 2011*. Hobart, Australia.

Pan Y, Birdsey RA, Fang J, *et al.* (2011) A large and persistent carbon sink in the world's forests. *Science*, **333**, 988 – 993.

Raumonen P, Kaasalainen M, Akerblom M, *et al.* (2013) Fast automatic precision tree models from terrestrial laser scanner data. *Remote Sensing*, **5**, 491–520.

Saarinen N, Kankare V, Vastaranta M, *et al.* (2017) Feasibility of terrestrial laser scanning for collecting stem volume information from single trees. *ISPRS Journal of Photogrammetry and Remote Sensing*, **123**, 140 – 158.

Särndal CE, Swensson B, Wretman J (2003) *Model assisted survey sampling*. Springer Science & Business Media.

Schilling A, Schmidt A, Maas HG (2011) Automatic tree detecion and diameter estimation in terrestrial laser scanner point clouds. In: *16th Computer Vision Winter Workshop* (eds. Wendel A, Sternig S, Godec M). Mitterberg, Austria.

Seidel D, Albert K, Ammer C, Fehrmann L, Kleinn C (2013) Using terrestrial laser scanning to support biomass estimation in densely stocked young tree plantations. *International Journal of Remote Sensing*, **34**, 8699 – 8709.

Seidel D, Albert K, Fehrmann L, Ammer C (2012) The potential of terrestrial laser scanning for the estimation of understory biomass in coppice-with-standard systems. *Biomass and Bioenergy*, **47**, 20 – 25.

Seidel D, Beyer F, Hertel D, Fleck S, Leuschner C (2011) 3d-laser scanning: A non-destructive method for studying above- ground biomass and growth of juvenile trees. *Agricultural and Forest Meteorology*, **151**, 1305 – 1311.

Shvidenko A, Barber CV, Persson R (2005) *Forest and Woodland Systems*, chap. 21, pp. 585 – 621. Island Press.

Simonse M, Aschoff T, Spiecker H, Thies M (2003) Automatic determination of forest inventory parameters using terrestrial laser scanning. In: *Proceedings of the ScandLaser Scientific Workshop on Airborne Laser Scanning of Forests*, pp. 251–257. Umeå, Sweden.

Tansey K, Selmes N, Anstee A, Tate NJ, Denniss A (2009) Estimating tree and stand variables in a corsican pine woodland from terrestrial laser scanner data. *International Journal of Remote Sensing*, **30**, 5195–5209.

Thies M, Pfeifer N, Winterhalder D, Gorte B (2006) Three-dimensional reconstruction of stems for assessment of taper, sweep and lean based on laser scanning of standing trees. *Scandinavian Journal of Forest Research*, **19**, 571–581.

Tomppo E, Gschwantner T, Lawrence M, McRoberts RE (2010) *National Forest Inventories*. Springer.

Van der Zande D, Jonckheere I, Stuckens J, Verstraeten WW, Coppin P (2008) Sampling design of ground-based lidar measurements of forest canopy structure and its effect on shadowing. *Canadian Journal of Remote Sensing*, **34**, 526 – 538.

Wezyk P, Koziol K, Glista M, Pierzchalski M (2007) Terrestrial laser scanning versus traditional forest inventory. first result from the polish forests. In: *ISPRS Workshop on Laser Scanning 2007 and SilviLaser 2007*, pp. 424 – 429.

Wilkes P, Sarmiento AL, Disney M, *et al.* (2017) Data acquisition considerations for terrestrial laser scanning of forest plots. *Remote Sensing of Environment*.

Yang X, Strahler AH, Schaaf CB, *et al.* (2013) Three-dimensional forest reconstruction and structural parameter retrievals using a terrestrial full-waveform lidar instrument (echidna). *Remote Sensing of Environment*, **135**, 36 – 51.

Yao T, Yang X, Zhao F, *et al.* (2011) Measuring forest structure and biomass in new england forest stands using echidna ground-based lidar. *Remote Sensing of Environment*, **115**, 2965–2974.

Chapter

2

Terrestrial Laser Scanning for Forest Inventories – Tree Diameter Distribution and Scanner Location Impact on Occlusion

This chapter is based on the peer-reviewed article:
***Abegg, M.**, Kükenbrink, D., Zell, J., Schaepman, M. E., Morsdorf, F. (2017) Terrestrial Laser Scanning for Forest Inventories – Tree Diameter Distribution and Scanner Location Impact on Occlusion. Forests, (8), 1-29.*
DOI:10.3390/f8060184
It is reprinted as the final submitted manuscript and has been modified to fit the layout of this thesis.

M.A. designed the experiments, performed the analysis and interpreted the results. D.K. contributed the voxel traversal code. J.Z. derived Weibull parameters from NFI data and assisted with the interpretation of the statistics. M.E.S. contributed to the experimental design and content of the publication, F.M. contributed to the experimental design and analysis. All authors wrote and reviewed the manuscript with main contribution of M.A.

Abstract

The rapid development of portable terrestrial laser scanning (TLS) devices in recent years has led to increased attention to their applicability for forest inventories, especially where direct measurements are very expensive or nearly impossible. However, in terms of precision and reproducibility, there are still some pending questions. In this study, we investigate the influence of stand parameters on the TLS-related visibility in forest plots. We derived 2740 stand parameters from Swiss national forest inventory sample plots. Based on these parameters, we defined virtual scenes of the forest plots with the software "Blender". Using Blender's ray-tracing features, we assessed the 3D coverage in a cubic space and 2D visibility properties for each of the virtual plots with different scanner placement schemes. We provide a formula to calculate the maximum number of possible hits for any object size at any distance from a scanner with any resolution. Additionally, we show that the Weibull shape parameter describing a stand, in addition to the number of trees and the mean diameter of the dominant 100 trees per hectare, has a significant and relevant influence on the visibility of the sample plot. Furthermore, we show the effectiveness and the efficiency of 40 scanner location patterns. These experiments demonstrate that intuitively distributing scanner locations evenly within the sample plot, with similar distances between locations and from the edge of the sample plot, provides the best overall visibility of the stand.

2.1 Introduction

National Forest Inventories (NFI) deliver information on the forest area, the amount and change of forest resources, the development of the biotope forest in general, the carbon balance of a country (FOREST EUROPE, 2015; MacDicken *et al.*, 2016; Pan *et al.*, 2011) and other ecosystem services (Shvidenko *et al.*, 2005). In the Swiss NFI, data collection is based on aerial photo interpretation, forest service interviews and field measurements (Brassel & Lischke, 2001). Field measurements provide the largest and most important collection of data for a NFI. On a national level, they comprise measurements of several thousand sample plots, each of which has to be visited by a field team (Tomppo *et al.*, 2010). Field measurements consist of two methods: actual measurements and expert assessments. If possible, measurements are applied to determine forest features. However, certain forest features are nearly impossible to measure on standing trees or can only be measured at a very high cost with traditional tools. Examples of such features are tree volume, forest structure, crown size and shape, gap size and light availability at certain heights above ground. The medium-term objective of the Swiss NFI is to replace or enhance expert assessments with actual measurements where possible. The development of portable terrestrial LiDAR devices in recent years and increased computing power lead to the question of whether these devices can be used for forest inventories to enhance the efficiency and improve data quality.

Given the high costs of terrestrial laser scanning systems (TLS) and the time-consuming measurement process, the added value of TLS for forest inventories needs to be clearly demonstrated in terms of efficiency, robustness and precision. One evaluation method is to simulate a virtual forest and a virtual instrument, as described by several authors (Lovell *et al.*, 2005; Disney *et al.*, 2012; Van der Zande *et al.*, 2008; Binney & Sukhatme, 2009). The advantage of the simulation approach is that many configurations can be tested with only little expense for additional samples. Still, the simulation environment is merely an abstraction of reality and, consequently, the representativeness of the virtual scene has to be considered carefully. Several factors, such as scanning resolution, the LiDAR technology applied, and weather conditions, influence the quality of the laser scans in terms of completeness and accuracy. However, as mentioned by various authors (e.g., (Watt & Donoghue, 2005; Trochta *et al.*, 2013; Van der Zande *et al.*, 2006)), occlusion is one of the key factors that limits the potential of TLS. Occlusion is caused by objects shadowing each other, so that parts of the objects of interest are not visible to the TLS device. The effect of occlusion is usually mitigated by combining TLS scans from different locations (Hilker *et al.*, 2012). In the literature, various scanner location combination patterns are described (e.g., (Watt & Donoghue, 2005; Wezyk *et al.*, 2007; Yang *et al.*, 2013; Liang *et al.*, 2016)). Trochta et al. (Trochta *et al.*, 2013) compare the quality of multiple scans in natural beech forests. Van der Zande et al. (Van der Zande *et al.*, 2008) evaluate three different scanner position combinations, each in three different types of stands. However, for the possible applications of TLS in forest inventory, the methods need to have a proven high performance in a larger range of forest stand conditions. The decision maker of a forest inventory needs a fundamental understanding of the influencing factors regarding the quality of the point clouds generated by TLS and possible constraints on operational applications. The analysis of visibility can contribute to quantifying the expected quality of TLS acquisitions in terms of completeness.

The goal of this study is to highlight both the potential and the limitations of TLS in terms of expected TLS points per object and to explain the influence of the stand and the scanner placement on the quality of the scans in terms of completeness. We therefore use simulations in order to explore the widest possible range of stand and scanner placement characteristics. Our objectives are:

(i) To demonstrate the relationships between angular resolution of the scanner, object size, distance to the scanner and the possible sampling frequency (scanner point density) on an object with TLS in a 3D space. This should help determine the minimal object size detectable by TLS.

(ii) To show the connection between the visibility of a sample plot and its stand describing parameters, such as diameter distribution, stem number and dominant diameter. This experiment improves the understanding of how the stand properties influence the scan quality. We hypothesize that there is a very strong link between the stand parameters and the visibility.

(iii) To demonstrate the influence of the scanning location within a sample plot on the visibility.

(iv) To understand the mechanism behind occlusion and to determine the most suitable scanner location patterns for TLS acquisitions in forests.

2.2 Materials and Methods

2.2.1 The NFI Framework, Data and Tools

2.2.1a Sample Plot

Depending on the target variable, different plot sizes are used in the Swiss NFI. The radii of the six sample plots for the tree measurement of the different diameter classes range from 0.9 m to 12.62 m (0.9 m, 1.5 m, 2.5 m, 4 m, 7.98 m, 12.62 m). The largest sample plot, a square area of 50 $\times$ 50 m termed the "interpretation area", is used to assess stand level parameters, such as stand structure and occurrence of important elements in the stand, such as snags or coverage of regeneration (Keller, 2011). For the evaluations of TLS applications, we chose to evaluate this largest area because all the sample plots of the Swiss NFI are contained within this area. For the evaluation, we defined the sample plot into a 2-dimensional cartesian coordinate system. The centre of the sample plot is located at the x–y-coordinates (0, 0).

2.2.1b NFI Data

NFI data are commonly collected on sample plots arranged in a regular grid over an area of interest. This allows for a statistical inference of population values, such as stem number, for the investigated area (Mandallaz, 2006). Since the year 2009, the Swiss NFI has conducted its field measurements on nine equally sized grids, which are placed so that all the grids combined constitute one regular grid with a mesh size of approximately 1.41 km ($\sqrt{2}$). This always allows a representative evaluation of either single or combined grids.

At each grid intersection point, the trees are recorded on different circular plots depending on their size as mentioned earlier (Size classes: 0.1 m–0.39 m height,

0.4–1.29 m height, 0.1–3.9 cm DBH, 4–11.9 cm DBH, 12–35.9 cm DBH, ≥36 cm DBH). Nevertheless, the methods applied are the same, allowing all the measured trees of any given diameter at breast height (DBH) to be combined. Since every tree of any diameter contributes to occlusion, we included all trees reaching 1.3 m in height for our evaluation. We used the combined datasets of all the trees per grid intersection point, respecting their statistical selection probability, to derive stand describing parameters.

The Weibull distribution is a common choice for describing the density of diameters in a stand (Bailey & Dell, 1973). It is a left-truncated distribution and can handle a wide spectrum of stand situations. The Weibull distribution consists of three parameters, a shape (W_{shape}), a scale (W_{scale}) and an offset that describes the smallest diameter. The offset was set to 0.5 cm as a fixed parameter because this is the smallest diameter measured at breast height. W_{shape} and W_{scale} were estimated by maximising the likelihood function of the Weibull distribution, given the observations. Since this estimation is subject to a stochastic process, we excluded extreme outliers which we could identify with commonly used NFI parameters. We excluded the simulated samples that exceeded double the maximal determined D_{dom} in a Swiss NFI field campaign (185 cm) and all the samples that have one simulated diameter that exceeds three times the maximal measured diameter in the Swiss NFI of 207 cm. With this variability, we covered all the possible stand parameters that are likely to occur in the Swiss forests and included some extreme values as well.

2.2.1c Blender

Blender (Blender Online Community, 2015) is an open-source 3D content creation suite. For this publication, we used version 2.74. Blender can be fully controlled using the programming language python. It allows the user to create 3D objects and define their light interaction properties. These features are normally used to render photorealistic images or animated movies. Blender provides a large toolbox to define, manipulate and store 3D objects.

We used Blender and the stand parameters to set up cylinders as a proxy for trees for a visibility assessment (see Figure 2.1). The Weibull parameters W_{shape} and W_{scale} defined the shape of the diameter distribution. N_{tree} on the other hand, defined the number of cylinders to be set up. A random number generator for Weibull distributions in the python library “numpy” provided the diameters of the cylinders. The locations of the cylinders were calculated by a random uniform number generator, which leads to Poisson-distributed cylinders on the sample plot. No cylinder was allowed to overlap the scanner positions or another cylinder, and any overlapping cylinders were relocated to a new random position within the sample plot. The cylinders were initially defined as a Bézier curve with a certain diameter (bevel) and then converted to a mesh. A mesh is defined in Blender as a number of points (vertices) that are connected with lines (edges) and polygons (faces). The time needed for the definition of new cylinders increases exponentially, so we sourced out the definition of new cylinders when N_{tree} exceeded 4000. For this step, we used a Blender feature called particle systems. With particle systems, a single object can be multiplied and randomly placed, without using much computing power, by defining the number and the random locations with a mathematical equation. We used particle systems to randomly place the smallest trees (cylinders), which are the single reason for higher N_{tree} values. To avoid overlapping with the scanner location, we spared an area of 0.04 m^2 around the scanner positions. To account for particle system cylinders located within larger cylinders, which were not defined by a particle

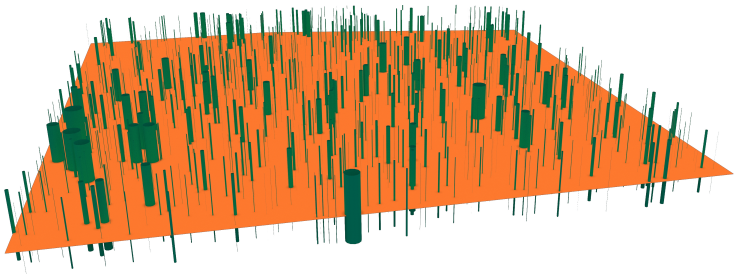

Figure 2.1: Rendering of the cylinder placement of one sample plot in Blender. The 50 × 50 m sample plot is orange and the cylinders following the Weibull distribution of tree diameters are green.

system, we increased the number of particle cylinders using the ratio of the basal area of the larger cylinders to the sample plot size.

2.2.1d Simulated Laser Scanning

BlenSor is an add-on for Blender which allows the user to simulate various types of range scanners and other optical instruments (Gschwandtner *et al.*, 2011). It enables an efficient intersection of mathematical vectors (rays) with 3D objects defined in Blender and returns the range and the incidence angle. This information allows the user to calculate the number of rays possibly hitting an object at any distance from the origin of the ray (scanner location), or it can be used as a sampling procedure for visibility assessments of the sample plots.

2.2.1e Voxel Traversal Algorithm

We used a voxel traversal algorithm implemented by (Kükenbrink *et al.*, 2016) based on the approach described by (Amanatides & Woo, 1987). By knowing the starting point (scanner location) and the point where the laser beam (mathematical vector) hits an object, this algorithm can calculate, for every voxel in a predefined voxel grid, whether the vector entered a voxel or was stopped before entering the voxel. In this way, the algorithm returns, for a given set of rays, the number of rays entering each voxel and those intercepted (occluded) before reaching that particular voxel.

2.2.1f Visibility Assessment

Visibility assessment has a long tradition in GIS sciences for the evaluation of digital elevation models (e.g., (Fisher, 1991; Travis *et al.*, 1975)). Our approach is to use TLS simulations to assess the 2-dimensional visibility of forest stands. We use BlenSor to send out horizontal vectors from a virtual scanner position, following specific angular steps (angular resolution). From a statistical point of view, we sample the visibility of a given space (e.g., the sample plot) with the vectors and assess the visibility along each of the vectors by intersecting them with the objects (cylinders) within that space (see Figure 2.2). BlenSor returns the coordinates of the intersections within the sample plot or, in cases where there is no intersection, a coordinate of the vector outside the sample plot (red dots in Figure 2.2). The obtained dataset is a 2D point cloud (or 3D point cloud with all the points in one plane). The voxel traversal algorithm described above evaluates for each voxel of a predefined voxel grid, the number of vectors entering and the number of vectors that could theoretically enter the voxel without occlusion. The visibility experiments, as described below, are

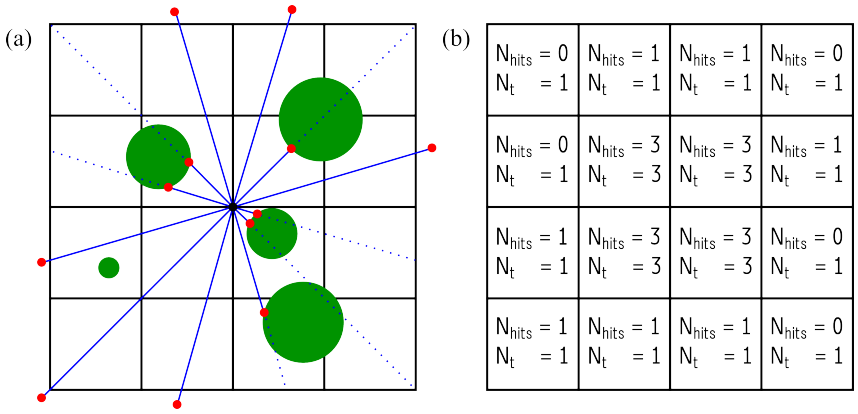

Figure 2.2: Illustration of visibility assessment. (**a**) Sample plot divided into a voxel (pixel) grid with scanner position in the centre. The cylinders are displayed as green circles, the unoccluded vectors as blue lines, the vectors occluded by the trees as dotted blue lines and the points of the point cloud as red dots; (**b**) The same sample plot showing, for each voxel (pixel), the number of vectors entering the voxel cell (N_{hits}) and the number of vectors that could enter the voxel cell without occlusion (N_t).

conducted with vectors in a plane and the voxel space height is only one voxel, so one could also speak of "pixels" instead of "voxels". For the visibility assessment in this publication, we calculated, for each voxel, the ratio of rays entering the voxel to all the rays that theoretically could have entered the voxel. This is a measure of the visibility of a given voxel. We defined the mean of all these ratios within a plot as the mean relative visibility (V_m). We chose V_m as a measure of visibility because it takes every voxel into account, irrespective of the distance from the scanner.

2.2.2 Theoretical Coverage of a Laser Scanning System in a 3D Space

The goal of this experiment was to determine the theoretical minimal coverage of a laser scanning system in a cubic space. The vertical extent of the sample plot was set to 50 m because that is the height of the tallest measured trees in the Swiss NFI.

We assumed the laser beam to be infinitesimally small in diameter. To define the direction in which these rays start, we assumed a scanning system with a rotating mirror on a horizontal axis. This mirror rotates again around a vertical axis, as applied in many commercial scanning systems, such as Faro Focus 3D and Leica BLK360, and in experimental systems such as SALCA (Gaulton *et al.*, 2013). In such a scanning system, the angular resolution refers to the angular steps in longitudinal and latitudinal directions. It leads to an increasing point density from the horizontal plane towards the zenith and the nadir. We tested angular scanning resolutions ranging from 0.01° to 1.00° (i.e., the angular resolutions in [°] of 0.01, 0.02, 0.04, 0.06, 0.1, 0.2, 0.5, 1). The location for the scanning system we chose to be the centre of the sample plot, at 1.3 m height above ground, corresponding to the height of the DBH measurement. To mimic variations in the object size, we varied the voxel size from 1 mm up to 1 m (i.e., the sizes in [m] of 0.001, 0.005, 0.01, 0.05, 0.06, 0.07, 0.1, 0.5, 1). To reduce the calculation time, we did not evaluate all the voxels in the voxel space but instead a maximum of 5000 randomly selected voxels for each scanner configuration.

As a measure of the coverage, we used the voxel traversal algorithm described in Section 2.2.1e to count the number of rays entering the sampled voxels (N_{hits}). As explanatory variables, we calculated, for each voxel, the Euclidean distance

(D_e) from the voxel centre to the scanner location. To account for the effect of a higher point density towards the zenith and the nadir of the scanner, we derived the horizontal distance (D_h) to the scanner location. D_h is the distance, projected on the X–Y-plane, from the voxel centre to the scanner location. Additionally, we calculated the ratio of voxel size to scanner resolution ($R_{vs/sr}$). To test for the influence of D_e, D_h and $R_{vs/sr}$ on N_{hits}, we applied a linear regression using the software R (R Core Team, 2017). Since all the variables are positive numbers, we log-transformed them following the recommendations of (Mosteller & Tukey, 1977). As some configurations with $R_{vs/sr}$ exhibited many voxels with N_{hits} of 0, we applied the regression on configurations starting at an $R_{vs/sr}$ of 1. At that point, every voxel in the 50 m cubic space obtains at least one hit, which allows the regression to be fitted in a meaningful way.

2.2.3 Influence of Stand Parameters on Visibility in a 2D Space

We used Blender to set up 2740 sample plots based on five annual NFI grids. For sampling visibility, we chose an angular resolution of 0.001°, which manifests a high sampling frequency. The voxel size was chosen considering two effects: if the voxel size is too small, the demand in computing power increases. However, large voxels overestimate the actual visibility. For the following experiments, we chose a voxel size of 0.1 m.

We calculated additional NFI-related stand parameters based on the generated diameter distribution files, to be used in the evaluation of the results. One parameter is the mean diameter of the 100 largest trees per hectare (D_{dom}). The other parameter is the stem number of the trees with a minimal diameter at breast height of 12 cm ($N_{tree \geq 12cm}$). To test the influence of the stand parameters, we transformed the dependent and independent variables, following the recommendations of (Mosteller & Tukey, 1977). Since the range of V_m is from 0 to 1, we applied an arc-sin-square-root transformation. The other variables were log-transformed. The software R (R Core Team, 2017) was used for the analysis.

2.2.4 Influence of the Scanning Location within Sample Plots on Visibility in a 2D Space

In this experiment, we investigated the influence of the scanning location within the sample plot on the visibility. We tested 25 evenly distributed scanning positions along the positive x-axis (T_h) of the local coordinate system. Another 25 scanner positions were tested following the diagonal (T_d) from the centre to the corner with coordinates (25, 25). Combined with the central scan, 51 scanner positions were tested in total (see Figure 2.3). In contrast to the other experiments where cylinders were set up with Blender, cylinders overlapping the scanner position were not relocated in this experiment. The affected sample plots were dropped from the sample to avoid alleys of visibility which would be generated on transects if the other approach was chosen. Due to computational constraints, we used the 537 stand samples from the last reporting period (2013) and not the full data set. Other than that, this experiment was set up identically to the former, using the same software tools. To test the influence of the scanner position, two additional independent variables were appended to the model described in the former experiment (see Equation (2.3)). We wanted to test the supplementary influence of the distance to the centre (D_c) and the transect (F_t) the scanner location belongs to. Both variables were added

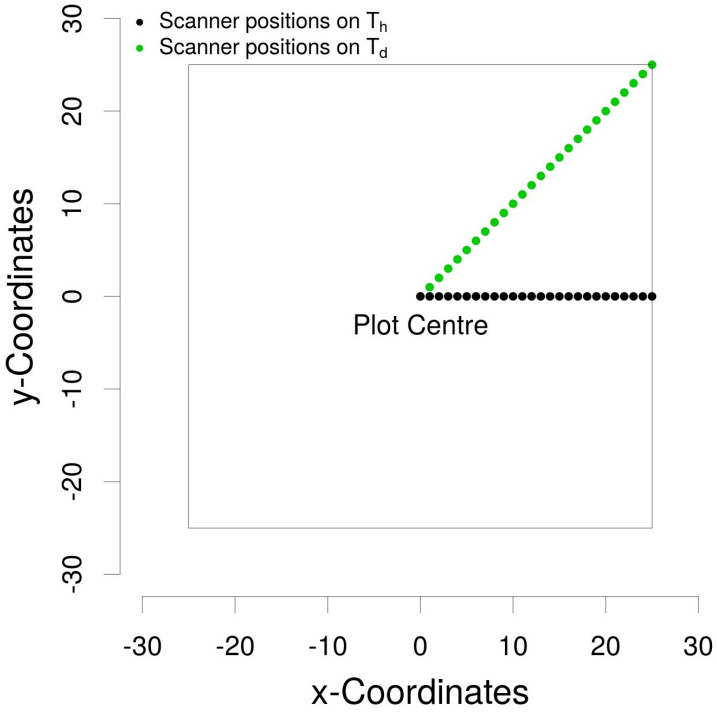

Figure 2.3: Locations of the tested scanner positions within the sample plot. T_h is the transect following the x-axis, T_d is the transect directed at a corner of the sample plot.

to the model, and D_c was log-transformed and squared. To visualize the influence of only these two variables, we removed the predicted values of the model using only the stand parameters from the actual V_m. The difference in V_m between the two transects we calculated as follows: first, we retransformed the residuals of the model with the stand parameters and D_c; second, we calculated the mean of these residuals for each transect. The difference of these means of residuals represents the mean difference in V_m without the influence of the stand parameters and D_c.

2.2.5 Influence of Scanner Location Patterns on Visibility in a 2D Space

The goal of this experiment was to show the influence of scanner location patterns (P_{sl}) on the visibility. A scanner location pattern is the combination of several scanning locations, as used for multiple terrestrial laser scanning acquisition. As in Section 2.2.4, we used the stand parameters of one annual NFI sampling grid. Various (P_{sl}) are described in the literature. Some authors (Antonarakis, 2011; Hilker *et al.*, 2012; Watt & Donoghue, 2005; Liang & Hyyppä, 2013; Liang *et al.*, 2014) describe multiple scanning patterns, where most of the scanner locations are on the edge of the sample plot. Others (Thies *et al.*, 2006; Bienert *et al.*, 2006; Maas *et al.*, 2008; Côté *et al.*, 2012) placed the scanner at multiple locations outside of the sample plot, either to scan isolated stands or to scan within a larger stand. On the other hand, a third group of authors (Simonse *et al.*, 2003; Eysn *et al.*, 2013; Yao *et al.*, 2011; Van der Zande *et al.*, 2008; Calders *et al.*, 2015; Woodgate *et al.*, 2016) applied various scanner location patterns, such as one scan in the centre and four to six around it, or distributed the scanner locations evenly. Based on these scanner location patterns, we defined 25 scanning locations that could be combined to form various scanner location patterns (see Figure 2.4). We also added very close scanning locations to test the effect of very dense scanner patterns (e.g., a brute force

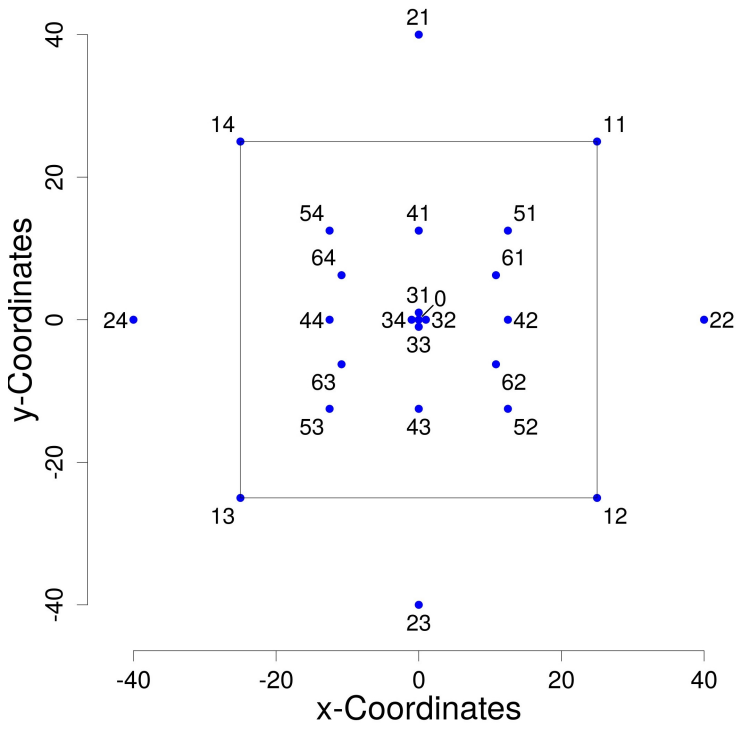

Figure 2.4: The scanning locations tested in each sample plot of 50 × 50 m. The displayed scanning locations, with their identification number, can be combined to form scanning location patterns for the search for efficient patterns, which are each evaluated for occlusion and coverage (visibility).

approach). Due to computational constraints, we restricted testing of the patterns we found in the literature and only added specific scanner location patterns to learn about the effect of shifting one scanning location. The complete set of tested scanner location patterns is shown in the Appendix 3.6 in Figures S2.2 and S2.3. Due to the combination of multiple scanner locations with their associated 2D point clouds, we calculated the visibility (V_m) in the following way: For each scanning location to be used in a pattern, we calculated the invisible fraction of each voxel (F_i). F_i is one minus the ratio of rays entering the voxel to the number of rays that could have entered the voxel in case of no occlusion. To combine the visibility of the various scanner locations, we assumed that every additional scan reduces the initial F_i in (actuarial) expectation in the ratio of F_i of the newly added scan. So the V_m of n combined scans is calculated as showed in Equation (2.1).

$$V_m = 1 - (F_{i(1)} * F_{i(2)} * ... * F_{i(n)}) \tag{2.1}$$

To check for the influence of the number of positions (N_s) used for a scanning pattern and the scanner location pattern (P_{sl}), we added these variables to the basic equation with the stand parameters (see Equation (2.3)). We log-transformed N_s following the recommendations of (Mosteller & Tukey, 1977). We compared the efficiency of the various P_{sl} without the influence of the stand parameters and N_s (see Figure 2.5). To do so, we fitted the basic model (Equation (2.3)) including N_s using the software R (R Core Team, 2017). With this model, we predicted V_m for all the sample plots. We subtracted this value from the "measured" V_m and normalised these values by subtracting the mean V_m of the single scanner locations in the centre of the sample plot. We call this value "scan location pattern efficiency" (P_{sl}-efficiency).

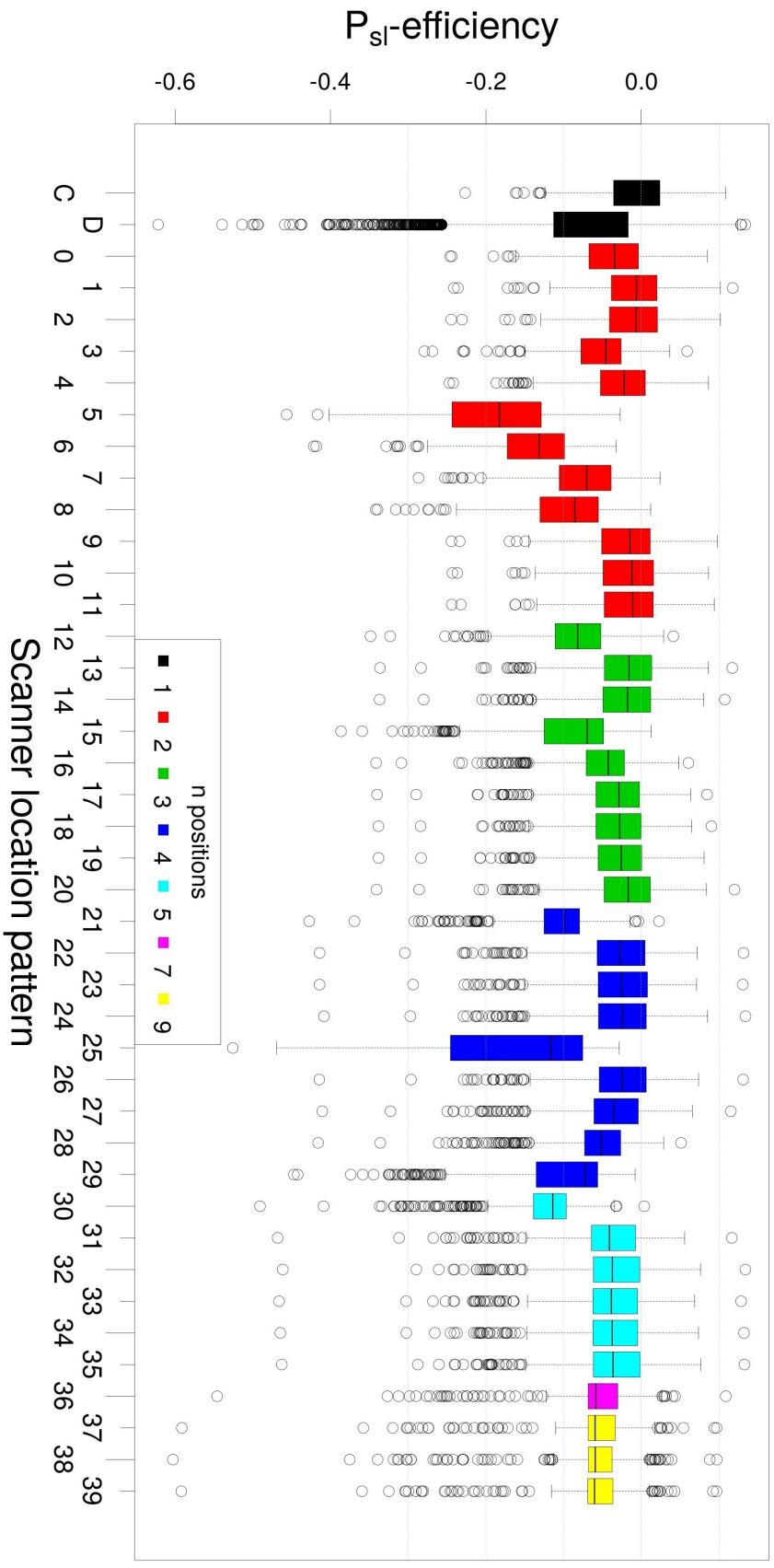

Figure 2.5: Efficiency of the scanner location patterns (P_{sl}-efficiency). P_{sl}-efficiencies are the residuals of the V_m model explained by the stand parameters and the number of combined scanner locations, normalised to the mean V_m of single scans in the centre of the sample plots. The figure shows the change in efficiency compared with that of the central scan (C) when different scanner location patterns are applied. The scanner location pattern "C" is the single central scan and "D" is the mean of all the other tested single scan positions that were used for the patterns.

2.3 Results

2.3.1 Theoretical Coverage of a Laser Scanning System in a 3D Space

To investigate the theoretical coverage of a TLS system in a cubic space with an edge length of 50 m, we simulated laser range measurements with geometric vectors as a proxy for TLS laser pulses. As a proxy for object size, we used the size of voxels in the given 3D space. The number of laser beams (vectors) entering each voxel N_{hits} served as a measure of coverage, i.e., detection quality of the laser scanner. With a sufficient resolution, any size of object could theoretically be resolved throughout the scene, i.e., at any distance to the scanner, given, that the laser beam has no extent (footprint). Besides the Euclidean distance D_e and the horizontal distance D_h from the voxel centre to the scanner location, we used the ratio of voxel size to scanner resolution ($R_{vs/sr}$) as an independent variable to explain N_{hits}. For a proper applicability of a linear regression, we only used settings where every voxel in the cubic space of 50 m has at least one vector passing it. Figure 2.6 shows that, in the given experimental setting, this point is reached when $R_{vs/sr}$ is equal to 1.

The regression was conducted using the following formula:

$$log(N_{hits}) = log(D_h) + log(D_e) + log(R_{vs/sr}) \tag{2.2}$$

The regression showed a very good performance, with all variables highly significant and an adjusted R^2 of 0.99. Table 2.1 displays the coefficients of the independent variables and their respective p values.

In Table S2.1 in the Appendix 3.6, the mean number of hits per voxel in the various ratio classes and the (Euclidean) distance to the scanner are shown.

2.3.2 Influence of Stand Parameters on Visibility in a 2D Space

The hypothesis was that the structure of a stand, represented by a Weibull distribution, stem number and dominant diameter (D_{dom}), would have an influence on the visibility within the stand. D_{dom} is the mean diameter of the 100 largest trees per hectare. To test this hypothesis, we randomly placed cylinders following Weibull distributions derived from 2740 sample plots of the Swiss NFI from the year 2009 to 2013. The number of placed cylinders ranges from 30 to 19,620 (see Figure 2.7). The scale parameter of the Weibull distribution ranges from 0.002 to 65.8 and the shape parameter ranges from 0.2 to 9.8. To analyse the visibility, the mean relative visibility of voxels (V_m) in each 50 $\times$ 50 m plot was calculated. The relative visibility of a voxel is the ratio between the vectors emitted from the virtual scanner location

Table 2.1: Model coefficients and standardised model coefficients based on scaled variables to make their effect sizes comparable.

Variable	Model Coefficient	Standardised Model Coefficient	*p* Value
Intercept	8.38	0	<0.0001
log (D_h)	−0.9	−0.22	<0.0001
log (D_e)	−1.09	−0.18	<0.0001
log ($R_{vs/sr}$)	2.03	0.92	<0.0001

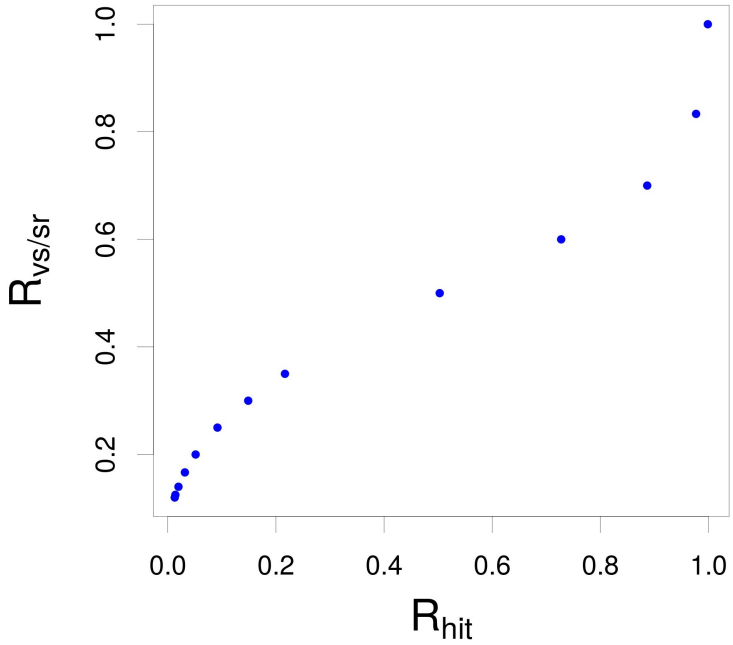

Figure 2.6: The relationship between the ratio of voxel size to scanner resolution [m/°] ($R_{vs/sr}$) and the ratio of the number of voxels hit by at least one ray to all the voxels in the cubic space with edge size of 50 m (R_{hit}).

Table 2.2: Model coefficients and standardised model coefficients based on scaled variables to make their effect size comparable.

Variable	Model Coefficient	Standardised Model Coefficient	*p* Value
Intercept	2.726	0	<0.0001
$log(N_{tree})$	−0.249	−1.211	<0.0001
$log(W_{shape})$	−0.124	−0.384	<0.0001
$log(D_{dom})$	−0.116	−0.271	<0.0001
$log(N_{tree \geq 12cm})$	0.008	0.06	<0.0001

(that either passed the voxel or hit an object within that voxel) and the theoretical number of vectors that could pass the voxel in a space without occluding objects. To account for the occurring range in the variables, they were transformed following the recommendations of (Mosteller & Tukey, 1977).

The regression was conducted using the following formula:

$$\arcsin(\sqrt{V_m}) = log(N_{tree}) + log(W_{shape}) + log(W_{scale}) + log(D_{dom}) + log(N_{tree \geq 12cm}) \quad (2.3)$$

All the independent variables except the Weibull scale parameter (W_{scale}) are highly significant, with an adjusted R^2 of 0.96. The refitted model without W_{scale} led to the coefficients shown in Table 3.3. In Figure S2.1 in the Appendix 3.6, the distribution of V_m for different D_{dom} and N_{tree} classes is shown.

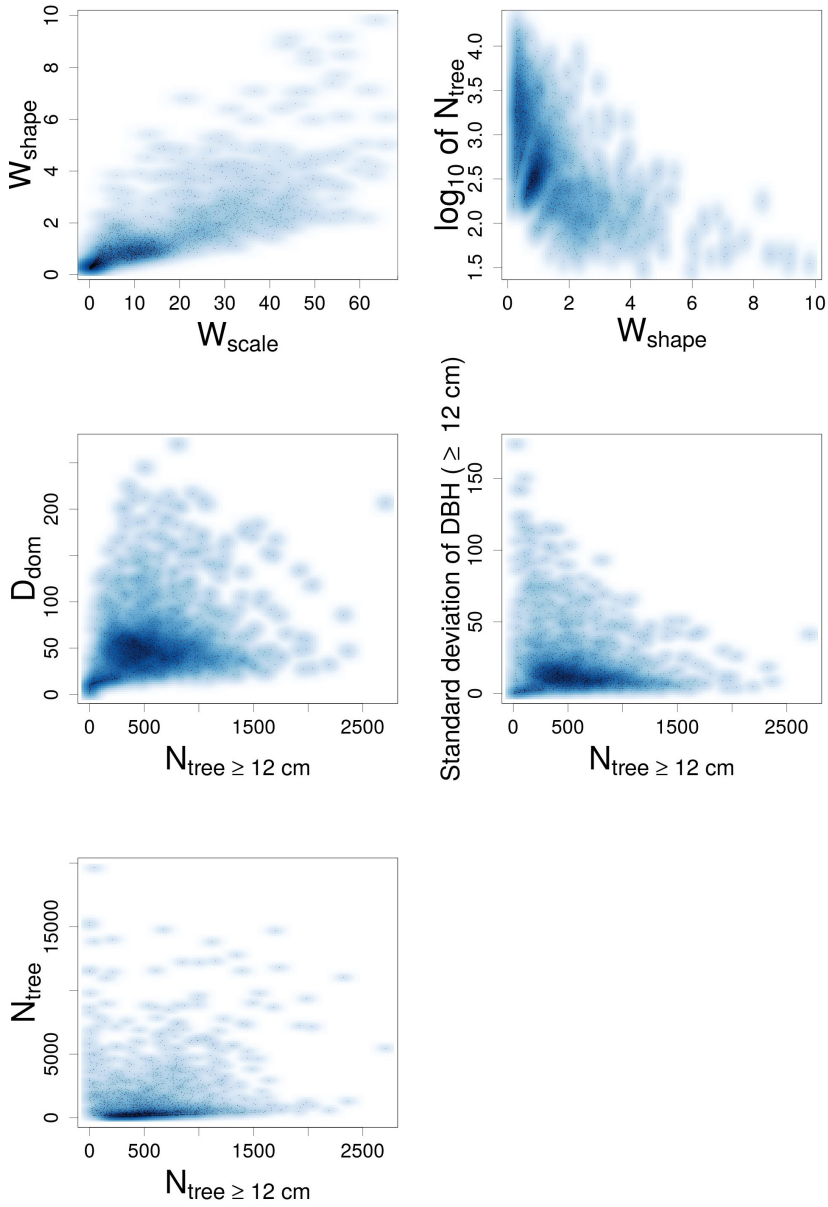

Figure 2.7: Derived stand parameters from National Forest Inventories (NFI) data and their relationship to each other.

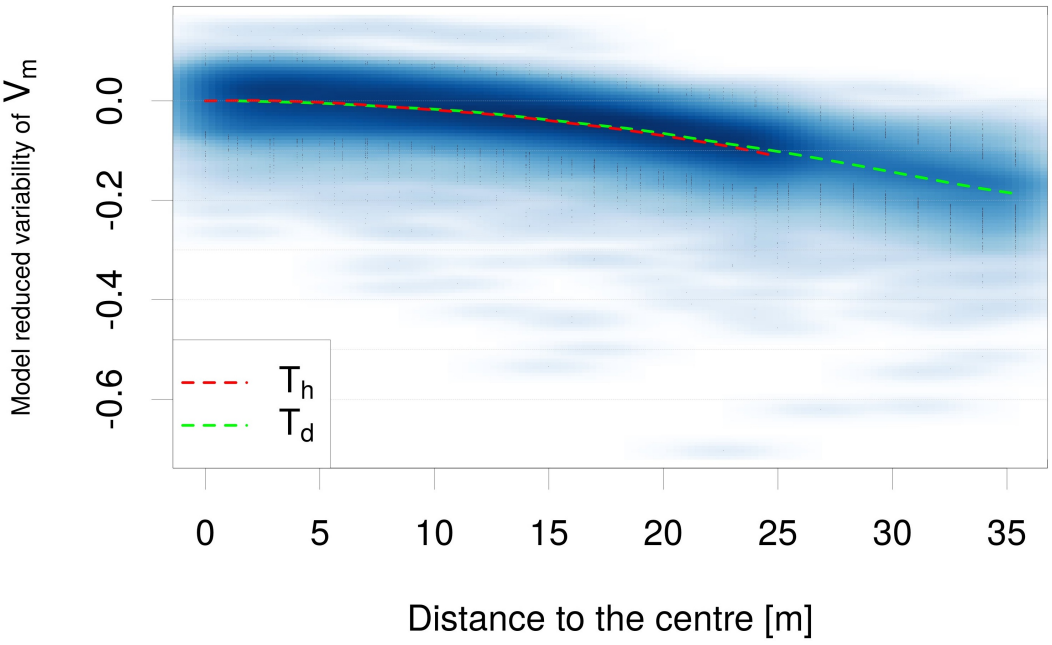

Figure 2.8: Reduction in visibility within the sample plot due to increased distance of the scanner location from the plot centre. V_m is reduced by the influence of the stand parameters and normalised to the mean V_m of the scans in the plot centre. T_h is the transect following the x-axis, T_d is the transect directing to a corner of the sample plot.

2.3.3 Influence of the Scanning Location within Sample Plots on Visibility in a 2D Space

To test the influence of the scanner position within the sample plot, we tested 51 scanner positions (see Figure 2.3). To confine computational cost, we reduced the dataset by using only the NFI plots surveyed in 2013, ending up with 537 different stand parameters. The regression of this reduced dataset leads to the same R^2 and to very similar coefficients and significance values (compare Table 3.3 earlier in the text with Table S2.2 in the Appendix 3.6). To test the influence of the scanner position within the sample plot, we added the distance to the plot centre (D_c) and a factor F_t which describes the kind of transect (horizontal or diagonal) the tested scanner position is situated on. The applied model is as follows:

$$\arcsin(\sqrt{V_m}) = log(N_{tree}) + log(W_{shape}) + log(D_{dom}) + log(N_{tree \geq 12cm}) + log(D_c) + log(D_c)^2 + F_t \quad (2.4)$$

All the added independent variables were significant, and the whole model showed an R^2 of 0.94. When reducing V_m by the influence of the stand parameters and the distance to the centre, the transect following the x-axis had on average, a V_m of 0.013 greater than that of the diagonal transect. Figure 2.8 shows the reduction in V_m caused by the distance to the centre.

2.3.4 Influence of Scanner Location Pattern on Visibility in a 2D Space

The combination of multiple scanner positions reduces the occlusion in a stand substantially (Newnham *et al.*, 2015; Dassot *et al.*, 2011; Bienert *et al.*, 2006; Liang *et al.*, 2016). Based on scanner location patterns found in the literature, we simulated 25 single scanning positions on each sample plot (n = 536) (see Figure 2.4) and combined

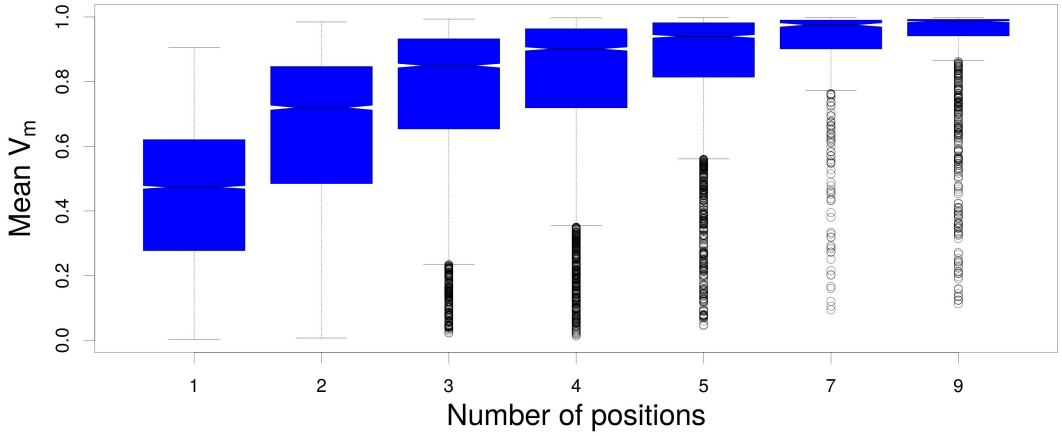

Figure 2.9: Influence of the number of combined scanning locations (N_s) on the mean visibility (V_m) within the plot.

them to form a total of 40 scanning location patterns (see Figures S2.2 and S2.3 in the Appendix 3.6).

Figure 2.9 shows the differences in the mean visibility V_m caused by varying the number of scanner positions. As one would expect, increasing the number of scans (N_s) has a positive influence on the quality of the point cloud by covering more of the sampled area. Our evaluations showed that the number of positions has a strong and significant influence on the mean visibility of the stand. We added the number of scanning locations (N_s) to the basic model (Equation (2.3)). The model produced an R^2 of 0.92. If we conduct the same procedure with the scanner location patterns (P_{sl}), the corresponding tested model has an R^2 of 0.94. Table 2.3 displays the mean visibility for each P_{sl}. Since P_{sl} includes N_s implicitly, these two R^2 figures imply that the kind of pattern chosen has an influence on the visibility within the stand as well. Figure 2.5 shows the change in visibility of the tested P_{sl} compared to a single scan in the centre of the sample plot. In the Appendix 3.6 we show, for each of the most efficient P_{sl}, the histrogram of visibility by classes of D_{dom} and N_{tree} (Figures S2.4–S2.9) . Following the findings given above, V_m becomes higher as more scans are combined and as N_{tree} becomes lower. Stem number class 3 (501 to 1000 trees per hectare) and 4 (more than 1000 trees per hectare) seem to be especially sensitive to the scanning regime.

Table 2.3: Changes in the mean visibility (V_m) influenced by scanner location pattern.

Scanner Location Pattern	Combined Locations	Mean V_m Mean V_m	Standard Deviation of V_m
0	32, 34	0.67	0.23
1	63, 61	0.69	0.24
2	42, 44	0.69	0.24
3	22, 24	0.65	0.25
4	51, 53	0.68	0.24
5	11, 13	0.52	0.26
6	11, 51	0.57	0.24
7	11, 0	0.63	0.25
8	11, 53	0.61	0.25
9	42, 32	0.68	0.24
10	42, 0	0.69	0.24
11	42, 34	0.69	0.24
12	0, 34, 32	0.72	0.22
13	0, 61, 63	0.78	0.23
14	0, 51, 53	0.78	0.23
15	0, 11, 13	0.71	0.26
16	53, 43, 52	0.75	0.23
17	53, 33, 52	0.77	0.23
18	53, 0, 52	0.77	0.23
19	53, 31, 52	0.77	0.23
20	53, 41, 52	0.78	0.23
21	31, 32, 33, 34	0.76	0.21
22	61, 62, 63, 64	0.84	0.21
23	41, 42, 43, 44	0.84	0.21
24	51, 52, 53, 54	0.84	0.21
25	11, 12, 13, 14	0.71	0.28
26	51, 62, 53, 64	0.84	0.21
27	51, 61, 53, 63	0.83	0.22
28	33, 43, 52, 62	0.81	0.22
29	11, 12, 13, 0	0.76	0.26
30	0, 31, 32, 33, 34	0.78	0.21
31	0, 41, 42, 43, 44	0.86	0.2
32	0, 51, 52, 53, 54	0.87	0.19
33	62, 51, 52, 53, 54	0.87	0.2
34	42, 51, 52, 53, 54	0.87	0.2
35	32, 51, 52, 53, 54	0.87	0.19
36	0, 41, 61, 62, 43, 63, 64	0.9	0.17
37	53, 43, 52, 44, 0, 42, 54, 41, 51	0.92	0.15
38	53, 43, 52, 44, 0, 42, 54, 41, 11	0.92	0.16
39	53, 43, 52, 44, 0, 42, 54, 41, 61	0.92	0.15

2.4 Discussion

2.4.1 Theoretical Coverage of a Laser Scanning System in a 3D Space

The first goal of this study was to test the link between scanner resolution and a minimum object size that could theoretically be detected without accounting for occlusion, given the assumption of an infinitesimally small laser beam. We provided a model which includes the independent variables "distance to the scanner" (D_e), "horizontal distance to the scanner" (D_h) and "ratio of object size to scanner resolution" ($R_{vs/sr}$), which enables calculation of the number of possible rays passing through a voxel with very high precision (R^2 of 0.99). The last bit of unexplained variation in the model possibly comes from the fact that the cross section of the voxel from the direction of the assumed scanner position varies, depending on the direction from which a voxel is scanned. Starting at ($R_{vs/sr}$) > 1, every object of the respective size obtains at least one hit by a laser ray in a 50 m cube. Below that value, the ratio between the number of voxels with at least one hit by a laser and the total number of voxels decreases in a close-to-linear s-shaped connection to $R_{vs/sr}$ (see Figure 2.6). As mentioned above, this experiment respects neither the influence of a laser beam divergence nor any effect of occlusion by other objects in the same scene. Nevertheless, a laser beam with an increasing diameter when crossing the forest scene can hit multiple objects at the same time, leading to various effects in respect to the obtained point clouds. Depending on the technology used, this can deliver point clouds with worse quality concerning the distance to the object or, in the better case, can deliver multiple returns from one single laser pulse. However, this experiment can support decisions for a field campaign concerning the size of the object of interest and the corresponding minimal scanner resolution. Findings from this experiment allow users to calculate in advance the maximum possible number of laser beams hitting an object of a specific size in any direction and distance to the scanner. This is especially important for measurements of tree parts which scanners cannot be placed close to, e.g., branches higher up in the canopy. For these objects, only multiple TLS measurements can improve the coverage, albeit in a linear fashion. Newnham et al. (Newnham *et al.*, 2015) identify two different categories of data retrieval approaches from TLS generated point clouds: gap probability and geometrical modelling. While the former approach samples the forest scene to provide a complement of all vegetation components, the latter uses the discrete point clouds to derive geometrical properties of the scanned object, e.g., by quantitative structure modelling (QSM) (Raumonen *et al.*, 2013; Hackenberg *et al.*, 2014). The suitability of geometrical modelling depends on a sufficient point based representation of an object in order to infer the geometric properties. Our results suggest that geometric modelling is more suitable for the lower forest layer(s), while in the top layers the point density might be too low simply because of the (vertical) distance to the scanner, not even considering occlusion.

2.4.2 Influence of Stand Parameters on Visibility in a 2D Space

The experiment to explore the influence of stand parameters on visibility showed that the Weibull parameter "shape" (W_{shape}) has a significant influence on V_m of a stand. The number of trees (N_{tree}), the mean diameter of the 100 largest trees per hectare (D_{dom}) and the number of trees with a DBH of $\geq$12 cm ($N_{tree \geq 12cm}$) show a highly significant influence as well. On the other hand, the Weibull "scale" parameter

(W_{scale}) in combination with the above-mentioned stand parameters has no influence. The standardised model coefficients, shown in Table 3.3, reveal the magnitude and the direction of the influence. The number of trees clearly has the strongest (negative) influence, followed by the W_{shape} parameter and D_{dom}. Surprisingly, $N_{tree \geq 12cm}$ has a positive relationship with V_m. A reason for this finding could be that there is some interaction with the other variables that alleviates their influence slightly. However, the standardised model coefficient shows that this influence is very small and not relevant. The independent variables of the model based on NFI data have a very high variability, due to the fact that only a few trees of a stand are located within the NFI sample plot. Their occurrence is subject to a stochastic process. This means that the stand description derived from the NFI data is not the actual description of the stand, but an unbiased expectation over a large sample of plots. The possible variety of stands that could occur is covered, or even goes beyond realistic occurrences. In the experiments of this publication, other influences are not considered, such as uneven terrain, lying dead wood or foliage, twigs and branches. However, twigs and branches might have a similar influence on visibility as a high number of small (stem) cylinders.

The assessment of visibility in this experiment is based on range measurements of geometric vectors with an infinitesimally small diameter. Especially when small objects with unsuitable angular resolution are scanned, a fraction of these objects would theoretically be invisible for the laser scanner (Figure 2.6). As mentioned above, laser pulses of any TLS device have a starting diameter and a beam divergence. Due to this increasing diameter (footprint) of the laser beam, a single laser pulse can hit multiple objects at the same time. Therefore, small objects would often be hit by a laser beam with a footprint, which could lead to noise or additional information in the acquired point cloud depending on the LiDAR technology of the TLS device (phase shift or time of flight). Kükenbrink et al. (Kükenbrink *et al.*, 2016) noticed an overestimation of occluded volume when laser scanning data were simulated using an infinitesimally small laser beam diameter.

The applied model (Equation (2.3)) shows a relatively high adjusted R^2 of 0.96. The unexplained variation might arise from the location of the scanner with respect to its neighbouring trees (cylinders) or might be due to the placement process of the cylinders. In this study, we chose a Poisson process to place them. Theoretically, it would be possible to apply so called "point processes", which are based on empirical data of tree distributions, to which the NFI data cannot contribute, due to the small sample plot size (Stoyan & Stoyan, 1998; Law *et al.*, 2009; Penttinen *et al.*, 1992). Even though the Weibull distribution is a common choice to describe diameter distributions of stands (Bailey & Dell, 1973), it does not encompass distributions with more than one local maximum, as described in (Trochta *et al.*, 2013). This experiment supports the assumption that, on the one hand, the number of objects and, on the other hand, the size of the objects, represented as D_{dom} and W_{shape}, influence visibility the most. With the derived formulas, we are now able to assess the extent of the influence of these stand parameters in advance. The experiment was conducted in a 2D space. This is useful for any application that is applied in such a setting, for example certain methods of stem detection or DBH derivation, as described by (Simonse *et al.*, 2003; Bienert *et al.*, 2006; Yao *et al.*, 2011; Hopkinson *et al.*, 2004; Kelbe *et al.*, 2012). However, most current methods of feature extraction are based on 3D point clouds, so it is questionable to what extent the findings of this 2D experiment can be transferred to a 3D space.

What kinds of stands are covered by the Weibull parameters used here? The Weibull distribution with a shape parameter (W_{shape}) of 1 describes an exponential distribution, whereas with W_{shape} 3.6 it follows a normal distribution. With a larger W_{shape}, the distribution becomes more negatively skewed. Figure 2.7 illustrates the combinations of W_{shape} with W_{scale} and N_{tree}. The plots show that the simulated stands include typical regeneration stands with a large number of trees (low W_{shape}, low W_{scale}), uneven-aged stands (W_{shape} around 3.6 and large W_{scale} around 50) to relatively even-aged mature stands (large W_{shape}, large W_{scale}). These Weibull parameters are based on the same data that were used to produce the online publication of the Swiss NFI results (Abegg *et al.*, 2014).

2.4.3 Influence of the Scanning Location within Sample Plots on Visibility in a 2D Space

By simulating different scanning locations, we showed the effect of the scanner placement within a sample plot on occlusion and coverage. We proved that the most efficient location to place a scanner in a single-scan setup is the centre of a sample plot, as one would intuitively assume. The mean visibility (V_m) within the plot decreases when the scanner is placed at an increasing distance from the plot centre. Whether the scanner is moved towards an edge or to a corner only makes a small difference. The reason for this effect is that the further away the scanner is from the plot centre, the longer the distance a laser beam has to travel to scan the opposite side of the sample plot and the more likely it is that the beam is intercepted by tree trunks. A limitation of this experiment was that no location outside of the plot was tested. In a continuous forest, the effect of increasing occlusion is very likely to continue with larger distances. If the stand is isolated in a non occlusive surrounding, the outside view may not lose visibility because no additional occluding objects will cross the view line of the scanner. Figure 2.8 shows the remaining unexplained variation of the mean visibility V_m. This could be either due to the random placement of the cylinders or due to the placement of the scanner relative to its nearest neighbouring cylinders, as mentioned above.

2.4.4 Influence of Scanner Location Pattern on Visibility in a 2D Space

With the fourth experiment, we tested the influence of multiple scanning locations on the visibility within sample plots. We evaluated 40 scanning location patterns and showed that, on average, every additional scan increased the visibility (see Figure 2.9). However, there is a saturation effect: for larger numbers of combined scans, the additional gain in V_m decreases. Nevertheless, the different patterns of scanner positions showed considerable differences in efficiency (see Figure 2.5). The least favourable pattern is scanning from the edge (as with P_{sl} 5 or 25, see Figures S2.2 and S2.3), which leads to a strong reduction in visibility. Similarly, very close P_{sl} (as in P_{sl} 0, 21 or 30) seem to deliver a low visibility compared to other patterns. Another loss of efficiency, though not to the same extent as those mentioned above, seems to occur with an uneven distribution of scanning locations over the sample plot (as in P_{sl} 6, 16 or 28). From P_{sl} 16 to 20, such an unevenness decreases continuously and efficiency increases. Minor shifts of a few metres (as in P_{sl} 18 to 19 or 9 to 10 to 11) do not worsen V_m notably. Even more severe shifts of the central position, as tested in P_{sl} from 32 to 35, do not show relevant changes in efficiency.

As an overall conclusion from the analysis of the scanner location patterns, the following rule of thumb could be inferred: an even distribution of scanner locations over the sample plot with even distances to the edge of the sample plot and to other scanner locations delivers the best visibility of the stand. Additionally, a local adjustment of the scanner location aimed at increasing the distance to the closest surrounding trees would not affect V_m; on the contrary, it would likely bring a gain in efficiency, as (Hilker *et al.*, 2012) stated.

2.5 Conclusions

In this study, we investigated the maximal possible coverage of a TLS device in a 50 m cubic voxel space. Additionally, using NFI Data and a 3D content creating suite, we analysed the influence of stand parameters, the scanning location within a sample plot and scanner location patterns on the visibility within a sample plot of 50×50 m.

We found a close relationship between the number of infinitesimally small laser beams hitting an object and the angular scanner resolution, the object size, and the distance to the scanner. These findings will help to exclude unrealistic expectations in TLS measurements. The number of trees clearly has the strongest influence on the visibility of a sample plot. Parameters with the second and third strongest influence on visibility are the shape of the Weibull distribution and the mean diameter at breast height of the 100 largest trees per hectare. These results suggest that, depending on the stand, different scanning settings might be necessary. The most efficient scanner location in terms of visibility is the centre of the sample plot. If multiple locations are used, our results show that an even distribution of the scanner locations over the sample plot, with even distances to the edge of the sample plot and to other scanner locations, delivers the best visibility for deriving properties of the stand. A local adjustment of the scanner location considering the surrounding trees could contribute to an even better visibility.

These findings will contribute to efficient TLS applications within forest inventories.

The following abbreviations are used in this article:

D_c	Horizontal distance to the centre of the sample plot
DBH	Diameter at breast height
D_{dom}	Diameter of the dominant (the largest) 100 trees per hectare
D_e	Euclidean distance from the voxel centre to the scanner location
D_h	Horizontal distance from the voxel centre to the scanner location
GIS	Geographical information system
LiDAR	Light detection and ranging
NFI	National Forest Inventory
N_{hits}	Number of rays (vectors) entering a voxel
N_s	Number of scanning locations combined to a scanner location pattern
N_t	Number of rays (vectors) that could enter a voxel without occlusion
N_{tree}	Number of trees per hectare with a minimal height of 1.3 m
$N_{tree \geq 12cm}$	Number of trees per hectare with a minimal DBH of 12 cm
P_{sl}	Scanner location pattern: The pattern multiple scanning locations are combined to scan a sample plot
$R_{vs/sr}$	Ratio of voxel size [m] to scanner resolution [°]
TLS	Terrestrial Laser Scanning
T_h	Horizontal transect within the sample plot. The transect following the positive x axis of the local coordinate system
T_d	Diagonal transect within the sample plot, ranging from the plot centre to the corner of the sample plot with coordinates (25,25)
V_m	Mean visibility of the sample plot
W_{scale}	Weibull scale parameter
W_{shape}	Weibull shape parameter

2.6 Supplementary Material

Table S2.1: Mean hits by (Euclidean) distance class and ratio voxel size to scanner resolution ($R_{vs/sr}$) class.

	$R_{vs/sr}$-Class					
	0–0.49	**0.5–0.9**	**1–4.9**	**5–9.9**	**10–49.9**	**>50**
Distance Class						
0–4.9	14.9	295	3203	30,744	279,571	4,653,479
5–9.9	1.8	41	457	4453	38,371	610,737
10–14.9	0.5	15	174	1695	14,538	230,408
15–19.9	0.2	8	93	909	7770	123,584
20–24.9	0.1	4	58	575	4945	78,485
25–29.9	0	3	40	400	3451	54,917
30–49.9	0	1	22	221	1913	30,431
$\geq$50	0	0	8	89	779	12,420

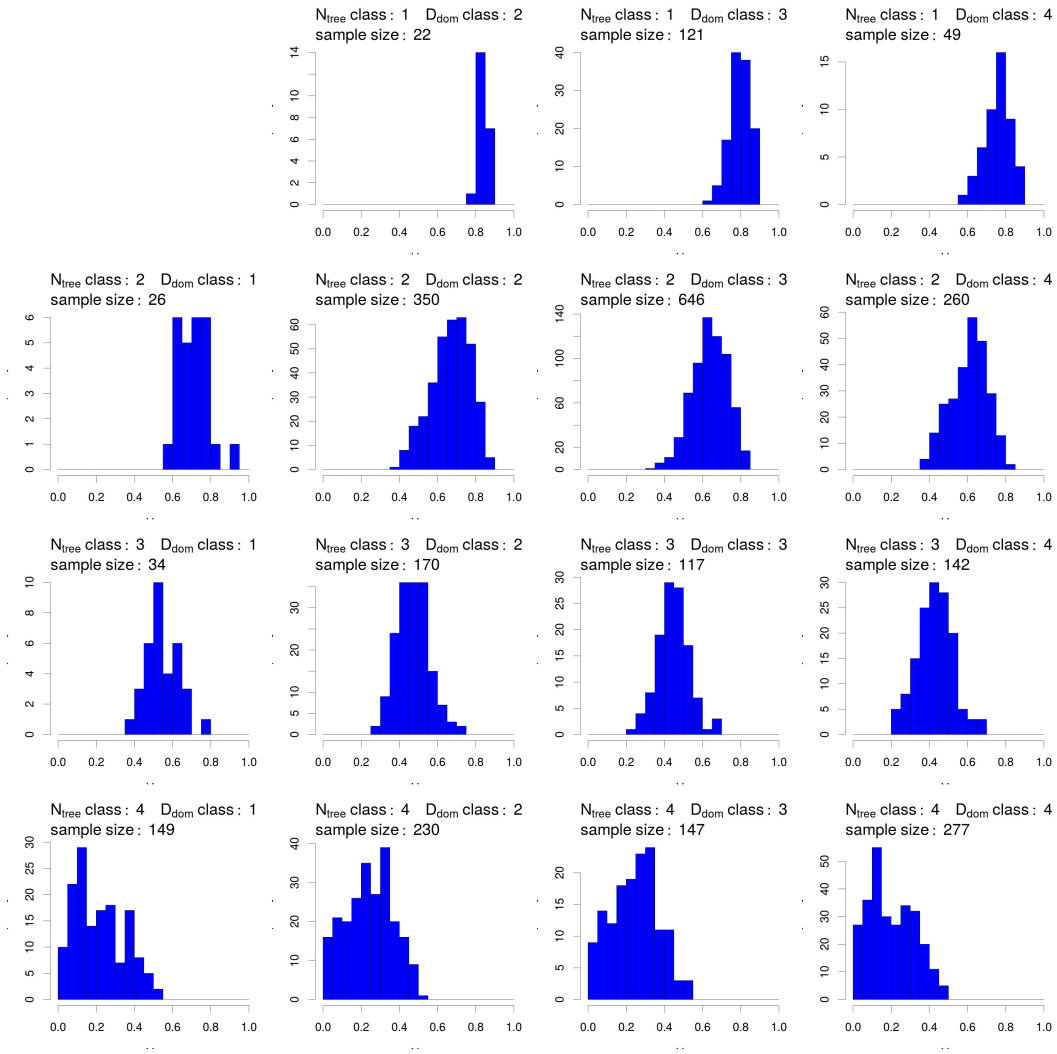

Figure S2.1: Visibility (V_m) by stand types. D_{dom} class 1 ($D_{dom} \leq 20$), D_{dom} class 2 ($D_{dom} > 20$ and ≤ 40), D_{dom} class 3 ($D_{dom} > 40$ and ≤ 60), D_{dom} class 4 ($D_{dom} > 60$), N_{tree} class 1 ($N_{tree} \leq 100$), N_{tree} class 2 ($N_{tree} > 100$ and ≤ 500), N_{tree} class 3 ($N_{tree} > 500$ and ≤ 1000), N_{tree} class 4 ($N_{tree} > 1000$).

Table S2.2: Model coefficients explaining V_m on a single annual NFI grid. $R^2 = 0.96$.

Variable	Model Coefficient	Standardised Model Coefficient	*p* Value
Intercept	2.781	0	<0.0001
$log(N_{tree})$	−0.251	−1.23	<0.0001
$log(W_{shape})$	−0.13	−0.408	<0.0001
$log(D_{dom})$	−0.123	−0.285	<0.0001
$log(N_{tree \geq 12cm})$	0.006	0.047	<0.0001

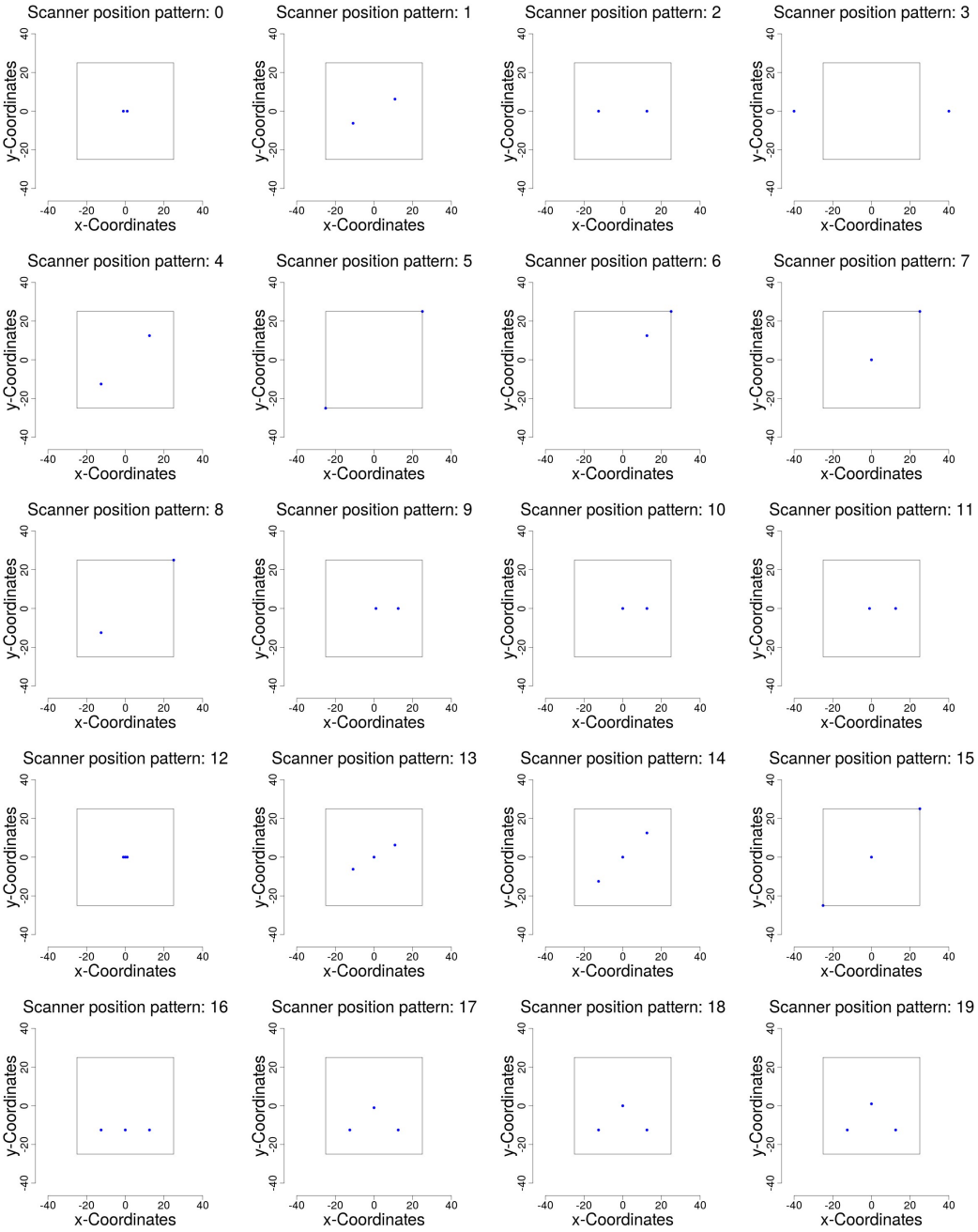

Figure S2.2: Tested scanner location patterns 0 to 19.

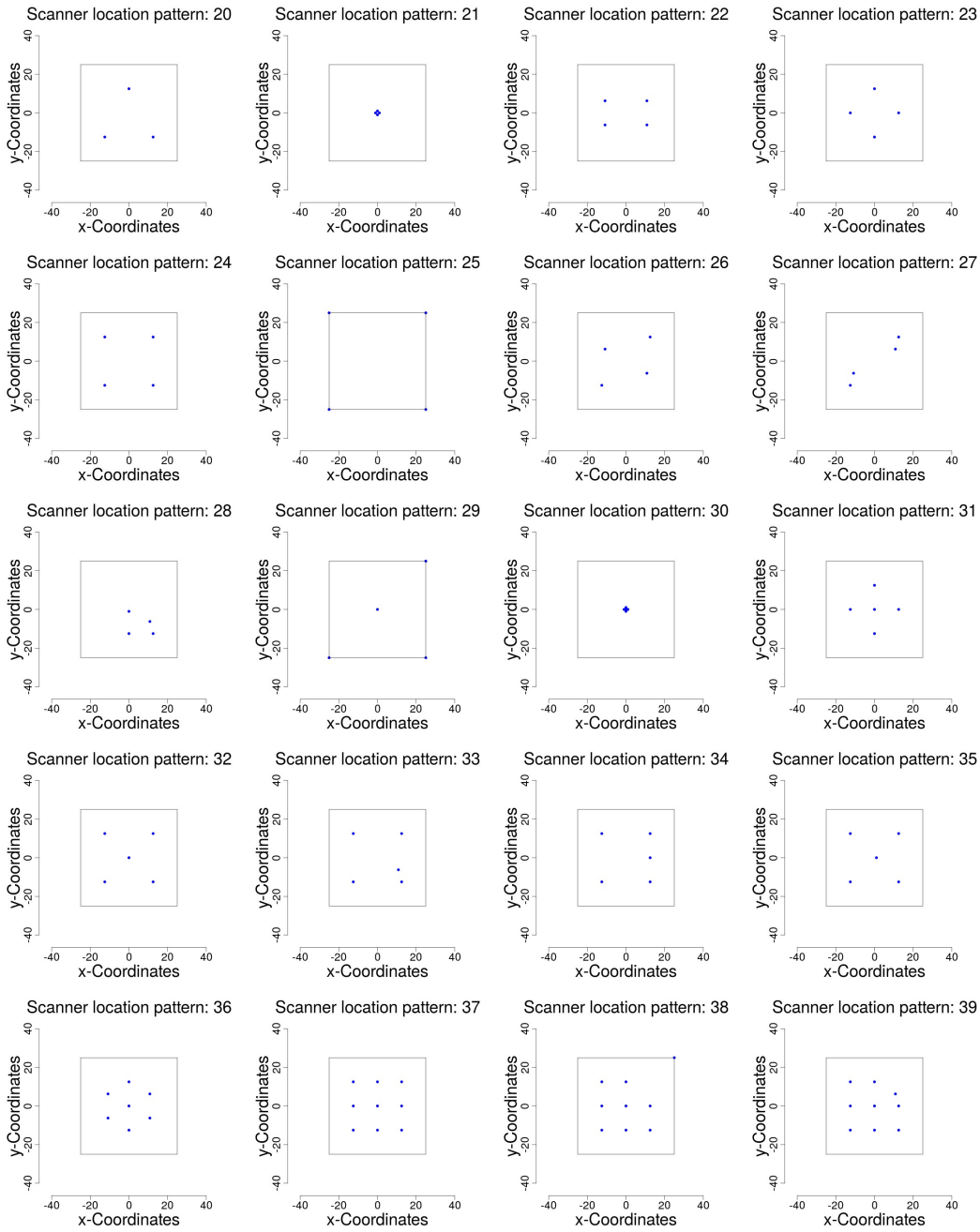

Figure S2.3: Tested scanner location patterns 20 to 39.

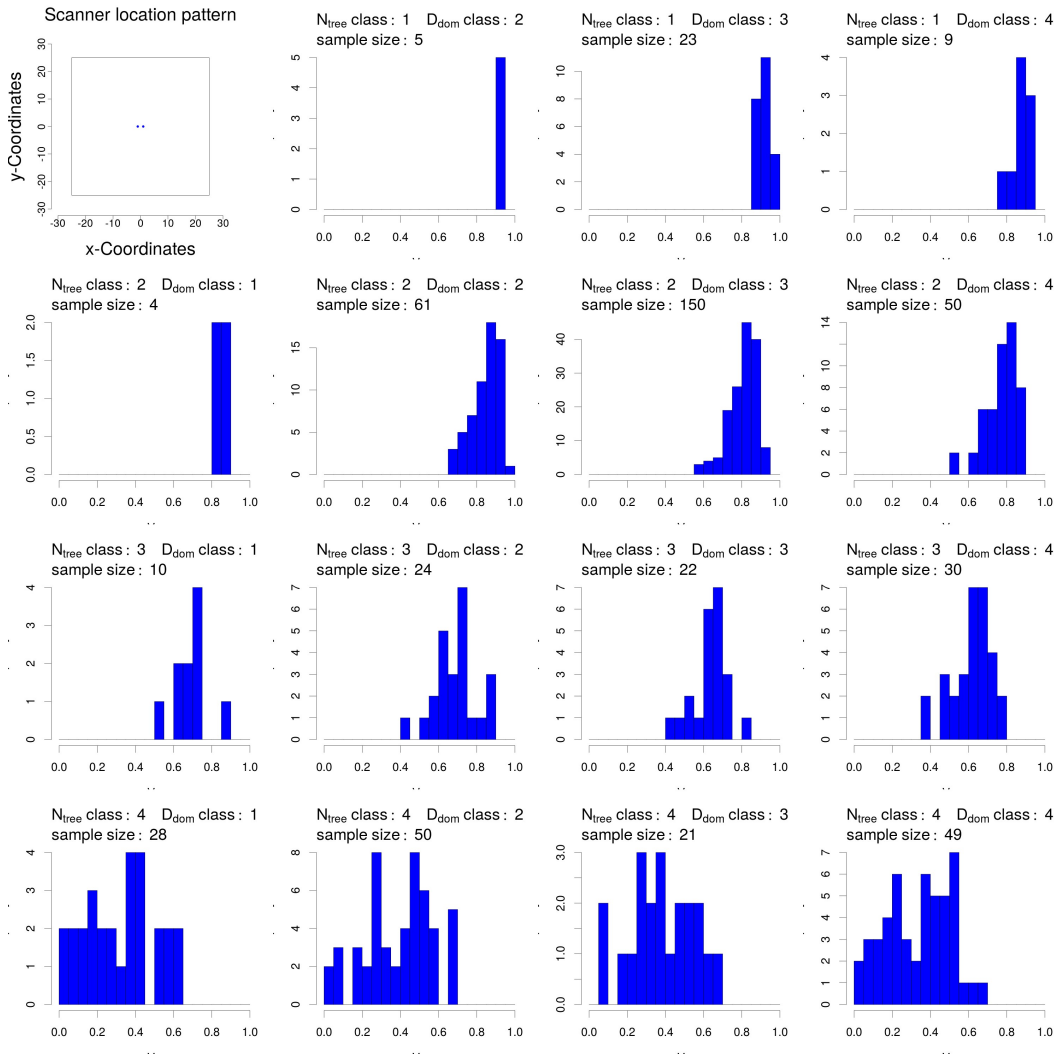

Figure S2.4: Visibility (V_m) of scanner location pattern 0 in dependence of D_{dom} class and stem number class. D_{dom} class 1 ($D_{dom} \leq 20$), D_{dom} class 2 ($D_{dom} > 20$ and $\leq$40), D_{dom} class 3 ($D_{dom} > 40$ and $\leq$60), D_{dom} class 4 ($D_{dom} > 60$), N_{tree} class 1 ($N_{tree} \leq 100$), N_{tree} class 2 ($N_{tree} > 100$ and $\leq$500), N_{tree} class 3 ($N_{tree} > 500$ and $\leq$1000), N_{tree} class 4 ($N_{tree} > 1000$).

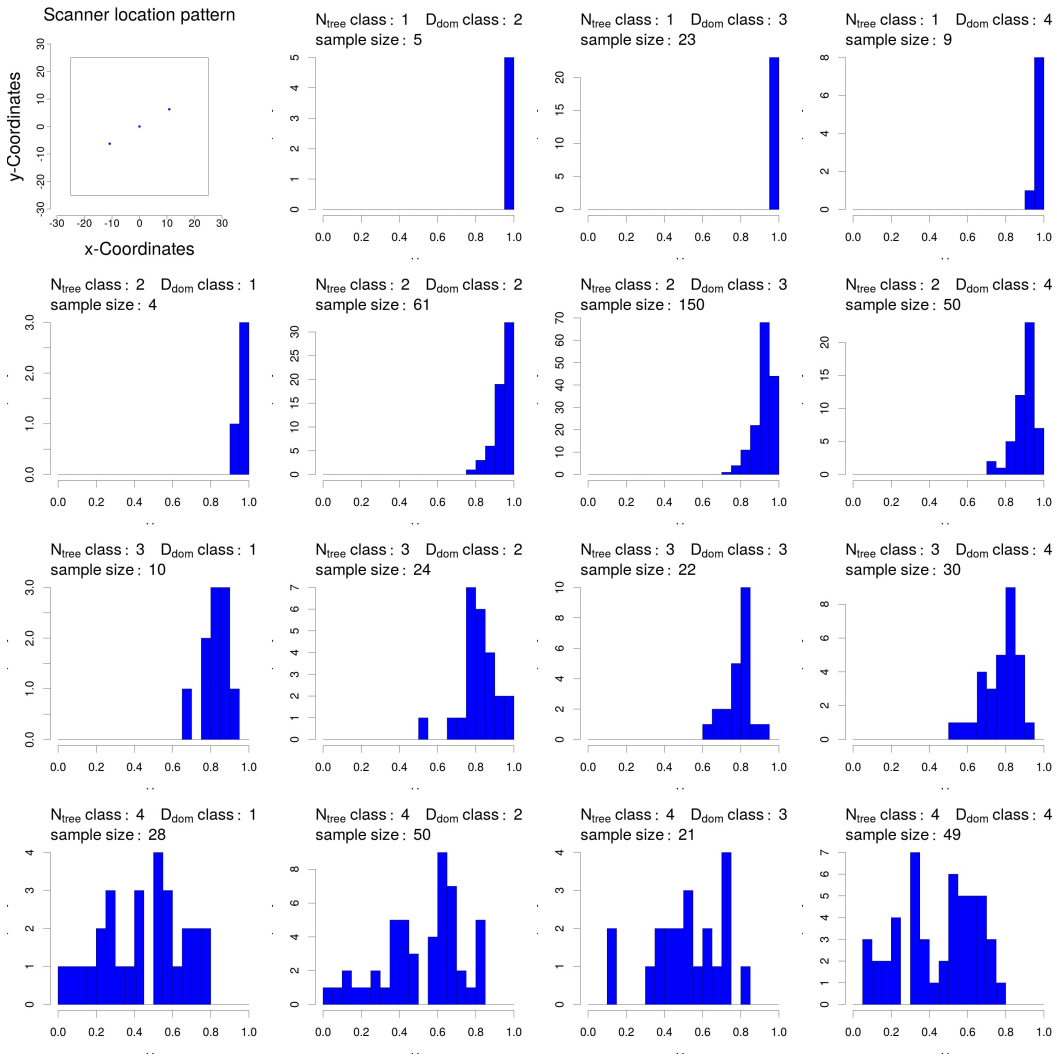

Figure S2.5: Visibility (V_m) of scanner location pattern 13 in dependence of D_{dom} class and stem number class. D_{dom} class 1 ($D_{dom} \leq 20$), D_{dom} class 2 ($D_{dom} > 20$ and $\leq$40), D_{dom} class 3 ($D_{dom} > 40$ and $\leq$60), D_{dom} class 4 ($D_{dom} > 60$), N_{tree} class 1 ($N_{tree} \leq 100$), N_{tree} class 2 ($N_{tree} > 100$ and $\leq$500), N_{tree} class 3 ($N_{tree} > 500$ and $\leq$1000), N_{tree} class 4 ($N_{tree} > 1000$).

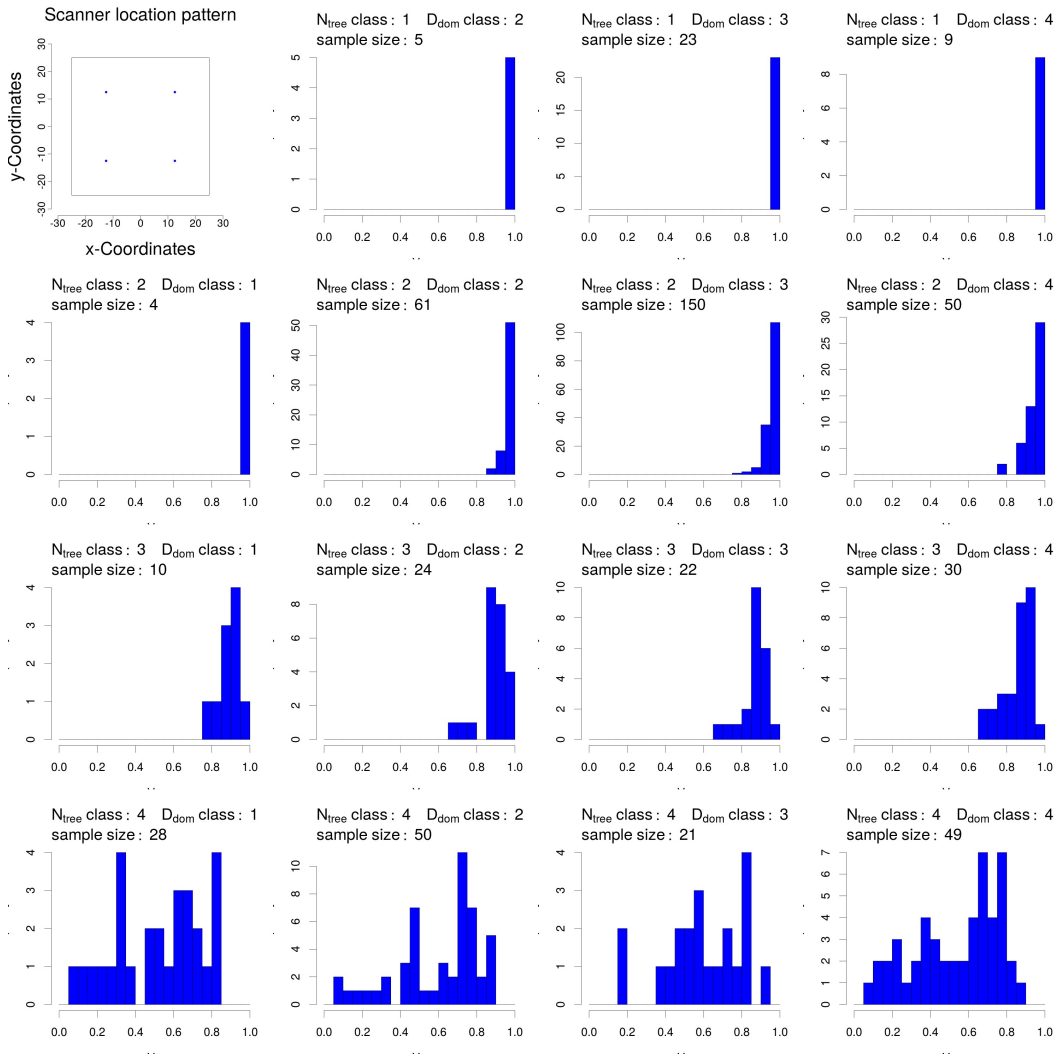

Figure S2.6: Visibility (V_m) of scanner location pattern 24 in dependence of D_{dom} class and stem number class. D_{dom} class 1 ($D_{dom} \leq 20$), D_{dom} class 2 ($D_{dom} > 20$ and $\leq$40), D_{dom} class 3 ($D_{dom} > 40$ and $\leq$60), D_{dom} class 4 ($D_{dom} > 60$), N_{tree} class 1 ($N_{tree} \leq 100$), N_{tree} class 2 ($N_{tree} > 100$ and $\leq$500), N_{tree} class 3 ($N_{tree} > 500$ and $\leq$1000), N_{tree} class 4 ($N_{tree} > 1000$).

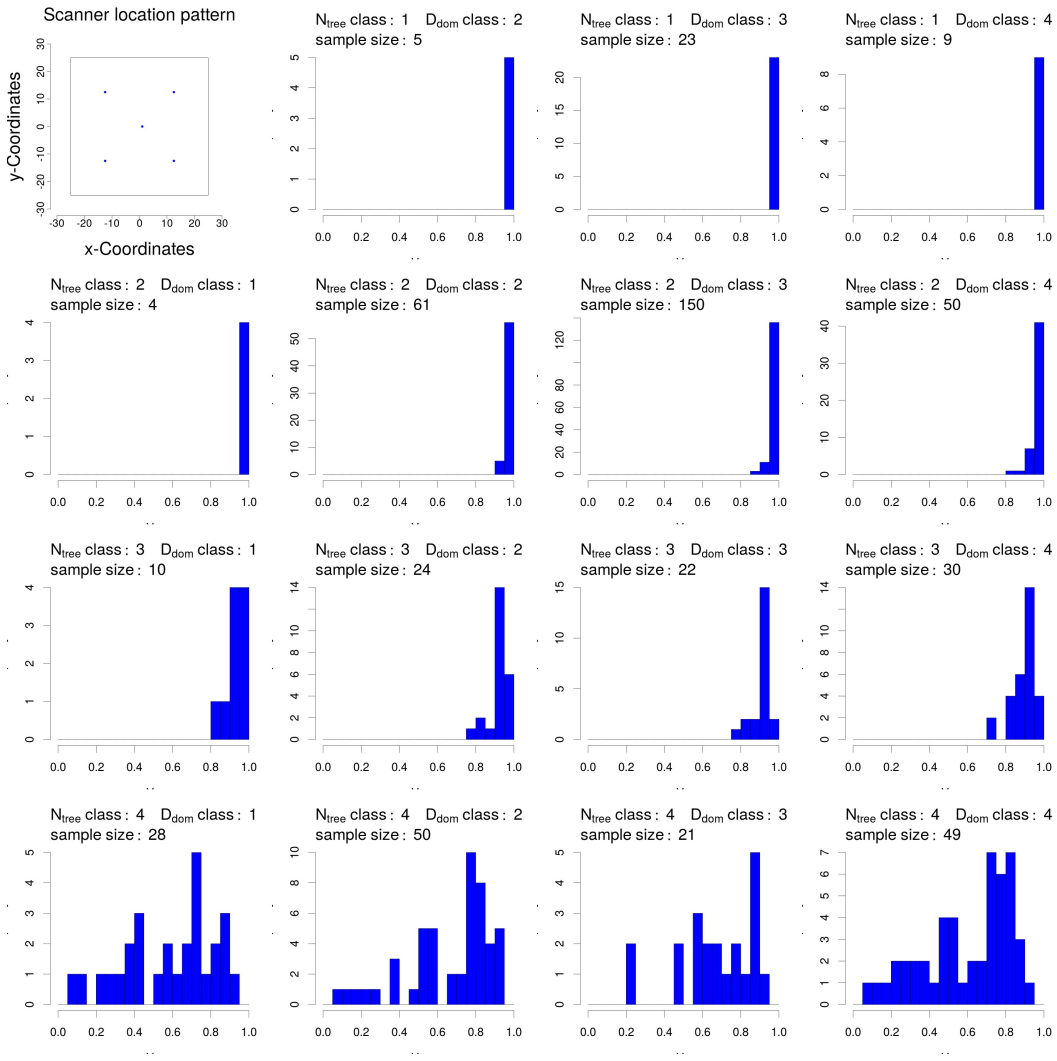

Figure S2.7: Visibility (V_m) of scanner location pattern 35 in dependence of D_{dom} class and stem number class. D_{dom} class 1 ($D_{dom} \leq 20$), D_{dom} class 2 ($D_{dom} > 20$ and $\leq$40), D_{dom} class 3 ($D_{dom} > 40$ and $\leq$60), D_{dom} class 4 ($D_{dom} > 60$), N_{tree} class 1 ($N_{tree} \leq 100$), N_{tree} class 2 ($N_{tree} > 100$ and $\leq$500), N_{tree} class 3 ($N_{tree} > 500$ and $\leq$1000), N_{tree} class 4 ($N_{tree} > 1000$).

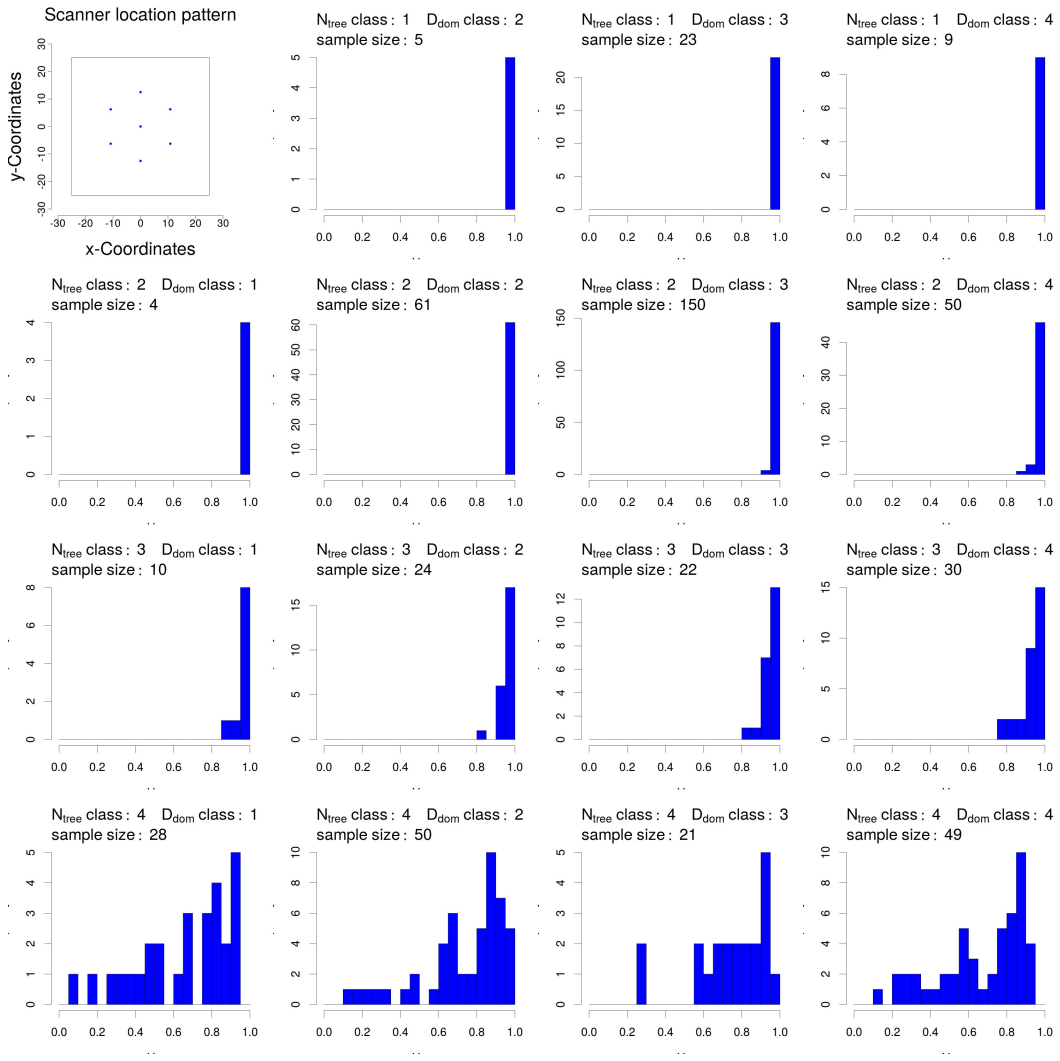

Figure S2.8: Visibility (V_m) of scanner location pattern 36 in dependence of D_{dom} class and stem number class. D_{dom} class 1 ($D_{dom} \leq 20$), D_{dom} class 2 ($D_{dom} > 20$ and $\leq$40), D_{dom} class 3 ($D_{dom} > 40$ and $\leq$60), D_{dom} class 4 ($D_{dom} > 60$), N_{tree} class 1 ($N_{tree} \leq 100$), N_{tree} class 2 ($N_{tree} > 100$ and $\leq$500), N_{tree} class 3 ($N_{tree} > 500$ and $\leq$1000), N_{tree} class 4 ($N_{tree} > 1000$).

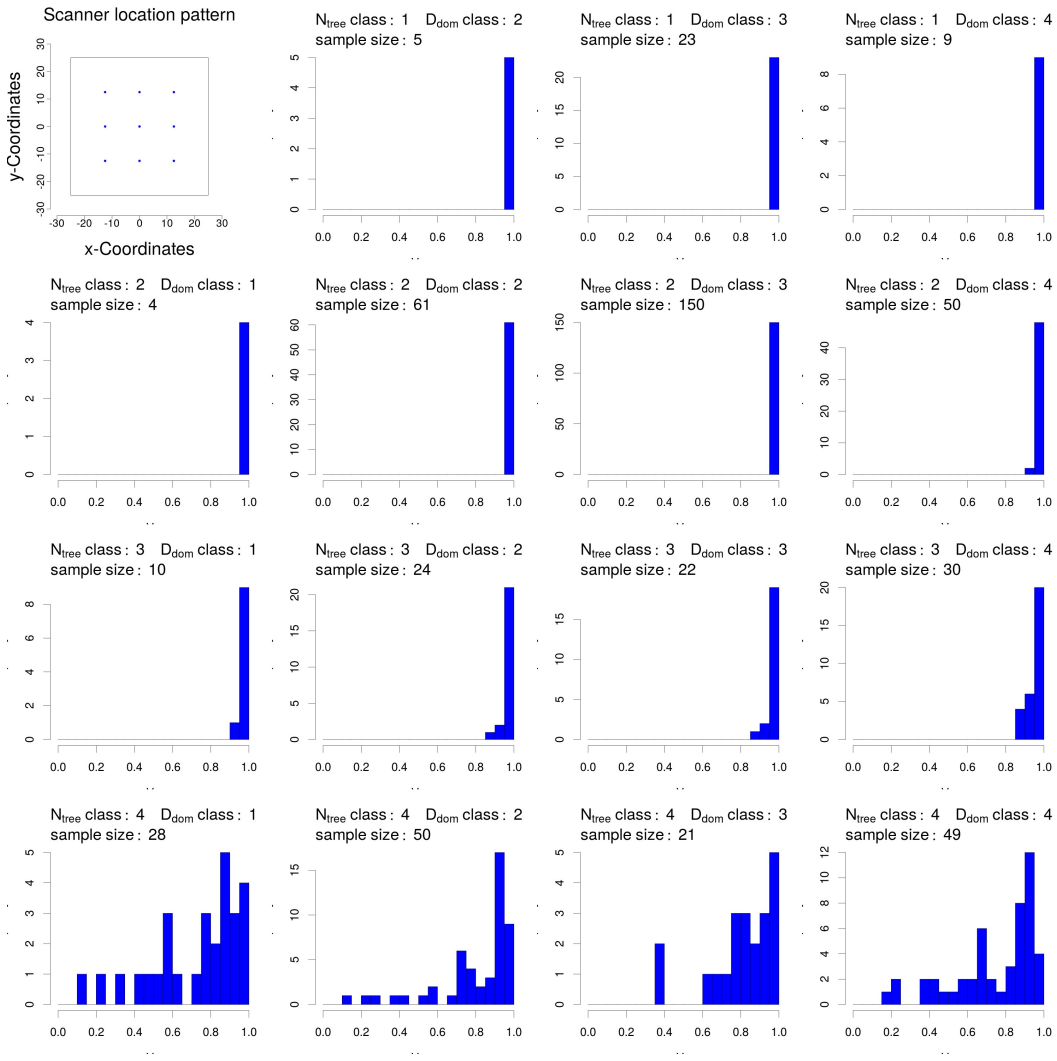

Figure S2.9: Visibility (V_m) of scanner location pattern 37 in dependence of D_{dom} class and stem number class. D_{dom} class 1 ($D_{dom} \leq 20$), D_{dom} class 2 ($D_{dom} > 20$ and $\leq$40), D_{dom} class 3 ($D_{dom} > 40$ and $\leq$60), D_{dom} class 4 ($D_{dom} > 60$), N_{tree} class 1 ($N_{tree} \leq 100$), N_{tree} class 2 ($N_{tree} > 100$ and $\leq$500), N_{tree} class 3 ($N_{tree} > 500$ and $\leq$1000), N_{tree} class 4 ($N_{tree} > 1000$).

2.7 References

(2012) *Silvilaser 2012*. Vancouver, Canada.

Abegg M, Brändli UB, Cioldi F, *et al.* (2014) Viertes schweizerisches landesforstinventar - ergebnistabellen und karten im internet zum lfi 2009-2013 (lfi4b).

Amanatides J, Woo A (1987) A fast voxel traversal algorithm for ray tracing. *Proceedings EUROGRAPHICS 87*, pp. 3 – 10.

Antonarakis AS (2011) Evaluating forest biometrics obtained from ground lidar in complex riparian forests. *Remote Sensing Letters*, **2**, 61–70.

Bailey RL, Dell TR (1973) Quantifying diameter distributions with the weibull function. *Forest Science*, **19**, 97 – 104.

Bienert A, Scheller S, Keane E, Mullooly G, Mohan F (2006) Application of terrestrial laser scanners for the determination of forest inventory parameters. In: *Commission V Symposium 'Image Engineering and Vision Metrology'*, vol. XXXVI part 5 of *International Archives of the Photogrammetry, Remote Sensing and Spatial Information Sciences*, p. 5. Dresden, Germany.

Binney J, Sukhatme GS (2009) 3d tree reconstruction from laser range data. In: *Robotics and Automation, ICRA'09 IEEE international Conference*. Kobe, Japan.

Blender Online Community (2015) *Blender - a 3D modelling and rendering package*. Blender Foundation, Blender Institute, Amsterdam.

Brassel P, Lischke H (2001) *Swiss National Forest Inventory: Methods and Models of the Second Assessment*. WSL Swiss Federal Research Institute, Birmensdorf, Switzerland.

Calders K, Newnham G, Burt A, *et al.* (2015) Nondestructive estimates of above-ground biomass using terrestrial laser scanning. *Methods in Ecology and Evolution*, **6**, 198 – 208.

Côté JF, Fournier RA, Frazer GW, Niemann KO (2012) A fine-scale architectural model of trees to enhance lidar-derived measurements of forest canopy structure. *Agricultural and Forest Meteorology*, **166-167**, 72–85.

Dassot M, Constant T, Fournier M (2011) The use of terrestrial lidar technology in forest science: application fields, benefits and challenges. *Annals of Forest Science*, **68**, 959–974.

Disney M, Lewis P, Raumonen P (2012) Testing a new vegetation structure retrieval algorithm from terrestrial lidar scanner data using 3d models. In: Sil (2012).

Eysn L, Pfeifer N, Ressl C, Hollaus M, Grafl A, Morsdorf F (2013) A practical approach for extracting tree models in forest environments based on equirectangular projections of terrestrial laser scans. *Remote Sensing*, **5**, 5424 – 5448.

Fisher PF (1991) First experiments in viewshed uncertainty: The accuracy of the viewshed area. *Photogrammetric Engineering and Remote Sensing*, **57**, 1321 – 1327.

FOREST EUROPE (2015) *State of Europe's Forests 2015*. FOREST EUROPE.

Gaulton R, Danson F, Ramirez F, Gunawan O (2013) The potential of dual-wavelength laser scanning for estimating vegetation moisture content. *Remote Sensing of Environment*, **132**, 32 – 39.

Gschwandtner M, Kwitt R, Uhl A, Pre W (2011) Blensor: Blender sensor simulation toolbox. In: *Advances in Visual Computing: 7th International Symposium (ISVC 2011)*, vol. Volume 6939/2011 (eds. Bebis R, Boyle B, Parvin D, Koracin R, Chung, Hammoud R), pp. 199 – 208. Springer Verlag, Las Vegas, USA.

Hackenberg J, Morhart C, Sheppard J, Spiecker H, Disney M (2014) Highly accurate tree models derived from terrestrial laser scan data: A method description. *Forests*, **5**, 1069 – 1105.

Hilker T, Coops NC, Culvenor DS, Newham G, Wulder MA, Bater CW, Siggins A (2012) A simple technique for co-registration of terrestrial LiDAR observations for forestry applications. *Remote Sensing Letters*, **3**, 239–247.

Hopkinson C, Chasmer L, Young-Pow C, Treitz P (2004) Assessing forest metrics with a ground-based scanning lidar. *Canadian Journal of Forest Research*, **34**, 573–583.

Kelbe D, Romanczyk P, vanAardt J, Cawse-Nicholson K, Krause K (2012) Automatic extraction of tree stem models from single rerrestrial lidar scans in structurally heterogeneous forest environments. In: Sil (2012), pp. 1–8.

Keller M (2011) *Swiss National Forest Inventory. Manual of the Field Survey 2004 - 2007*. Swiss Federal Research Institute WSL, Birmensdorf, Switzerland.

Kükenbrink D, Schneider FD, Leiterer R, Schaepman ME, Morsdorf F (2016) Quantificationof hidden canopy volume of airborne laser scanning data using a voxel traversal algorithm. *Remote Sensing of Environment*, **194**, 424 – 436.

Law R, Illian J, Burslem DFRP, Gratzer G, Gunatilleke CVS, Gunatilleke IAUN (2009) Ecological information from spatial patterns of plants: insights from point process theory. *Journal of Ecology*, **97**, 616 – 628.

Liang X, Hyyppä J (2013) Automatic stem mapping by merging several terrestrial laser scans at the feature and decision levels. *Sensors*, **13**, 1614 – 1634.

Liang X, Kankare V, Hyyppä J, *et al.* (2016) Terrestrial laser scanning in forest inventories. *ISPRS Journal of Photogrammetry and Remote Sensing*, **115**, 63 – 77.

Liang X, Kankare V, Yu X, Hyyppä J, Holopainen M (2014) Automated stem curve measurement using terrestrial laser scanning. *IEEE Transactions on Geoscience and Remote Sensing*, **52**, 1739 – 1748.

Lovell J, Jupp D, Newnham G, Coops N, Culvenor D (2005) Simulation study for finding optimal lidar acquisition parameters for forest height retrieval. *Forest Ecology and Management*, **214**, 398 – 412.

Maas HG, Bienert A, Scheller S, Keane E (2008) Automatic forest inventory parameter determination from terrestrial laser scanner data. *International Journal of Remote Sensing*, **29**, 1579–1593.

MacDicken K, Jonsson O, Piña L, *et al.* (2016) *Global Forest Resources Assessment 2015: How are the world's forests changing?* Food and Agriculture Organistation of the United Nations (FAO), Roma, Italy.

Mandallaz D (2006) *Sampling Techniques for Forest Inventories*. Chapman & Hall/CRC Applied Environmental Statistics. Chapman and Hall/CRC, Boca Raton, USA.

Mosteller F, Tukey JW (1977) *Data Analysis and Regression: A second course in statistics*. Addison-Wesley.

Newnham GJ, Armston JD, Calders K, *et al.* (2015) Terrestrial laser scanning for plot-scale forest measurement. *Current Forestry Reports*, **1**, 239 – 251.

Pan Y, Birdsey RA, Fang J, *et al.* (2011) A large and persistent carbon sink in the world's forests. *Science*, **333**, 988 – 993.

Penttinen A, Stoyan D, Henttonen HM (1992) Marked point prprocess in forest statistics. *Forest Science*, **38**, 806 – 824.

R Core Team (2017) *R: A Language and Environment for Statistical Computing*. R Foundation for Statistical Computing, Vienna, Austria.

Raumonen P, Kaasalainen M, Akerblom M, *et al.* (2013) Fast automatic precision tree models from terrestrial laser scanner data. *Remote Sensing*, **5**, 491–520.

Shvidenko A, Barber CV, Persson R (2005) *Forest and Woodland Systems*, chap. 21, pp. 585 – 621. Island Press.

Simonse M, Aschoff T, Spiecker H, Thies M (2003) Automatic determination of forest inventory parameters using terrestrial laser scanning. In: *Proceedings of the ScandLaser Scientific Workshop on Airborne Laser Scanning of Forests*, pp. 251–257. Umeå, Sweden.

Stoyan D, Stoyan H (1998) Non-homogeneous gibbs process models for forestry - a case study. *Biometrical Journal*, **40**, 521 – 531.

Thies M, Pfeifer N, Winterhalder D, Gorte B (2006) Three-dimensional reconstruction of stems for assessment of taper, sweep and lean based on laser scanning of standing trees. *Scandinavian Journal of Forest Research*, **19**, 571–581.

Tomppo E, Gschwantner T, Lawrence M, McRoberts RE (2010) *National Forest Inventories*. Springer.

Travis MR, Elsner GH, Iverson WD, Johnson CG (1975) Viewit: computation of seen areas, slope, and aspect for land-use planning. Tech. rep., Pacific Southwest Research Station, Forest Service, U.S. Department of Agriculture, Berkeley, California.

Trochta J, Kral K, Janik D, Adam D (2013) Arrangement of terrestrial laser scanner positions for area-wide stem mapping of natural forests. *Canadian Journal of Forest Research*, **43**, 355 – 363.

Van der Zande D, Hoet W, Jonckheere I, van Aardt J, Coppin P (2006) Influence of measurement set-up of ground-based lidar for derivation of tree structure. *Agricultural and Forest Meteorology*, **141**, 147 – 160.

Van der Zande D, Jonckheere I, Stuckens J, Verstraeten WW, Coppin P (2008) Sampling design of ground-based lidar measurements of forest canopy structure and its effect on shadowing. *Canadian Journal of Remote Sensing*, **34**, 526 – 538.

Watt PJ, Donoghue DNM (2005) Measuring forest structure with terrestrial laser scanning. *International Journal of Remote Sensing*, **26**, 1437 – 1446.

Wezyk P, Koziol K, Glista M, Pierzchalski M (2007) Terrestrial laser scanning versus traditional forest inventory. first result from the polish forests. In: *ISPRS Workshop on Laser Scanning 2007 and SilviLaser 2007*, pp. 424 – 429.

Woodgate W, Armston JD, Disney M, *et al.* (2016) Quantifying the impact of woody material on leaf area index estimation from hemispherical photography using 3d canopy simulations. *Agricultural and Forest Meteorology*, **226 – 227**, 1 – 12.

Yang X, Strahler AH, Schaaf CB, *et al.* (2013) Three-dimensional forest reconstruction and structural parameter retrievals using a terrestrial full-waveform lidar instrument (echidna). *Remote Sensing of Environment*, **135**, 36 – 51.

Yao T, Yang X, Zhao F, *et al.* (2011) Measuring forest structure and biomass in new england forest stands using echidna ground-based lidar. *Remote Sensing of Environment*, **115**, 2965–2974.

Chapter

3

Impact of Beam Diameter and Scanning Approach on Point Cloud Quality of Terrestrial Laser Scanning in Forests

This chapter is based on the peer-reviewed article:
***Abegg, M.**, Bösch, R., Schaepman, M.E., Morsdorf, F. (under Review) Impact of Beam Diameter and Scanning Approach on Point Cloud Quality of Terrestrial Laser Scanning in Forests. IEEE Transactions on Geoscience and Remote Sensing.*
It is reprinted as the final submitted manuscript and has been modified to fit the layout of this thesis.

M. A. designed the experiments, performed the analysis and interpreted the results. R. B. contributed to the code of the laserbeam simulation, experimental design and content of the publication. M.E.S. contributed to the experimental design and content of the publication, F.M. contributed to the experimental design and analysis. All authors wrote and reviewed the manuscript with main contribution of M.A.

Abstract

In recent years, portable laser scanning devices and their applications in the context of forest mensuration have undergone rapid methodological and technological developments. Devices have become smaller, lighter and more affordable, whereas new data-driven methods and software packages have facilitated the derivation of information from point clouds. Thus, terrestrial laser scanning (TLS) is now well established and laser – object interactions have been studied using theoretical-, modeling- and experimental approaches. The representation of scanned objects in terms of accuracy and completeness is a key factor for successful feature extraction. Still, little is known about the influence of TLS and survey properties on point clouds in complex scattering environments such as forests. In this study, we investigate the influence of laser beam diameter and signal triggering on the quality of point clouds in forested environments. Based on Swiss National Forest Inventory data, we simulate TLS measurements in 684 virtual forest stands using a 3D content creation suite. We show that small objects lack sufficient representation in the point cloud and they are further negatively influenced by large laser beam diameters, dense stands and large distances from the scanning device. We provide simulations that make it possible to derive a rationale for decisions regarding the appropriate choice of TLS device and survey configuration for forest inventories.

3.1 Introduction

Forests cover more than 30% of the global land area, serving as a source of livelihood, protecting soil, water and infrastructure, holding more than 75% of the world's terrestrial biodiversity, and providing a multitude of ecosystem services (FAO, 2018; Shvidenko *et al.*, 2005). Notably, forests play a vital role in carbon storage (Pan *et al.*, 2011). To ensure sustainable management of forests, monitoring is crucial. Forest mensuration provides a large toolset to acquire information on forests, from remote sensing to field measurements on systematic grids in the case of forest inventories. Even though remote sensing covers many aspects of forest monitoring, field measurements are still essential, providing data not measurable by remote sensing or serving as ground truth to calibrate remote sensing products such as wall-to-wall maps of forest features (e.g., Waser *et al.*, 2017). However, certain forest features, such as light availability, crown size, forest structure and tree volume, are nearly impossible to measure with traditional approaches or only at a very high cost. They are based either on models (e.g., tree volume models) or on expert assessments (e.g., forest structure). The fast development of efficient and lightweight close range remote sensing technologies in recent years, such as terrestrial laser scanning (TLS) and their applications, raise the question of their applicability for forest mensuration, e.g., in forest inventories (Liang *et al.*, 2016).

New measurements must be evaluated in terms of efficiency, precision and the quality of the newly acquired forest information. For close-range scanning applications where ground-truth is difficult to acquire (Morsdorf *et al.*, 2018), one established way to evaluate this technology is the use of simulation approaches (Lovell *et al.*, 2005; Disney *et al.*, 2012; Van der Zande *et al.*, 2008; Binney & Sukhatme, 2009). Once a simulation environment is established, it is possible to test many configurations in short time frames. A major advantage of simulation is the possibility to conduct sensitivity studies by comparing different configurations of the same object (Hovi & Korpela, 2014). The simulation environment is merely an abstraction of reality and consequently the representativeness of the virtual scene and the implemented LiDAR technology has to be considered carefully.

The application of laser scanning technologies is dependent on many factors, such as laser geometry properties and the interaction of light with the object surface (Kukko & Hyyppä, 2007). Adams & Kerstens (1996) and (Newnham *et al.*, 2012) point to the phenomenon of "mixed pixels" (edge noise), which occur when a pulse emitted by a laser scanner hits more than one object in its path, may leading to false range measurements. Some authors (e.g., Wagner *et al.*, 2004; Jutzi & Stilla, 2005) describe different approaches for signal triggering in time-of-flight systems. (Newnham *et al.*, 2012) mention "range averaging" in phase-shift laser scanners in case of mixed pixel situations. Furthermore, some approaches exist to simulate the characteristics of various laser scanning technologies (e.g., Disney *et al.*, 2010; Kukko & Hyyppä, 2007),

but they are mostly focused on airborne laser scanning systems with large beam diameters and full waveform information (time-of-flight systems). The specific peculiarities of terrestrial laser scanners, phase shift or time-of-flight systems, working with small laser diameters are mostly unknown. Even though certain information, such as the intensity pattern of the LiDAR reflections is sometimes known (e.g., Kaasalainen *et al.*, 2008; Koenig *et al.*, 2013). These publications indicate that there is a gap between theory and real implementation in laser scanners regarding details in signal triggering. Additionally, producers of terrestrial laser scanners keep the technical details of the implemented LiDAR technology as industrial secrets.
The goal of this study is to use a simulation approach to understand specific effects, e.g., influence of signal triggering, diameter of the laser beam or size of the scanned object, on the application of terrestrial laser scanning (TLS) in complex environments, such as forests. We hypothesise that depending on certain properties of the LiDAR device, such as the diameter of the laser beam or the signal triggering approach, there are clear limits to the ability of point clouds to contain accurate geometric information on scanned objects.
In order to conduct this simulation study, we:
i) analyse the main "mixed pixel" effects of three TLS devices in experiments performed in a laboratory setting with respect to signal triggering, omission of echoes during scanning, and deviation of scan points from object surfaces
ii) integrate these system effects to a laser scanning simulation environment
iii) conduct a simulation study using different forest stand characteristics by simulating laser scanners with different laser beam diameters and signal triggering approaches (including distance deviation and filtering), ultimately leading to recommendations for suitable TLS objectives and detectable object (tree, branch) sizes.

3.2 Materials and Methods

3.2.1 Simulating laser scanning with Blender

Blender (Blender Online Community, 2015) is an open-source 3D content creation suite. It is designed to easily build digital 3D objects and their light-interaction properties. It usually generates photorealistic images or animations as output. Blender provides a large toolbox to define, manipulate and store 3D objects. As in one of our previous studies (Abegg *et al.*, 2017), we used Blender version 2.74 and fully controlled the simulation using python scripts (Version 2.7.13).
BlenSor is an add-on for Blender which allows access to an internal part of Blender and hence provides the basics to simulate various types of range scanners and other optical instruments (Gschwandtner *et al.*, 2011). It enables an efficient intersection of mathematical vectors (rays) with 3D objects defined in Blender, and returns the range

Table 3.1: Beam diameters and divergences of different devices according to the $1/e^2$ definition.

Device	Beam diameter at exit [mm]	Beam divergence [mrad]
Leica BLK360	3.80	0.68
FARO Focus^{3D} 120	4.24	0.27
Riegl VZ-1000	18.00	0.30

and the incidence angle on the object surface. Similar to Monte Carlo ray-tracing approaches (Szwarcbaum & Shaviv, 1976; Govaerts & Verstraete, 1998; Lewis, 1999), single rays of light (photons) can be traced on their way through a virtual scene.
If the geometric properties, i.e., the diameter at exit and the divergence, of the laser emitted by a laser scanning system are known, this ray-tracing capability can theoretically be used to simulate any kind of LiDAR sensor. To do so, multiple photons (light rays) can be sampled within one laser beam cone. Following an assumed distribution of energy (e.g., Gaussian-shaped), the sampling density can be varied within the laser beam. If it is known exactly how a laser scanner uses the backscattered light to trigger one or multiple echoes, an implementation in Blender enables a realistic laser scanning simulation.

3.2.2 Analysis of terrestrial laser scanners

3.2.2a Tested devices

We tested three different portable state-of-the-art terrestrial laser scanners with beam properties (beam diameter at exit and beam divergence), as displayed in Table 3.1. The Leica BLK360 uses the "time of flight enhanced by Waveform Digitizing technology" (Leica, 2017). It triggers one point per laser pulse and offers a field of view of $360°$ horizontally and $300°$ vertically. It measures 100 mm in diameter and 165 mm in height, with a weight of 1 kg. It has a range of 0.6 m up to 60 m (Leica, 2017). The FARO Focus^{3D} 120 is a phase shift system that sends out a modulated laser beam to trigger a single echo per direction. It offers a field of view of $360°$ horizontally and $305°$ vertically, leaving only a small spot beneath the scanner uncovered. Various scan parameters can be adjusted, including the angular resolution and the point cloud quality parameters. It measures 240 x 100 x 200 mm, with a weight of 5 kg. It has a range of 0.6 m up to 120 m (FARO, 2013). The Riegl VZ-1000 is a time-of-flight system, with the ability to capture multiple points per laser pulse and options to provide full wave data. It offers a field of view of $360°$ horizontally and $100°$ vertically. The scanner, measuring 200 x 203 x 308 mm and with a weight of 9.8 kg, has a wide range of adjustable settings, including pulse repetition frequency and angular resolution. It has a range of 2.5 m to 1,400 m (Riegl, 2015).

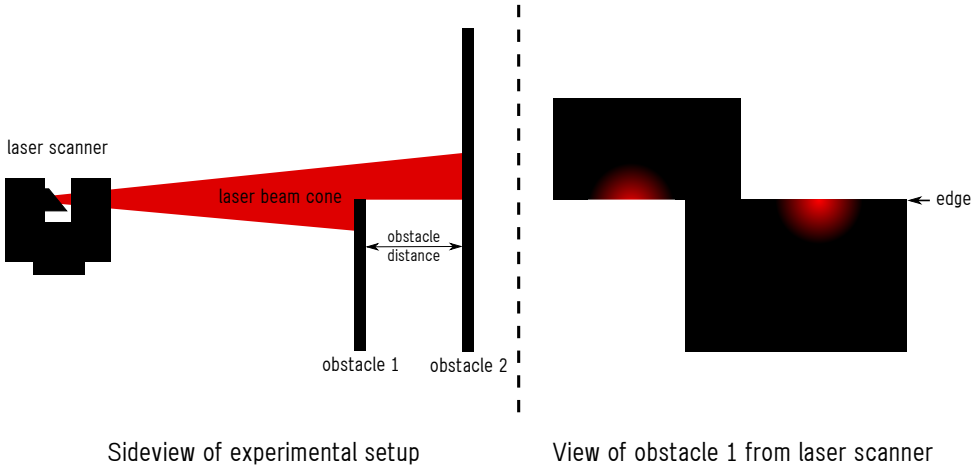

Figure 3.1: Setup of lab experiment to analyse edge noise effects of terrestrial laser scanners. Two obstacles are placed at a known distance ("obstacle distance") from each other, in such a way that effects on the point triggering of laser beam cones hitting the two objects can be analysed. Left: side view of the experimental setup, when a laser pulse intersects with obstacle 2 and the lower part of obstacle 1. Right: the footprint of two laser pulses on obstacle 1, both hitting the obstacles with approx. 50% of the beam energy. The laser pulses on the left (and top) part of obstacle 1 are only used to derive the height of the horizontal edge. The laser pulses on the right (and bottom) part are used for both, the derivation of the horizontal edge height and the analysis of the edge noise effects.

3.2.2b Experimental laboratory setup for the analysis of mixed pixel effects

We evaluated mixed pixel effects that emerge when two separated objects are intersected by one laser beam cone. This enables us to derive models of point triggering functionalities, and to describe the most important mixed pixel effects of the examined devices. As preparation, we conducted various test scans with different setups of obstacles at different distances to infer a suitable experimental setup. The final experimental setup is listed in Table 3.2. These setups capture the most important noise effects, previously observed in our data.
As depicted in Figure 3.1, we placed two objects in the field of view of the scanner, one (obstacle 1) closer to the scanner and the other (obstacle 2) farther away. Obstacle 1 has two horizontal edges at the same height, one is a top edge and the other is a bottom edge. Because edge noise in the point cloud at these edges is symmetric, the edge height can be derived from the point cloud directly by comparing the edge noise patterns at the bottom and the top edge. With the known beam diameter at the distance of the obstacle, the amount of laser beam energy hitting the two obstacles can be calculated. The obstacles' surfaces are white sheets of paper with an appropriate thickness to ensure a flat surface.

3.2.2c Model description of signal triggering

In this subsection, we describe the derivation of signal triggering models based on the lab experiments outlined in the previous section. Generalized for multiple obstacles,

Table 3.2: Setup of the obstacles for the lab experiments.

Device name	Distance scanner to obstacle 1 [m]	Obstacle distances [m]
Leica BLK360	3.59	0.07, 0.54, 1.95, 3.53, 5.28, 9.53
FARO Focus^{3D} 120	5.01	0.1, 0.2, 0.3, 0.4, 0.5, 0.6, 0.7, 0.8, 0.9, 1.0, 1.1, 1.2, 1.3, 1.4, 1.5, 1.6, 1.7, 1.8, 1.9, 2.0
Riegl VZ-1000	4.91	0.2, 0.4, 0.6, 0.7, 0.8, 0.9, 1.0, 1.1, 1.2, 1.4, 1.6, 1.8, 2.0

these models can be applied to a simulation study.
As mentioned in section 3.2.1, the LiDAR simulations, as applied in this study, can only make use of distance measurements to objects with the corresponding energy ratios of simulated laser beam cones hitting them. Hence, the models derived from the lab experiments also rely on these two parameters.
To know which points in the point cloud are based on laser pulses hitting the two objects, the energy ratio of the laser pulse on the two objects was calculated. For this purpose, the size of the laser footprint on the object must be known. Even though only explicitly provided for Riegl (Riegl, 2015) and partly for FARO (FARO, 2013), we assumed the laser beam of all three devices to be circular with a Gaussian-shaped energy distribution. As the three devices use different units to describe the laser beam diameter, we calculated them according to the "1/e^2" standard, as described in Equation 3.1. All the standards provide a means to describe the ratio of the maximally irradiating energy across a laser beam diameter, which is used to define the width between two opposite points where this irradiance ratio is reached.

$$D_{B_{(1/e^2)}} = \sqrt{2} D_{B_{(1/e)}} = 1.699 * D_{B_{(FWHM)}} \tag{3.1}$$

where $D_{B_{(1/e^2)}}$ is the diameter according to the "1/e^2" standard (max. irradiance/ e^2), $D_{B_{(1/e)}}$ according to the "1/e" standard (max. irradiance/ e) and $D_{B_{(FWHM)}}$ according to the "FWHM" standard (max. irradiance/ 2). Assuming a Gaussian-shaped energy distribution, the "1/e^2" range within the laser beam contains 95.45% of the energy, covering two times the standard deviation of the Gaussian-distributed energy.

By using a Gaussian distribution function with the expectation value (μ), the standard deviation (σ) and a quantile (q), the energy ratio on the objects can be derived.

3.2.2c.1 Leica BLK360 An examination of Leica BLK360 point clouds revealed noise in only very few exceptional cases and no noise at all in the specific setup of the lab experiments. Consequently, we did not derive a noise model. However, as we saw in our analysis (Figure 3.4), the Leica scanner only triggers one echo per laser pulse and does perform a filtering of the point cloud. Because the filtering is executed during the scanning, we refer to it as prefiltering to distinguish it from the filtering of the point cloud as part of processing after the scanning.
For our model derivation, we used laser pulses intersecting the two obstacles with an energy ratio slightly above twice the standard deviation of the energy distribution (from 2% to 98% of the laser beam energy on the two obstacles). A prefiltering model is represented by the probability that an echo (or signal) is triggered (referred to here as "signal triggering probability"). Thus, we derived a model for the signal triggering probability based on the Leica scanner lab data. To obtain the true value of the signal triggering probability, we built equal bins of vertical scan angles and counted the number of points in each bin. An approximation of the triggering probability equals the ratio of the point number per bin to the mean point number in bins without prefiltering. To derive a suitable model for the triggering probability, we only need to analyse the energy ratios $\geq$ 50% because if the energy ratio of the laser pulse on one of the two obstacles is lower, the point is triggered on the other object (or not at all). The basis for the signal triggering probability model is a logit function (see Equation 3.2), where p is the triggering probability and L is a function of the energy ratio of the laser on an obstacle.

$$p = \frac{1}{1 + e^{-L}} \tag{3.2}$$

The model was fit empirically in the following form, where E_l is the ratio of energy of the laser pulse on the object which obtains the most energy, D_o is the positive distance in meters to the closest neighbouring obstacle (and a minimal value of at least 1), α = 1.02, β = -0.11 and γ = 90. γ is used to stretch the model in the x-direction, whereas α and β shift the curve in the x-direction, both influencing the obstacle distance D_o.

$$p = \frac{1}{1 + e^{-(E_l - \alpha + \beta D_o)\frac{\gamma}{D_o}}} \tag{3.3}$$

3.2.2c.2 FARO Focus^{3D} 120 As Figure 3.2 indicates, the FARO scanner applies four different signal triggering functionalities:

i Common distance measurement: a single object placed within the laser beam cone

ii Distance deviation through lack of object separation: the distance is the weighted mean distance of two objects because:

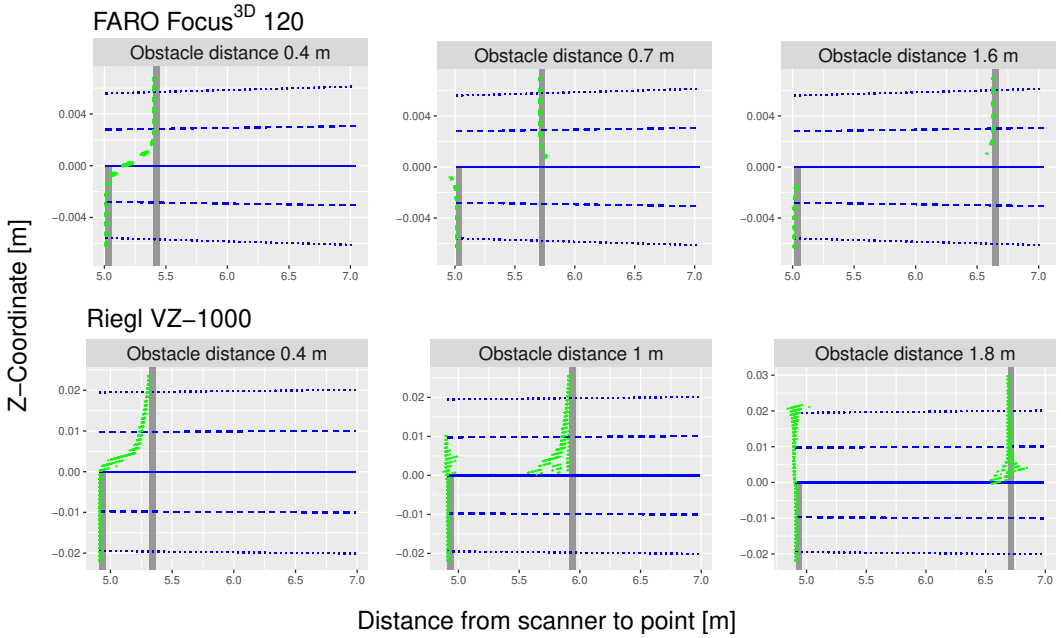

Figure 3.2: Side view of point clouds from Riegl VZ-1000 (bottom row) and FARO Focus^{3D} 120 (top row) scanners when the laser beam cones of the scanners intersect with two obstacles. The green dots indicate the triggered echoes (scan points). The solid blue line indicates the center of the viewline from the scanner over the edge, and the dashed (dotted) blue lines indicate twice (four times) the standard deviation of the Gaussian-shaped laser beam footprint. Vertical grey bars indicate the positions of the obstacles.

iiA the objects are too close to each other for separation; or

iiB the objects obtain a nearly identical amount of laser energy and are set wide apart

iii Distance deviation through ambiguity in distance measurement

iv No signal triggering (filtering)

i) When the laser beam cone intersects with only a single object, no specific triggering model is needed, because the distance to the point in the point cloud is the unambiguous distance measured by the laser.

iiA) When the laser beam intersects with two obstacles that are close to each other (0.5 m or less), the scanner does not identify them as separate objects. The distance delivered by the scanner appears to be a weighted mean distance. To derive the model of the distance measurement, we included all points that originated from laser pulses hitting the two obstacles in the lab experiments with at least 2% of the laser energy. Only the lab experiments where the obstacle distance was between 0 and 0.5 m were selected. For case iiA), we assumed a weighted distance to the two obstacles, as displayed in Equation 3.4.

$$D_p = \frac{D_{(1)}e^{\alpha E_{(1)}} + D_{(2)}e^{\alpha E_{(2)}}}{e^{\alpha E_{(1)}} + e^{\alpha E_{(2)}}} \tag{3.4}$$

where D_p is the distance between the scanner and the point, $D_{(1)}$ and $D_{(2)}$ are the distances from the scanner to the two obstacles, $E_{(1)}$ and $E_{(2)}$ are the ratios of the energy on the respective obstacles, and α = 4.37 is the parameter which resulted from the non-linear least squares fit of the model.

iiB) Another effect of a lack of object separation occurs when the laser energy on the two obstacles is nearly identical and the obstacle distance is at least 1.8 m. We assumed a weighted mean distance, where the respective laser energies on the two obstacles E_{l_o} serve as the weights:

$$D_p = \frac{D_{o1} * E_{l_{o1}} + D_{o2} * E_{l_{o2}}}{E_{l_{o1}} + E_{l_{o2}}} \tag{3.5}$$

iii) The other case of distance deviation seems to be dependent on the obstacle distance. The distance deviation oscillates around the edge towards the scanner and away from it. To fit a model, we selected points from around the edge of obstacle 1 of the lab setups with object distances greater than 0.5 m. We assumed, based on effects observed in lab experiments, that the distance deviation depends on a sinusoidal weighted obstacle distance and on the energy ratio of the laser beam on the obstacle. Hence, we set up the model for the distance deviation ΔD as follows:

$$\Delta D = -1 * \frac{sin(\frac{D_o - 0.5}{\alpha} 2\pi)}{\beta} * e^{\frac{\gamma}{E_l}} \tag{3.6}$$

where D_o is the obstacle distance (Figure 3.1) and E_l is the energy ratio of the laser pulse on the obstacle. α gives a weight to the obstacle distance, whereas β weights the sinusoidal effect and γ weights the energy ratio of the laser beam. The latter leads to the effect that the stronger the laser beam hits the object, the smaller the distance deviation becomes. The non-linear least squares model fit ended up with α = 1.324, β = 65180 and γ = 5.792.

iv) The last effect we observed in our data (Figure 3.4) is that in certain cases the FARO scanner does not trigger signals at all, hence prefiltering mixed pixel points with too much ambiguity. This is the case when obstacles are at least 0.6 m apart (meaning they are identified as separate objects) and the laser energy on both objects is of similar intensity. We assume prefiltering when the energy on the two objects is within the range of 50% $\pm$ 20%, based on the observations of the lab data.

3.2.2c.3 Riegl VZ-1000 The Riegl VZ-1000 scanner has more complex noise patterns than the FARO and the Leica scanner. This could be due to its ability to trigger multiple echoes from one laser pulse. To describe the noise patterns mathematically, we need to know the exact beam diameter of the Riegl scanner. However, for the Riegl VZ-1000, there is no such specification, neither in its technical specification

sheets nor in its manual (Riegl, 2015). The point cloud, however, shows that the scanner produces noise up to 21 mm above the edge of obstacle 1 (Figure 3.2). We assumed a beam diameter at exit of 18 mm ($1/e^2$), as officially specified for the Riegl VZ-4000. In the point cloud of the Riegl VZ-1000 scanner, we observed the following signal triggering functionalities (see Figure 3.2):

i Common distance measurement: a single object lies in the laser beam cone

ii Common distance measurement of a laser pulse hitting two objects: the laser energy on the first object is above 50%

iii Multiple signal triggering

iv Distance deviation through lack of object separation

v Distance deviation when separate objects are identified with specific patterns for:

vA obstacle 1

vB obstacle 2

i) When the laser beam cone intersects with only a single object, no specific triggering model is needed, and the distance of the point in the point cloud is the unambiguous distance measured by the laser.
ii) As Figures 3.4 and 3.2 reveal, the Riegl scanner triggers the points on the surface of obstacle 1 if the laser energy reaching it is at least 50% (assuming an equal reflection). Besides this threshold, no specific model needs to be developed.
iii) When the laser beam intersects with the two obstacles, and with obstacle 1 with less than 50% of the laser energy, the probability of triggering two points per laser beam appears to be 100% when the obstacles are at least 1.5 m apart. However, if between 0.7 and 1.5 m apart, the probability of triggering two points rises from 0 to 100%, but still only when the laser beam energy on obstacle 1 is less than 50%. The model for the probability of triggering an additional point for obstacle 1, hit with less than 50% of the energy and an obstacle distance of 0.7 m and 1.5 m is the following, with $\alpha = 0.51$ and $\beta = 2.7$ (non-linear least squares fit):

$$P_t = 1 + \alpha \frac{E_{(1)} - 0.5}{D_{(2)} - D_{(1)}} e^{\frac{1}{(D_{(2)} - D_{(1)})^{\beta}}} \tag{3.7}$$

iv) When the obstacles are closer to each other than 0.7 m, and in cases where there is no multiple triggering up to an obstacle distance of 1.5 m, the Riegl scanner does not appear to distinguish between separate objects and calculates a weighted mean, similar to the FARO scanner. To capture the effect of the “mean distance”, we fitted a non-linear least squares model only for the lab data where obstacles were 0.7 m or less apart, as the separation of single and multiple triggered signals between obstacle distances of 0.8 and 1.6 m is difficult, whereas the model presumably remains the

same. The resulting model is similar to the model in Equation 3.4 of FARO, with α = 4.1:

$$D_p = \frac{D_{(1)}e^{E_{(1)}} + D_{(2)}e^{\alpha(E_{(2)}-0.5)}}{e^{E_{(1)}} + e^{\alpha(E_{(2)}-0.5)}} \tag{3.8}$$

v) Once Riegl identifies separate objects, it reveals various patterns of distance deviation (noise pattern) on the two obstacles. To clarify these structures, we separated them for the two obstacles.
vA) If a laser pulse hits obstacle 1 with less than 50% of the energy and a signal is triggered (see model iii), the points show a specific noise pattern (Figure 3.2). Besides a distance deviation, there is a deviation perpendicular to the laser beam based on the fact that the center of the laser beam is no longer on the object.
We derived an unbiased Gaussian-distributed distance deviation, with a standard deviation of 0.02 m if the obstacles are between 0.7 and 1.1 m apart. If the obstacles are farther apart, the distance deviation from obstacle 1 (ΔD) has the following shape (α = 27.8, β = 0.012 and γ = -0.50):

$$\Delta D = \frac{\beta}{1 + e^{\alpha(-E_{(1)}+\gamma)}} - \beta \tag{3.9}$$

with a model for the distance uncertainty (standard deviation) $\sigma_{\Delta D}$:

$$\sigma_{\Delta D} = \gamma + \frac{1}{\alpha E_{(1)}^{\beta}} \tag{3.10}$$

where α = 1394, β = 0.72 and γ = 0.0022.

vB) Due to the fact described in (ii), only points with laser energy ranging from 50% to 100% on obstacle 2 are triggered for obstacle 2. The distance deviation from obstacle 2 for obstacle distances between 1.1 and 1.8 m is split into two parts: one distance deviation towards the scanner and one away from it. The distance deviation for obstacle distances between 0.7 and 1.1 m is not modeled separately because of difficulties in separating it from the points modeled under (iv). The distance deviation was fitted with a non-linear least squares approach for the following equation:

$$\Delta D = \alpha(1 - e^{-\beta E_{(2)}}) - \alpha \tag{3.11}$$

The noise part towards the scanner obtained α = 1.3 and β = 4.7, and the noise part away from the scanner obtained α = -0.46 and β = 2.4. The corresponding uncertainty for the distance deviation towards the scanner was fitted with the following model, with the result that δ = 0.0089 and γ = 2.9:

$$\sigma_{\Delta D} = \delta \frac{1}{E_{(2)}^{\gamma}} \tag{3.12}$$

The uncertainty for the distance deviation away from the scanner resulted in $\alpha = 0.00051$, $\beta = 0.0099$ and $\gamma = 13.2$ for the model:

$$\sigma_{\Delta D} = \beta + \alpha \frac{1}{E_{(2)}^{\gamma}} \tag{3.13}$$

Beyond an obstacle distance of 1.8 m, we observed a constant distance noise depending on the energy on obstacle 2, as in Equation 3.12, with $\alpha = 0.01$ and $\gamma = 2.4$.

3.2.3 Simulation study: laser scanning for forest inventories

3.2.3a Stand models based on Swiss National Forest Inventory (NFI) data

Swiss NFI data is collected on a systematic grid covering the entire country. This makes it possible to make a statistical inference regarding population values, such as wood volume, for the area of interest, e.g., for a whole country (Mandallaz, 2006). Since 2009 field measurements for the Swiss NFI have been conducted on nine systematic sub-grids of equal size. This enables representative evaluations of either single or combined grids.
As in an earlier study (Abegg *et al.*, 2017), we used information about the measured trees with heights of at least 1.3 m to derive stand-describing parameters in the form of a Weibull distribution. The variability of the derived stand descriptions covers all the possible stand parameters that are likely to occur in Swiss forests and includes some extreme values as well.

3.2.3b Stand models for simulation

We implemented the stand models in the same manner as in one of our previous studies (Abegg *et al.*, 2017), using Blender and the stand parameters to set up cylinders as a proxy for tree stems, with a position and a diameter, for a horizontal scan. Mixed signal effects are based on laser beams hitting multiple objects and the goal is to have the same for cylinders at the edge of the sample plot. We therefore at least doubled the edge length of our square sample plots compared to the size of the plot we used for the evaluation. Because the time needed for the definition of new cylinders increases exponentially, we limited the number of cylinders in a scene to 4,000, unlike in Abegg *et al.* (2017). However, in order to simulate dense stands as well, we applied simulations to two different rectangular plot sizes, with edge lengths of 23 and 100 m, to evaluate plots with edge lengths of 10 m for plots with tree densities above 4,000 trees per hectare and with 50 m edge lengths for plots with tree densities below 4,000 per hectare.

3.2.3c Signal triggering models

The goal of the simulation study is to simulate the most important effects when laser beam cones of terrestrial laser scanning (TLS) systems intersect with multiple objects. In this subsection, we describe the approaches used to simulate TLS systems based on our lab observations. As mentioned in section 3.2.1, we sampled the footprint of a circular-shaped virtual laser pulse based on a Gaussian-shaped density across the beam energy distribution. In Blender, one can set the angular resolution in longitudinal or latitudinal directions. In our study, we set both angular resolutions to $0.04°$. The sampling rate for one laser pulse was set to 300 sampled distances. The sampling rate has an influence on the sensitivity of the simulated laser scan at the fringes of the laser footprint. For our simulation study, we implemented different kinds of models derived from the lab tests, but also some theoretical approaches as a "baseline" for comparison purposes. All the models have in common that they deliver a distance from the scanner. Knowing the longitudinal and the latitudinal direction of the laser beam center, the combination with the distance to the scanner makes it possible to calculate a point in the point cloud.
The first step in the simulation of signal triggering was to identify possible objects for each laser pulse based on the range measurements of the samples (n = 300) within respective laser beam cones. For this purpose, we counted the number of range measurements within a 0.2 m window, moved in 1 mm steps from the minimal measured distance within the laser pulse to the maximal measured distance. Within this array of 1 mm steps, we identified the local maxima. These local maxima, their locations and the number of samples assigned to them provide a rudiment of objects, their ranges and the amount of laser pulse energy hitting them. In this study, these rudiments of objects are named "proto-objects". The amount of laser energy hitting a proto-object (referred to as E_I) is the ratio of the number of range samples closest to the respective proto-object (local maximum) to the total number of distance measurements sampled within one laser pulse.

3.2.3c.1 Geometric scanning "Geometric scanning" is a theoretical approach which stands for a scanner with an infinitesimally small laser beam diameter. In the simulation this means that one only samples the main direction of the virtual laser beam with one sample. This distance measurement is not subject to any distance deviation or other noise effect. It serves as a "baseline" to compare the performance of the other scanning approaches.

3.2.3c.2 Mean distance The "mean distance" scanner is a theoretical approach as well. It represents a very primitive (nonexistent) LiDAR scanner which simply produces a mean distance to the obstacles that are hit by a laser pulse. It serves as a

"worst case scenario" comparison with the other approaches.

3.2.3c.3 L-system: A Leica-like LiDAR simulation The lab experiments of the Leica BLK360 scanner reveal only prefiltering as an effect of laser pulses hitting multiple objects. Prefiltering of points produced by a laser scanner is always based on ambiguous backscattered signals from a LiDAR distance measurement. Ambiguous signals reduce the probability of triggering a signal. We implemented a prefiltering model, i.e., a model for triggering probability based on the lab data from the Leica BLK360 scanner (see section 3.2.2c). In the simulation, the prefiltering model first derives the proto-objects for each laser pulse. If there is only one proto-object within one laser pulse, the distance to that object is taken directly. If multiple proto-objects are in the way of a laser beam, the model checks the triggering probability for the proto-object which obtained the most energy from the laser pulse, according to the triggering probability function in Equation 3.3. The input parameters for the model are the energy ratios of the laser pulse on this proto-object (E_I) and the distance to the closest neighbouring proto-object D_o. However, we limited the values of D_o to a minimum of 1 m and a maximum of 8 m to produce plausible probabilities with the trigger probability function.

3.2.3c.4 F-system: A FARO-like LiDAR simulation We implemented the observed scanner properties in the following manner in order to handle multiple objects in the direction of the laser beam (Figure 3.3). The bases for applying the models are the "proto-objects", with their corresponding distance and energy ratios of the laser pulse reflected by each object. According to our observations, the FARO scanner does not separate objects within one laser pulse that are less than 0.55 m apart but treats them as one (the threshold lies between 0.5 and 0.6 m, according to the laboratory tests, see Figure 3.2 left panels). Therefore, we grouped the proto-objects together if they were less than 0.55 m apart and called them "identifiable-objects". Within these groups, we summed the reflected laser energy and calculated the mean distance to the proto-objects within the groups. We observed that the FARO scanner only triggers one signal per range measurement. Because this happens on the object which reflects the most energy, we selected the identifiable-object with the most laser energy. In cases where multiple objects had the same amount of energy, we selected the one closest to the scanner. Additionally, we selected the identifiable-object with the second most energy reflection. As the last preparatory action, we calculate the average energy of all the identifiable-objects. Based on this information, we implemented the following triggering models (see section 3.2.2c):

i) If there is only one proto-object in the laser beam cone for the range measurement, this distance is taken.

iiA) If the identifiable-object with the most energy is composed of multiple proto-objects, the weighted mean distance of the proto-objects according to Equation 3.14 is calculated (α = 4.37). This distance might be subject to prefiltering.

$$D_p = \frac{\sum_{i=1}^{n} D_{(i)} e^{\alpha(E_{(i)}-0.5)}}{\sum_{i=1}^{n} e^{\alpha(E_{(i)}-0.5)}} \tag{3.14}$$

where D_p is the distance between the scanner and the point, $D_{(i)}$ are the distances from the scanner to the n proto-objects, and $E_{(i)}$ are the ratios of the laser energy on the respective proto-objects.

iiB) If all identifiable-objects are farther from each other than 1.8 m and reflect a laser beam energy that is within $\pm$ 5% of the average energy on all identifiable-objects, a simple mean distance, weighted by the respective energies of the identifiable-objects, is calculated according to Equation 3.5.

iii) If the identifiable-object with the most energy contains only one proto-object, but the laser beam cone intersects with multiple identifiable-objects, the distance measurement is subject to a distance deviation according to the model described in Equation 3.6. As the distance between the obstacles (D_o), the distance between the two identifiable-objects with the most energy is taken. The laser pulse energy can also be distributed across more than two objects, the model input of laser energy was therefore adjusted so that the possible range of energy on the identifiable-object is 70% to 100%, which are the energy values the model is fitted on. The slight intercept of this model when 100% of the energy is reached is removed from the distance deviation. Additionally, the amount of energy (E_l) is set to a minimum of 70% so that the derived model produces plausible values. These signals are subject to prefiltering as well.

iv) Prefiltering: If the energy of the identifiable-object with the most energy is less than the average energy of all identifiable-objects plus 20%, no signal is triggered. The idea behind this approach is, with reference to observations in the lab experiments, that if the energies on the objects are too close to each other, the scanner omits the echo. Thus, we assume that if the identifiable-object with the most energy is too close to the average energy, ambiguity has been reached for the scanner.

3.2.3c.5 R-system: A Riegl-like LiDAR simulation Figure 3.3 illustrates the implemented signal triggering for the Riegl like system. Similar to with the FARO scanner, there is a minimal distance at which the Riegl device does not appear to distinguish between two objects. In the lab experiments, this threshold is very clearly visible up to an obstacle distance between 0.7 and 0.8 m. Therefore, we grouped proto-objects that were closer to each other than 0.75 m into “identifiable-objects” and calculated their mean distance to the scanner and the energy ratio of the laser beam hitting the proto-objects within each identifiable-object. However, also beyond this distance up to 1.5 m, depending on whether the scanner performs multiple

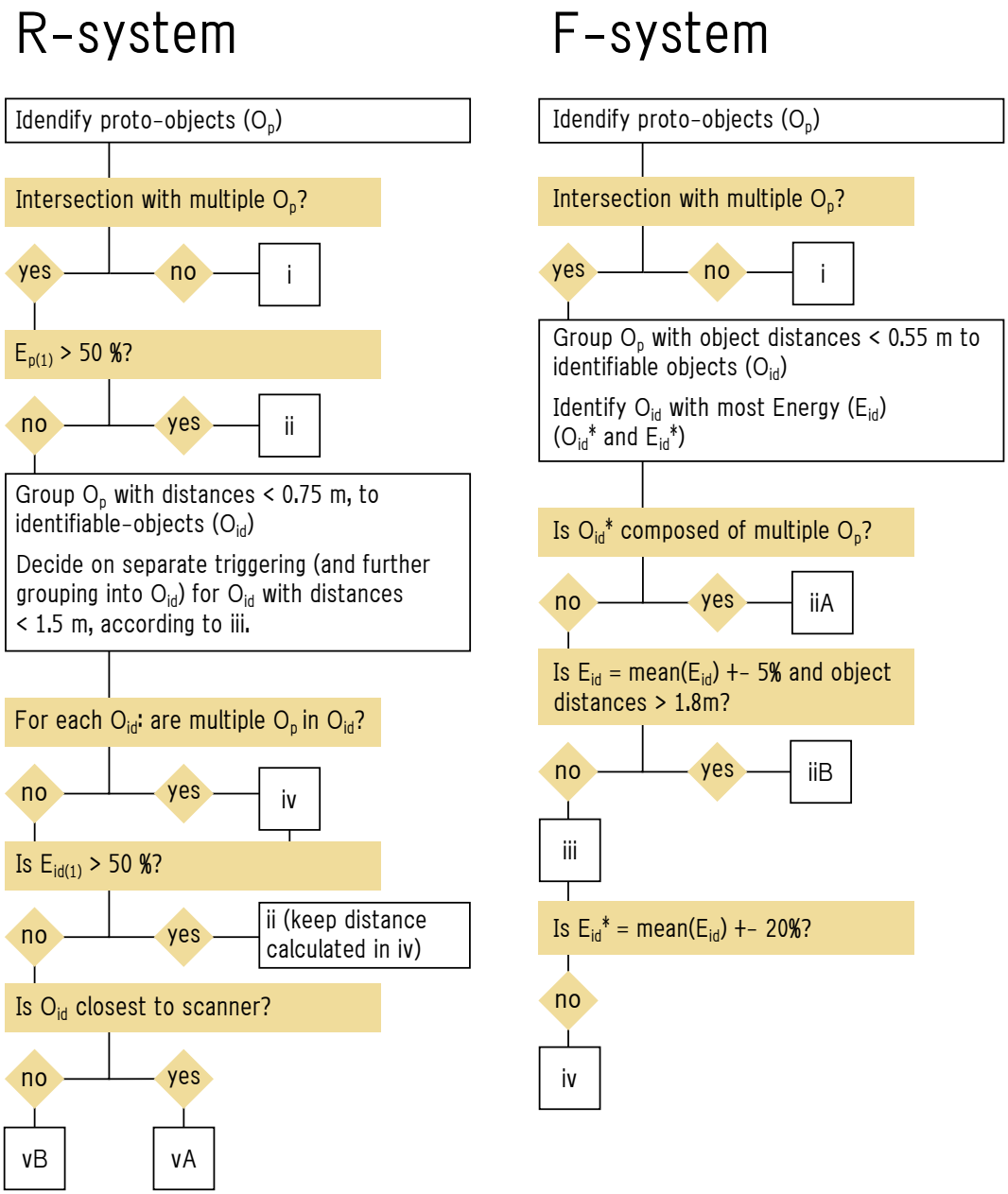

Figure 3.3: Decision tree on signal triggering of R- and F-system. O_p are the proto-objects, E_p is the according energy ratio on each proto-object. O_{id} are the identifiable-objects, whereas one O_{id} can be composed of either one or several O_p. E_{id} is the cumulative energy ratio on all O_p within each O_{id}. Procedures for i, ii, iii, iv, and vA, vB for the R-system and iiA, iiB for the F-system, are described in the text.

triggering, the Riegl scanner does not appear to distinguish between these obstacles, with decreasing probability. For multiple signal triggering, we checked whether the identifiable-objects are closer to each other than 1.5 m. In the lab experiments (Figure 3.4), the Riegl scanner always triggers multiple signals when obstacle distances are beyond this value. When they are smaller, it triggers with increasing probability. We implemented the following signal triggering models for the R-system (see section 3.2.2c):

i) If the laser pulse for the range measurement hits only one object, the range measurement to that object is used to directly calculate the coordinates of the point.

ii) In the lab experiments (Figures 3.4 and 3.2), the Riegl scanner triggers a point clearly on the first obstacle the laser beam hits, as long as the laser beam energy on this obstacle is above 50%. Consequently, we implemented the same logic for either the proto-objects or the identifiable-objects, with their specifically calculated distances (see iv).

iii) Multiple signal triggering is implemented as follows (considering ii). As Figure 3.4 indicates, the Riegl scanner always triggers a signal for each obstacle if they are farther from each other than 1.5 m. We implemented this rule for each "identifiable-object". However, when the obstacle distance is between 0.7 and 1.5 m, the probability of triggering signals for separate obstacles continually rises from 0 to 100%. The implementation of multiple signal triggering for groups of identifiable-objects when they are between 0.7 and 1.5 m apart, is as follows. The identifiable-object with the most energy is definitely triggered. The probability (p) of triggering a signal for the other obstacles (identifiable-objects) is:

$$p = 1 + \alpha * (E_{within} - 0.5) * \frac{1}{D_{meo}} * exp^{D_{meo}^{-\beta}} \tag{3.15}$$

where α = 0.51, β = 2.7 and E_{within} is the relative energy of the laser pulse on all identifiable-objects that are 0.7 m to 1.5 m apart and are intersected by one laser pulse. D_{meo} is the distance to the identifiable-object with the most energy. When p is below 0, it is set to 0.

iv) The lab experiments indicate that obstacles closer to each other than 0.75 m are not distinguished as separate objects. Also beyond that obstacle distance, up to 1.5 m, the scanner does not appear to always distinguish between separate objects, although with decreasing probability. This probability appears to be connected to the triggering of multiple signals with one laser pulse. Thus, if the scanner identifies separate objects, it triggers points for each obstacle; otherwise, it treats them as the same object. In that case, the scanner interprets multiple proto-objects as a single object and calculates a weighted mean distance. We implemented the calculation of the weighted mean distance to the obstacle D_p based on Equation 3.8 in the following way:

$$D_p = \frac{D_{(1)}e^{E_{(1)}} + \sum_{i=2}^{n} D_{(i)}e^{\alpha(E_{(i)}-0.5)}}{e^{E_{(1)}} + \sum_{i=2}^{n} e^{\alpha(E_{(i)}-0.5)}} \tag{3.16}$$

where $D_{(i)}$ are the distances from the scanner to the (1 to n) obstacles and $E_{(i)}$ is the amount of laser pulse energy on the (1 to n) obstacles, with α = 4.08.

vA) The obstacle closest to the scanner shows two patterns of distance deviation for points triggered from laser pulses intersecting the obstacle with less than 50% of the energy and hence with their center not on the obstacle itself. Depending on the distance to the next obstacle, this distance deviation gradually develops a

specific pattern (Figure 3.2). We split this gradual development into two specific patterns, one for obstacle distances below 1.15 m and one for obstacle distances beyond 1.15 m.
At obstacle distances below 1.15 m, we assumed a constant normally distributed distance deviation with a standard deviation of $\sigma = 0.02$ m. For obstacle distances beyond 1.15 m, a distance deviation is directly implemented with Equation 3.9 for the shape and with Equation 3.10 for the uncertainty.

vB) Figure 3.2 reveals different distance deviation patterns on obstacle 2. To be close to the output of the lab experiments, we implemented the distance deviation pattern as follows.
The case where obstacles cannot be distinguished is already treated under iv). Once multiple triggering takes place, a gradual change occurs in the pattern of obstacle distances from 0.7 m to 2 m, beyond which it appears to remain constant. We thus implemented the distance deviation pattern for the obstacles that are not hit first by the laser pulse with two models, one for obstacle distances below 2 m and another for obstacle distances above 2 m. For the distance deviation of identifiable-obstacles with a distance of less than 2 m to the next object, we split the range measurements into two equally sized groups, one deviating towards the scanner and the other away from the scanner. For the shape of these distance deviations, we used Equation 3.11 and the corresponding standard deviations in Equations 3.12 and 3.13 for a Gaussian-shaped distance uncertainty of the deviation towards the scanner and away from it. When the laser energy $E_{(l)}$ on one of the objects drops below 50%, it is set to 50%.
If an identifiable-object is at least 2 m away from the next object, Equation 3.12 is used again, with $\alpha = 0.01$ and $\gamma = 2.4$ for an unbiased distance noise dependent on the energy on the respective object.

3.2.3d Simulated laser scanner types and beam properties

We implemented the above-described LiDAR simulation approaches, except for the "geometric scanning", with beam diameter sizes at exit ($1/e^2$) of 3 mm, 18 mm and 50 mm, following the diameters described in Table 3.1. The idea was to have a small and a large TLS version and a diameter which represents a footprint of a drone-mounted LiDAR scanner. As a beam divergence, we implemented 0.3 mrad for all simulations.

3.2.3e Simulation control, data preparation and statistical analysis of simulation output

The simulations were implemented in Blender (Blender Online Community, 2015), as adapted by Gschwandtner *et al.* (2011) and described in this publication. We used Blender to simulate diameter distributions from one annual panel (representative grid) of the Swiss NFI, as described in Abegg *et al.* (2017). Each of these scenes

was virtually scanned with the above-mentioned scanner models with different beam diameters. This led to a total of 8890 2D point clouds. For the evaluation, we used the true position and the diameters of the cylinders in the scene to assign the points from the point cloud to the closest cylinder. In real TLS applications, point clouds are usually filtered in order to remove possible noise, e.g., from mixed pixel echoes, or points of unwanted objects, e.g., leaves in case woody volume is targeted. The filtering procedure depends to a large extent on the scanned objects, the evaluation routines and the goal of the scanner application. As a proxy for noise filtering, we implemented a simple filter procedure, removing all points farther than 2 cm and 10% of the cylinder diameter from its surface. This filtering approach is not applicable in real scanning situations, as it needs a priori knowledge on the objects, but was used here to illustrate possible filtering effects, as well as the influence of noise points with large distance deviations. All statistical analyses were performed in R (Version 3.4.4) (R Core Team, 2017).

3.3 Results

3.3.1 Analysis of edge noise effects of three terrestrial laser scanners

Edge noise effects of three terrestrial laser scanners (Leica BLK360, FARO Focus^{3D} 120 and Riegl VZ-1000) were analyzed using the experimental setup as shown in Figure 3.1. The distances between the obstacles intersected by one laser pulse play a major role in how these devices trigger one or multiple points, as our observations of their point clouds indicate. The distance between obstacles, as used in our experiments, had to be adapted for each individual device, because every device triggers points in a unique way. To simplify the experimental approach and modeling, we only used two obstacles.

3.3.1a Prefiltering

One aspect of the triggering functionality is how the devices omit echoes (prefiltering). Figure 3.4 shows the number of echoes (points) triggered per laser pulse sent out by the laser scanner in a specific latitudinal direction (theta). The Leica scanner omits echoes from multiple obstacles that are close to each other, such that the energy of the laser pulse is similar on both objects. The closer the objects are, the stronger the prefiltering is. The FARO scanner also performs prefiltering when the energy on both obstacles is similar, but from an obstacle distance of around 0.5 m and greater. With increasing distance between the obstacles, prefiltering becomes slightly stronger. At an obstacle distance greater than 1.8 m, however, and only when the laser pulse energy on two objects is almost the same, the prefiltering intermits.

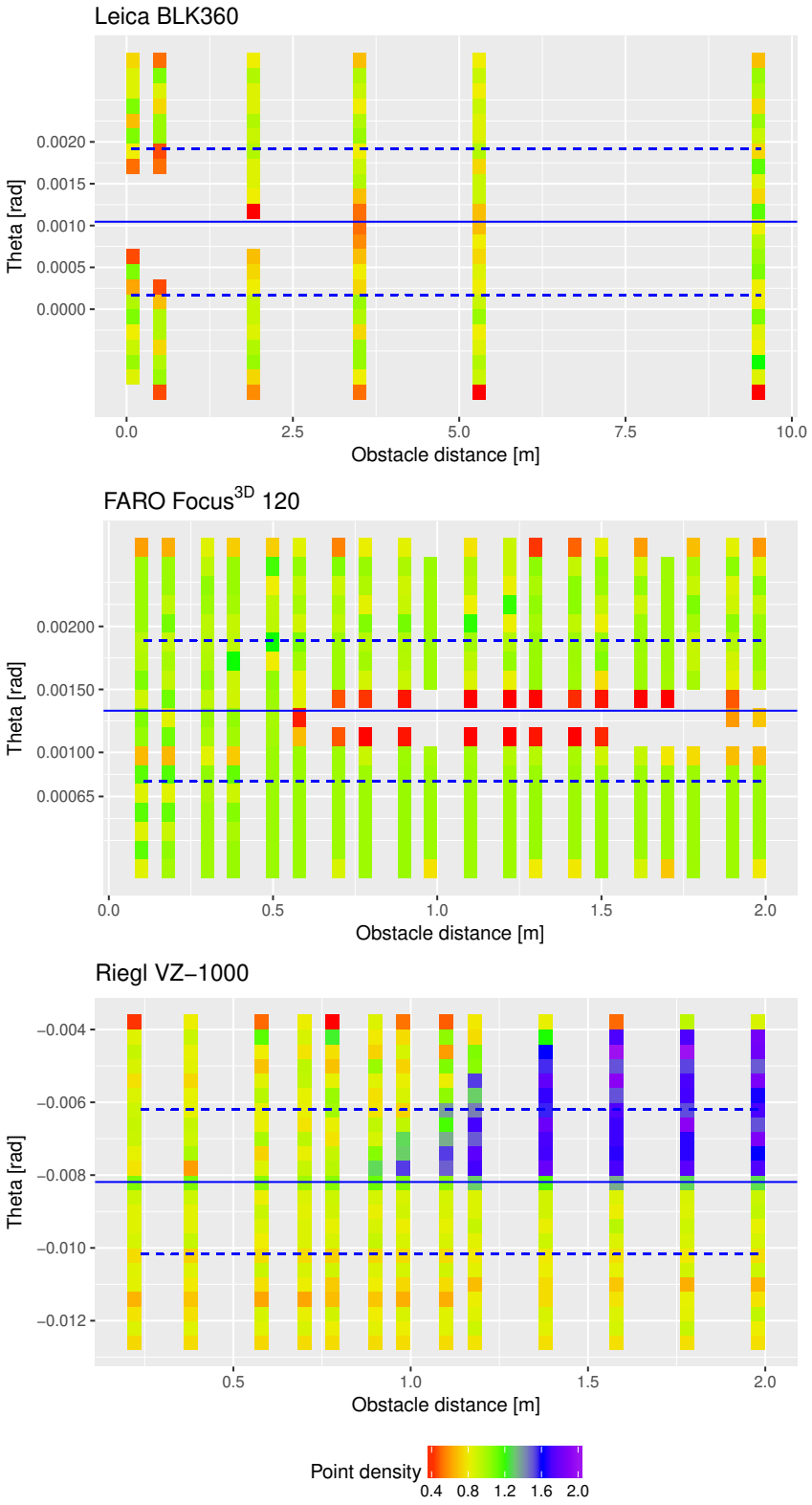

Figure 3.4: Prefiltering and multiple triggering from lab tests of three different scanners (top: Leica BLK360; middle FARO Focus^{3D} 120; bottom: Riegl VZ-1000): point densities per scanning angle (theta) from multiple experimental setups as a function of obstacle distances. The blue solid line shows the viewline of the scanner at the edge height of obstacle 1. The blue dashed line represents the footprint (using $1/e^2$) when the beam center is at the edge height of obstacle 1. Colors on the vertical bars indicate point densities.

3.3.1b Multiple triggering

Neither the FARO nor the Leica scanners trigger multiple points from one laser pulse. On the other hand, the Riegl scanner does no prefiltering at all, but supports multiple triggering. Multiple triggering is referred to here as the triggering of more than one point per laser pulse. Time-of-flight laser scanner systems have the ability to trigger multiple signals from one laser pulse (Kukko & Hyyppä, 2007; Maas & Vosselman, 2010). As Figure 3.4 indicates, the Riegl VZ-1000 triggers more than one point per laser pulse for specific obstacle setups. Up to 50% of the laser pulse energy on the first obstacle, respectively reflected by it, leads to clear triggering on the first obstacle. If the energy is less than 50% when the laser beam center has crossed the edge, and the obstacles are more than 0.7 m apart, the scanner begins to trigger echoes from both obstacles with increasing probability, reaching 1 when the obstacles are more than 1.5 m away from each other. Beyond this obstacle distance, two signals are always triggered when a laser beam intersects with two objects.

3.3.1c Distance deviation through lack of object separation

The placement of obstacles intersected by one laser pulse of a scanner influences not only prefiltering and multiple triggering, but also where a point is triggered. A user of laser scanners expects the points to represent points on the surface of scanned objects. However, depending on the surface a laser pulse hits, the time-dependent profile of the backscattered light (waveform) is altered (Mallet & Bretar, 2009). Based on this waveform, the scanner has to decide whether it has hit one or more objects with one laser pulse. With strong prefiltering, the Leica scanner removes most of the ambiguous distance measurements so that only signals that lie fully on the object surface are triggered (except for the common range noise). In very rare cases, as can be observed in Leica point clouds, this is not the case. However, as we can see in Figure 3.2, the FARO and the Riegl scanners do not distinguish between two objects if they are close to each other. When the obstacle distance is small, these scanners trigger the points at something similar to a weighted mean distance of the laser beam to the obstacles (Figure 3.2 left). With increasing distance between the objects, points are triggered at the distance of either one of the two objects (or both as in the case of multiple signal triggering). The distance threshold is up to 0.6 m for the Riegl scanner and 0.5 m for the FARO scanner. Beyond these obstacle distances, the scanners produce separated point clouds for the different obstacles. However, even with higher obstacle distances (e.g., 1.8 or 2 m), and when the laser beam center hits the edge of obstacle 1 exactly, the FARO scanner appears to have problems separating the two obstacles.

3.3.1d Distance deviation through mixed pixel effects

As we observed in the lab experiments, FARO Focus^{3D} 120 and Riegl VZ-1000 produce specific range deviations when the laser beam cone intersects more than one object and the scanner is able to distinguish between two objects (Figure 3.2). The FARO scanner triggers points on either object, starting at a distance between obstacles of 0.6 m. It produces a slight distance deviation of the triggered points, sometimes towards the scanner, sometimes away from it, in a sinusoidal manner depending on the distance between the obstacles.
The distance deviation of the Riegl scanner displays a more complex pattern. The Riegl device triggers points "exactly" at the surface of obstacle 1 when the laser pulse energy on it is greater than 50%. However, there are scan points above the edge of obstacle 1, owing to the ability to trigger multiple signals for one laser pulse (Figure 3.2). This begins to happen when the laser energy on the first obstacle is less than 50% and the obstacle distance is at least 0.8 m, with an increasing probability of triggering with increasing obstacle distance, reaching 100% when the obstacles are 1.4 m apart. Additionally, these points slightly deviate towards the scanner by a few centimeters. The points on obstacle 2 deviate in both directions depending on the laser pulse energy on this obstacle. The pattern of the noise on obstacle 2 changes for obstacle distances of up to 2 meters. Above that distance, the pattern remains constant (depending on the laser pulse energy ratio on obstacle 2).

3.3.2 Analysis of simulation study

3.3.2a Impact of laser beam diameter and object size on visibility

Our hypothesis (see section 3.1) was that beam diameter and signal triggering have an influence on the detection of objects. For forest inventories, it is crucial to know which object size is still detectable, as this makes it possible to set realistic objectives when applying close-range laser scanning. We defined "detectable" objects as those that have at least one laser point assigned (closer to their surface than to the surface of another object). We simulated laser scanning in a plane with different beam diameters and signal triggering approaches, where cylindrical objects following stand densities derived from 684 NFI sample plots were placed as detectable objects. To show the effect of filtering procedures on the point cloud, we removed points that were more than 10% of the cylinder diameter and at least 2 cm away from the cylinder surface.
Figure 3.5 shows the comparison regarding the mean detectability of different object sizes by laser beam diameter and signal triggering from 514 square sample plots with edge lengths of 50 m and tree densities below 4,000 trees per hectare. Each signal triggering approach is compared to a geometric scanning, which represents a laser scanner with an infinitesimally small laser beam. Such a theoretical scanner would deliver a point cloud without any noise or distance deviation from the objects.

We also implemented a system "mean distance", which calculates the mean distance weighted by the reflected energy to all the objects that are hit by a laser pulse. This system represents the opposite of the geometrical approach, and delivers a maximum amount of noise. The most important effect is that the smaller the beam diameter, the higher the detection rate of small objects, especially in dense plots (Figure S3.1). When only one point per laser pulse can be triggered, small objects up to at least 4 cm in diameter are clearly less frequently detected. The reason for this effect is that when multiple objects are hit by one pulse, the larger objects reflect more light, which favours their identification. In the case of scanning systems with prefiltering (L-system or F-system), this effect can lead to a further loss of points for small objects. On the other hand, systems with multiple triggering ability, as implemented in the R-system, show a clearly higher rate of object detection. If a scanner system were to use the "mean distance" approach, the detection rate without filtering would be at the same level as with multiple triggering (R-system) or even higher. Yet, as the detection rates after filtering in Figure 3.5 indicate, most of the objects are false detections. This implies that many of the points for small objects would not contribute to a reasonable reconstruction of a scanned object. The "visibility" of an object depends strongly on the object size, the distance to the scanner and the stand parameters (e.g., the density of objects). Thus, with shorter distances from the scanner, for example for squares with edges 10 m in length, more objects are detected, even with a higher "tree density". Especially small objects are less occluded when scanned with small laser beam diameters, as exemplified in Figure S3.1.

3.3.2b Impact of laser beam diameter and object size on the representation of scanned objects

The number of points by which an object is represented in a point cloud, and the precision of their location, are crucial for the assessment of using laser scanning. We, therefore, evaluated the number of points per object (cylinder) with and without filtering. The filtering is described in section 3.3.2a. "Invisible" objects, that is, objects with no points after filtering, were not considered in the evaluation. The filtering serves as an indicator of the quality of the precision of the points' locations. Figure 3.6 displays the variation in the number of points as boxplots. It only compares objects which have at least one triggered echo in each of the scanning approaches. The variation arises from the distance to the scanner and the stand parameters, especially the density of the objects (see also Abegg *et al.*, 2017). A regression analysis using the following formula demonstrates the importance of the influence of the objects' diameters, their distances from the scanner and the number of objects per scene:

$$\sqrt{n_p} = log(diam_o) + log(D_s) + \sqrt{n_t} + prop_L \tag{3.17}$$

where n_p is the number of points per object, $diam_o$ is the diameter of the objects (cylinders), D_s is the distance between the object and the scanner, and n_t is the

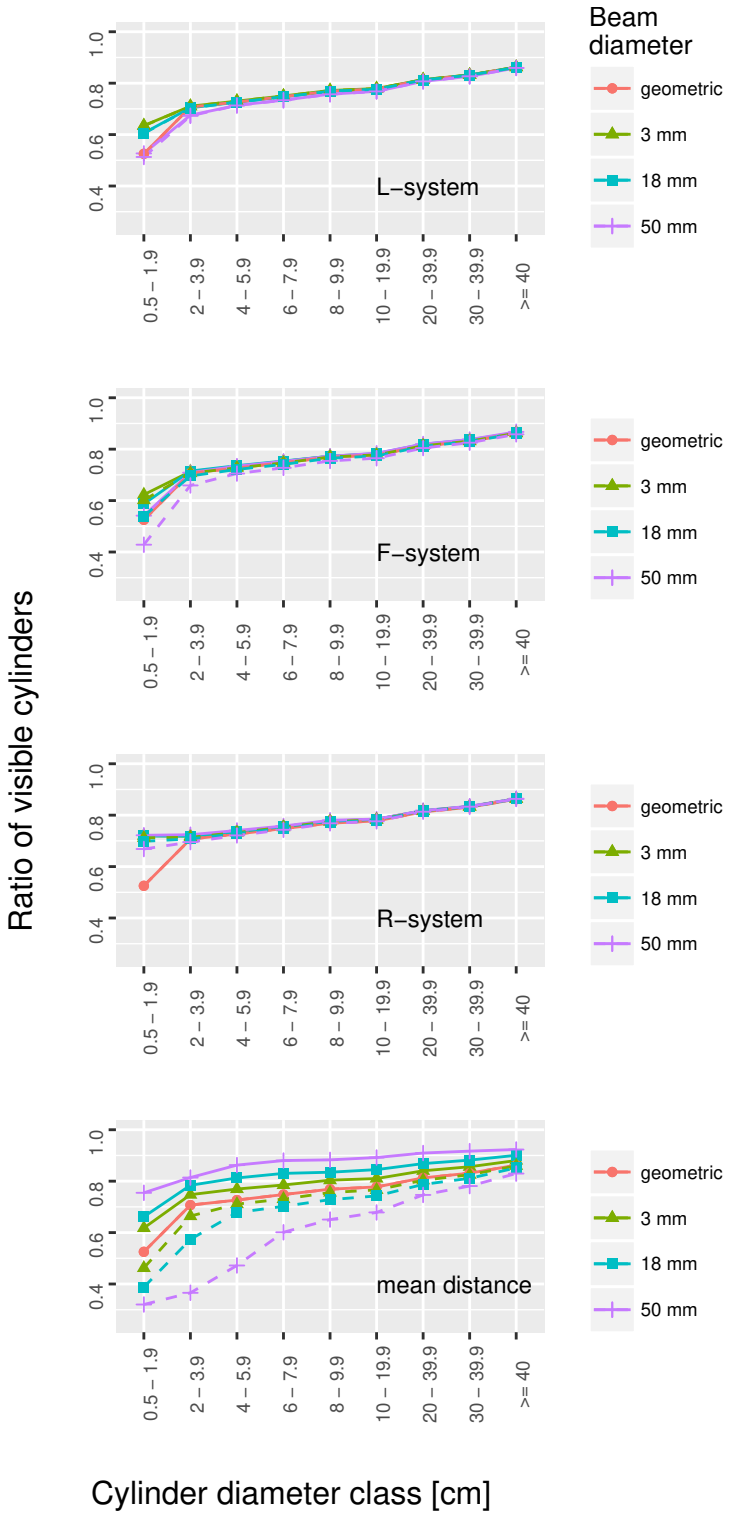

Figure 3.5: Ratio of the number of cylinders with at least one "hit" to the total number of cylinders on 514 square plots with an edge length of 50 m in forest stands with a tree density of less than 4,000 trees per hectare, by cylinder diameter class, signal triggering model and laser beam diameter at exit. Dashed line: number of visible cylinders after filtering the point cloud.

number of objects per scene and indicates the density of objects. As we have shown previously (Abegg *et al.*, 2017), n_t is the most important stand parameter that influences the visibility of a sample plot when performing laser scanning. To show

Table 3.3: Standardized model coefficients based on scaled variables to make their effect size comparable, for the diameter of the objects (cylinders) $diam_o$, the distance between the object and the scanner D_s and the number of objects (trees) n_t. Adjusted R^2 = 0.69.

Variable	Standardized model coefficient	*p* value
Intercept	0	0
$log(diam_o)$	0.59	0
$log(D_s)$	-0.58	0
$\sqrt{n_t}$	-0.16	0

the effect of these three influencing parameters, we removed the influence of the LiDAR property $prop_L$ (signal triggering system and beam diameter) by including it in the model.

In dense stands (see Figure S3.2), the L- and F-systems have fewer points per object with increasing laser beam diameter, especially on small objects. However, in stands with lower tree density, a larger laser beam diameter leads to more points per object. The R-system, which is capable of multiple signal triggering, displays a significant discrepancy between the unfiltered and the filtered point cloud for large footprints. In the point cloud without filtering, the number of points is far greater and wrongly suggests that a large footprint performs better than a small one. This indicates that point location precision is suboptimal. All plots in Figure 3.6 suggest that there are limits to object sizes that are reasonable to scan, depending on the scanning system, the beam diameter and the application. As can be seen in Figure S3.2 and also suggested by Table 3.3, scans from closer objects deliver a much greater number of points per object, even for smaller sizes.

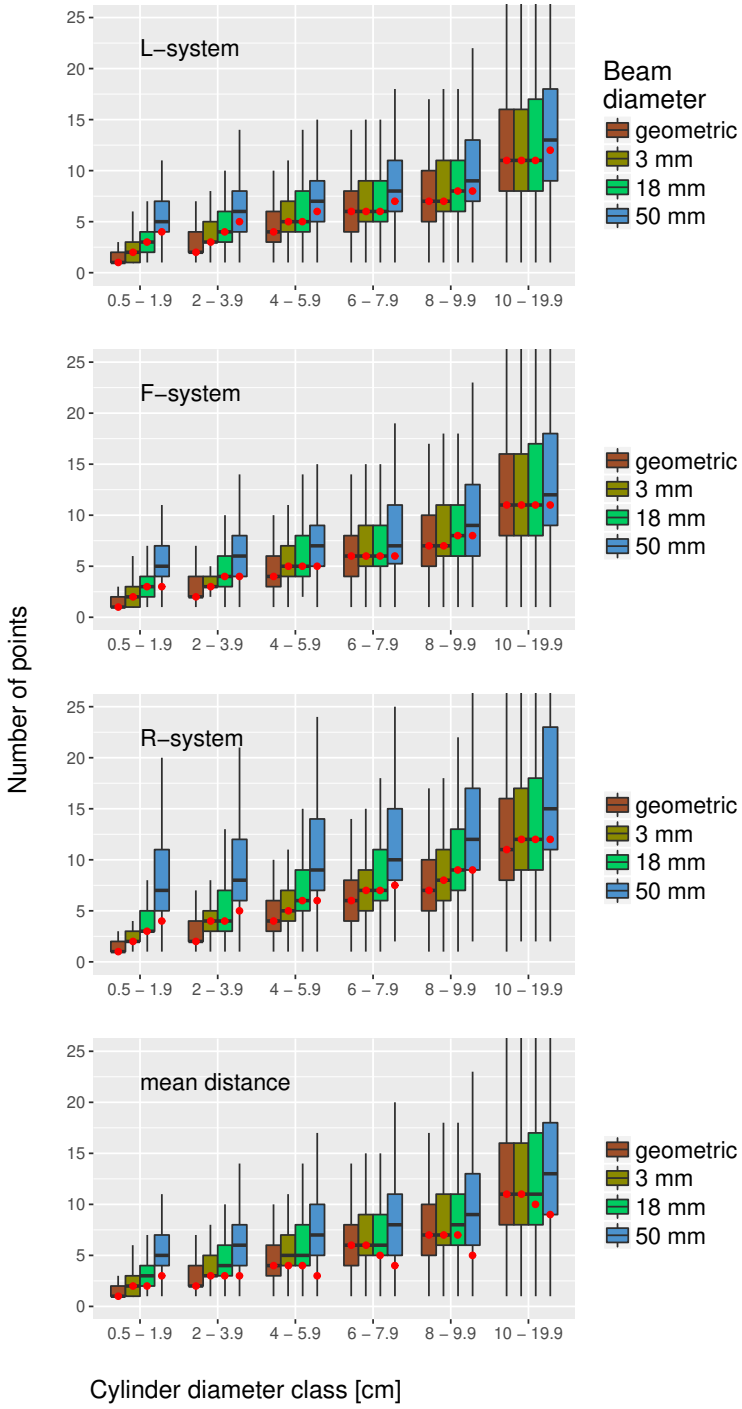

Figure 3.6: Number of points per cylinder in simulation experiments for 514 square sample plots of 50 x 50 m in forest stands with tree densities of less than 4,000 trees per hectare. Only cylinders that have at least one point in all the simulated scanning settings are evaluated. The box plots show the variation in the number of points per cylinder for different cylinder diameters, point triggering models and laser beam diameters at exit from the scanner. The red dots indicate the median of the number of points after filtering the point cloud (points must be closer than 10 percent of the cylinder diameter and, if not, closer than 2 cm). The point triggering model "geometric" simulates a laser scanner with an infinitesimally small laser beam.

3.4 Discussion

The objective of this simulation study was to investigate the effects of certain TLS properties, such as laser beam diameter and signal triggering, on point cloud quality when scanning in forested environments. For the implementation of a TLS simulation, we analyzed three state-of-the-art terrestrial laser scanners in terms of their effects when their laser beams intersect with multiple objects along their range. The findings from this study provide a basis for setting realistic objectives regarding the application of TLS for forest inventories.

The presented simulations make it possible to partially explain how the various scanning effects of the three devices influence the resulting point cloud. These effects are the prefiltering of points based on ambiguous echoes, the distance deviation patterns at edges of objects, the lack of separation of objects, and the triggering of multiple points per range measurement. The simulation study reveals the extent to which laser beam diameter and signal triggering approaches influence point cloud quality. The main implications are that objects with "small" diameters can hardly be depicted by TLS in a reasonable way because they are not visible in the point cloud, are represented by very few echoes and/or are subject to severe measurement errors due to ambiguous echoes (edge effects). The actual threshold for "small" depends on the objective of the TLS application and the point cloud evaluation algorithms applied.

The lab experiments demonstrate two effects of deviation of scan points from an object's surface, one perpendicular to and the other parallel to the laser beam. The perpendicular deviation is an effect of multiple signal triggering, which produces points along the central axis of the laser beam. Thus, if a beam touches an object at its edge, the point's possible distance to the object is directly dependent on the diameter of the laser. Concerning the distance deviation parallel to the laser beam, the phase-shift system (FARO) performs differently compared with time-of-flight systems (Riegl and Leica). The phase-shift system struggles with ambiguity problems, due to the combination of intensity modulations in the laser beam to measure a range. Therefore, depending on the distance of the scanned obstacles to each other, it can either remove points that are clearly problematic (prefiltering) or display a distance deviation which is sinusoidally weighted by the distance between the obstacles. In certain cases, ambiguities cannot be resolved and produce severe distance deviations (range averaging as described in Newnham *et al.*, 2012). Time-of-flight systems do not struggle with this kind of problem, owing to their ability to evaluate the whole reflected laser energy pattern over time. The Riegl and FARO scanners do not separate obstacles that are close to each other, while the Leica scanner solves the problem by prefiltering these points. For a scanning device, there is no way to perfectly resolve all types of objects of any shape, as one object with an inclined surface may reflect the same light pattern as two separate objects. There are only

two available options, to either prefilter or provide some kind of average distance to the objects (range averaging, see Newnham *et al.*, 2012).

The simulation study shows the limitations of depicting small objects precisely in a point cloud. Either they are not visible or they have only very few points because of their small size. Especially when a scanner prefilters the point cloud, almost no points are left on small objects. Triggering multiple signals alleviates this effect, whereas the points are at a certain distance from the object surface, which can lead to erroneous object reconstructions. Another observed effect is that objects appear flattened in the point cloud with increasing beam diameters. This effect is due to the laser beam working like a moving window, averaging the ranges measured within its footprint.

The signal triggering of laser scanning systems is influenced by many factors, such as the object shape, its surface, the reflectance of the object, the constellation of multiple objects, and even the atmospheric conditions. In addition, the scanner settings (adjustable or not) have an influence on the point cloud. However, reverse-engineering of signal-triggering functionalities, without any detailed manufacturer's information on the devices, is a huge effort. Nevertheless, we were able to cover the most important effects observed in point clouds.

The effects observed with the two-obstacle lab setting had to be generalised for cases where a laser pulse hits more than two objects. Hence, the effects caused by such settings most likely do not match reality exactly. Prefiltering effects are assumed to be reproduced in a realistic way, and surely provide realistic implications. The primary objective of the simulation study was not to reproduce exactly the same scanning results of the three devices investigated, but to allow general conclusions to be made regarding the effects of different signal triggering approaches. Nevertheless, the effect of the laser beam size is based on realistic assumptions, as the effect of its size is precisely reproducible.

There are various effects that could additionally be considered with the simulation approach used in this study, such as the intensity of the reflected light, multiple reflectance of the photons of the laser pulse, the influence of incidence angles on the objectives, and errors in the range measurement of the different devices.

An important finding of the present study for forest inventory applications is that small objects lack appropriate representation in point clouds of the signal triggering approaches investigated here, in that points are either prefiltered or subject to a deviation from the object's surface. Information on small objects deteriorates even more with increasing distance to the scanner, especially in environments with a high density of objects, due to occlusion and an increasing probability of mixed pixel situations. This implies that scanning small branches (e.g., less than 2 cm in diameter) in tree crowns (large distance to the scanner) with many small branches (high density) will be nearly impossible when tree crown reconstruction is the objective of the application. In such a situation, scanners with small laser beam diameters perform slightly better. On the other hand, larger laser beam diameters, in combination with multiple triggering, deliver more points per object. Larger

branch diameters (e.g., up to 6 cm) are also difficult to represent, depending on the application. Another problem occurring with large laser beam diameters is that the object shape tends to be flattened. This could lead to a bias in diameter estimation, e.g., when applying the widely used Hough transform approach (e.g., Simonse *et al.*, 2003; Hough, 1962; Bienert *et al.*, 2007; Heinzel & Huber, 2017) to fit circles or cylinders in the point cloud.

These findings indicate that TLS-based wood volume estimations of smaller trees might be severely impacted, as well as estimations of small branches. Depending on the triggering approach, small branches are either underestimated, because of prefiltering and occlusion, or overestimated, through the distance deviation of points. Scanning in dense forests, e.g., those with understorey, will increase occlusion effects considerably (Abegg *et al.*, 2017), further reducing the number of visible objects. Additionally, we expect additional noise in the point clouds due to an increment in mixed pixel effects caused by laser pulses intersecting with multiple small branches. Similar effects are to be expected when scanning during the growing season (leaf-on conditions), when additional problems of separating echoes from leaves and woody parts would arise. In addition to these technical limitations, even slight wind or precipitation would add further noise to the point cloud. Nevertheless, we expect TLS based wood volume estimations of large trees or large branches are mostly accurate since the ratio of erroneous points is decreasing with increasing object size. Therefore, if diameter thresholds are chosen approprately, TLS is still the most promising approach for tree volume estimation. Yet, future simulation experiments, including volume estimation approaches, need to be conducted, to examine details of volume estimation.

3.5 Conclusions

In this study, we investigated edge noise effects of three terrestrial laser scanners. We used their scanning properties to evaluate the influence of signal triggering approaches, laser beam diameters and stand properties on the quality of the point cloud. We show that these devices handle ambiguous signals from a controlled experiment, with obstacles placed in the laser beam, with different approaches: prefiltering, multiple signal triggering and deviation of points from object surfaces. All approaches have disadvantages, either leading to a lack of information or biased information. In a simulation study with 684 stand diameter distributions, we show that especially small objects (twigs and small branches) in combination with large (or strongly diverging) laser beams produce lower point cloud quality. These effects are increased when objects are farther away from the scanner and/or the density of objects is high, for example in tree crowns. We therefore recommend the choice of a targeted branch diameter to be measured of at least 2 cm, whereas a reasonable diameter would be the one for “merchantable” wood ($\geq$ 7 cm) which is widely used

in NFI reporting. Furthermore, we recommend using terrestrial laser scanners with a small footprint if object reconstruction is intended. If the gap probability of a stand needs to be assessed, a device with multiple signal triggering will provide more information with a similar angular resolution than devices with single signal triggering. These findings contribute to the ability to set realistic objectives when applying terrestrial laser scanning for forest inventories and support the selection of suitable scanners.

3.6 Supplementary Material

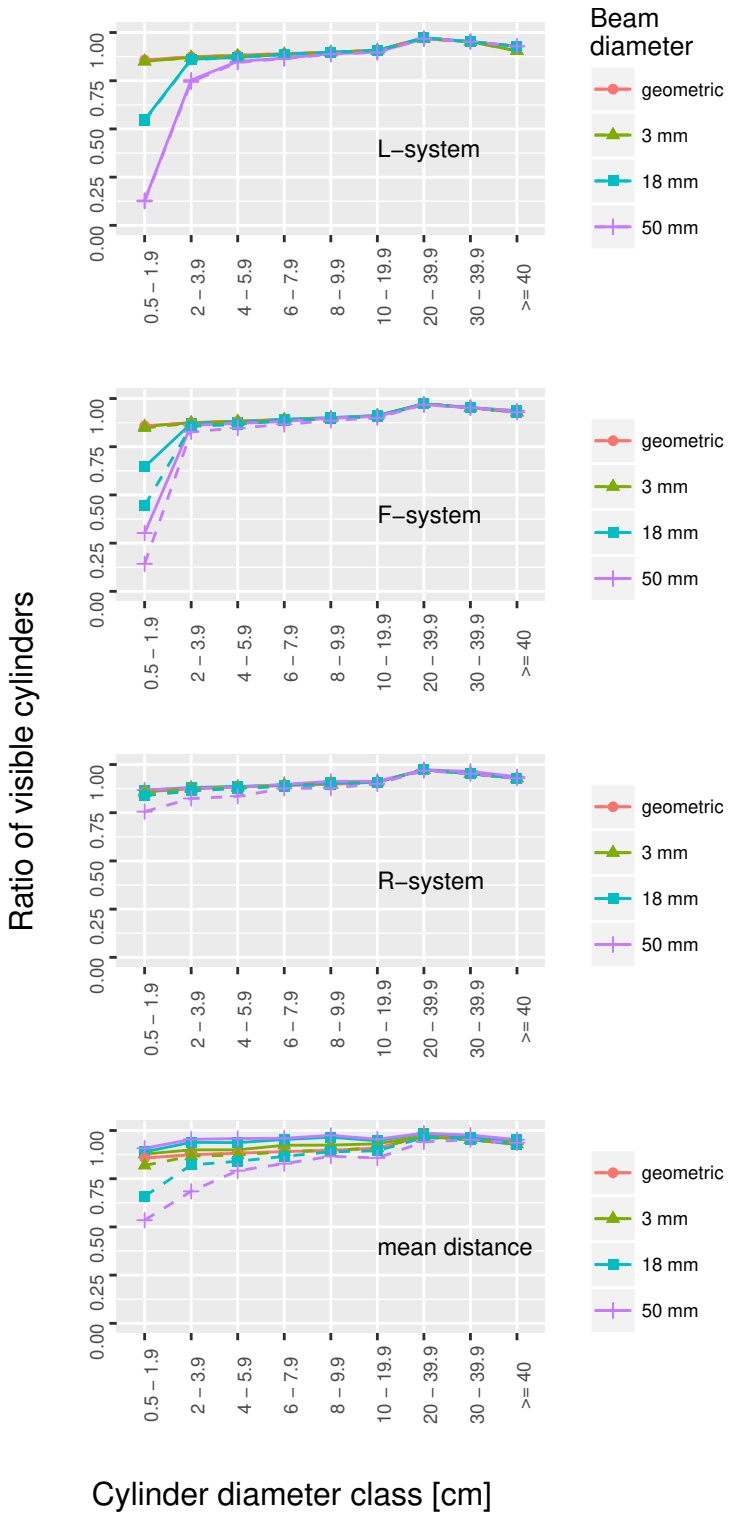

Figure S3.1: Ratio of the number of cylinders with at least one "hit" to the total number of cylinders on 170 square plots with an edge length of 10 m in forest stands with tree densities of more than 4,000 trees per hectare, by cylinder diameter class, signal triggering model and laser beam diameter at exit. Dashed line: number of visible cylinders after filtering the point cloud.

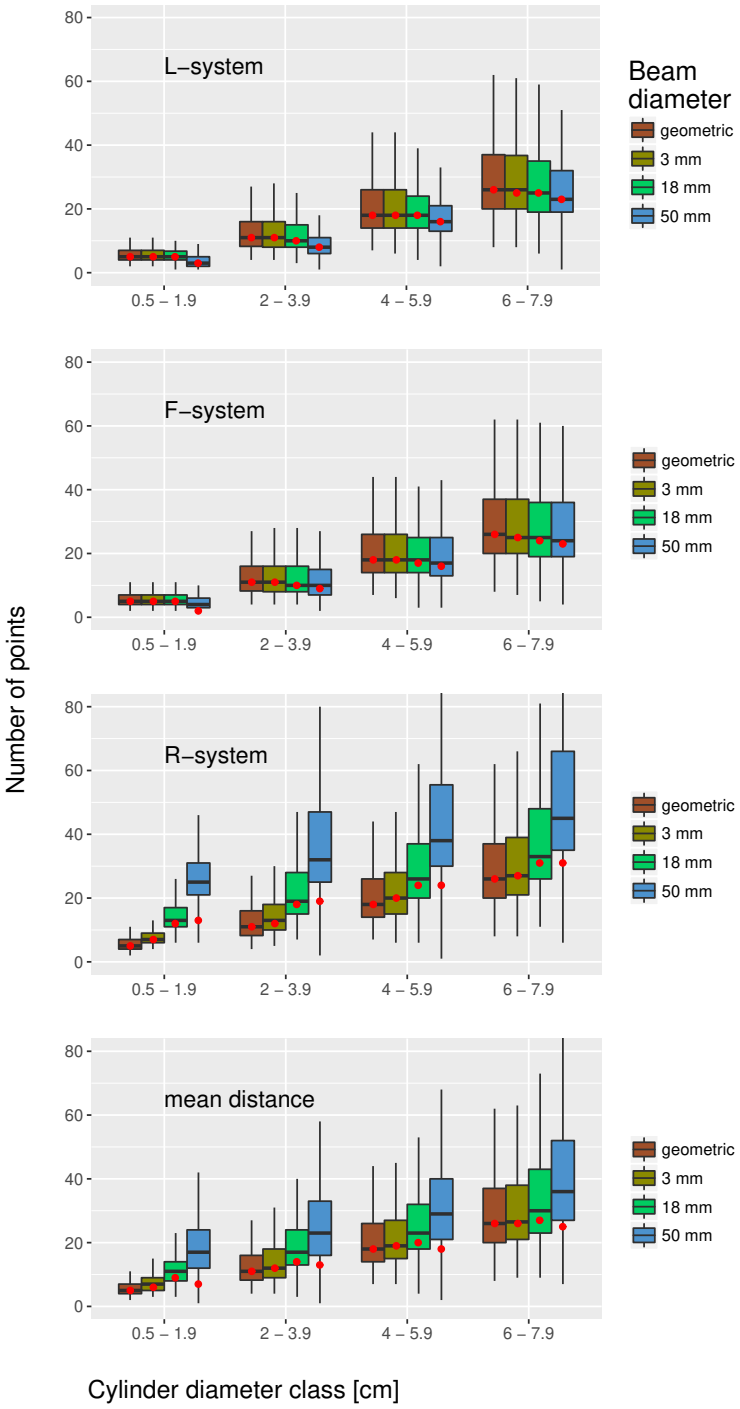

Figure S3.2: Number of points per cylinder in simulation experiments for 170 square sample plots of 10 x 10 m in forest stands with tree densities of more than 4,000 trees per hectare. Only cylinders that have at least one point in all the simulated scanning settings are evaluated. Box plots show the variation in the number of points per cylinder for different cylinder diameters, point triggering models and laser beam diameters at exit from the scanner. The red dots indicate the median number of points after filtering the point cloud (points must be closer than 10 percent of the cylinder diameter, and, if not, then closer than 2 cm). The point triggering model "geometric" simulates a laser scanner with an infinitesimally small laser beam.

3.7 References

(2007) *Laser Scanning 2007 and SilviLaser 2007*, vol. XXXVI-3/W52 of *International Archives of the Photogrammetry, Remote Sensing and Spatial Information Sciences*.

Abegg M, Kükenbrink D, Zell J, Schaepman ME, Morsdorf F (2017) Terrestrial laser scanning for forest inventories - tree diameter distribution and scanner location impact on occlusion. *Forests*, **8**, 1 – 29.

Adams MD, Kerstens AJ (1996) The interpretation of phase and intensity data from amcw light detection sensors for reliable ranging. *International Journal of Robotics Research*, **15**, 441 – 458.

Bienert A, Scheller S, Keane E, Mohan F, Nugent C (2007) Tree detection and diameter estimations by analysis of forest terrestrial laserscanner point clouds. In: ISP (2007), pp. 50 – 55.

Binney J, Sukhatme GS (2009) 3d tree reconstruction from laser range data. In: *Robotics and Automation, ICRA'09 IEEE international Conference*. Kobe, Japan.

Blender Online Community (2015) *Blender - a 3D modelling and rendering package*. Blender Foundation, Blender Institute, Amsterdam.

Disney M, Kalogirou V, Lewis P, Prieto-Blanco A, Hancock S, Pfeifer M (2010) Simulating the impact of discrete-return lidar system and survey characteristics over young conifer and broadleaf forests. *Remote Sensing of Environment*, **114**, 1546 – 1560.

Disney M, Lewis P, Raumonen P (2012) Testing a new vegetation structure retrieval algorithm from terrestrial lidar scanner data using 3d models. In: *Silvilaser 2012*, SL2012-049. Vancouver, Canada.

FAO (2018) *The state of the World's Forests 2018. Forest pathways to sustainable development.* Food and Agriculture Organistation of the United Nations (FAO), Rome.

FARO (2013) *FARO Laser Scanner Focus ^{3D}*. FARO Technologies Inc., Lake Mary, USA.

Govaerts YM, Verstraete MM (1998) Raytran: A monte carlo ray-tracing model to compute light scattering in three-dimensional heterogeneous media. *IEEE Transactions on Geoscience and Remote Sensing*, **36**, 493 – 505.

Gschwandtner M, Kwitt R, Uhl A, Pre W (2011) Blensor: Blender sensor simulation toolbox. In: *Advances in Visual Computing: 7th International Symposium (ISVC 2011)*, vol. Volume 6939/2011 (eds. Bebis R, Boyle B, Parvin D, Koracin R, Chung, Hammoud R), pp. 199 – 208. Springer Verlag, Las Vegas, USA.

Heinzel J, Huber MO (2017) Tree stem diameter estimation from volumetric tls image data. *remote sensing*, **9**.

Hough PVC (1962) Method and means for recognizing complex patterns.

Hovi A, Korpela I (2014) Real and simulated waveform-recording lidar data in juvenile boreal forest vegetation. *Remote Sensing of Environment*, **140**, 665 – 678.

Jutzi B, Stilla U (2005) Measuring and processing the waveform of laser pulses. *Optical*, pp. 194 – 203.

Kaasalainen S, Kukko A, Lindroos T, Litkey P, Kaartinen H, Hyyppä J, Ahokas E (2008) Brightness measurements and calibration with ariborne and terrestrial laser scanners. *IEEE Transactions on Geoscience and Remote Sensing*, **46**.

Koenig K, Höfle B, Müller L, Hämmerle M, Jarmer T, Siegmann B, Lilienthal H (2013) Radiometric correction of terrestrial lidar data for mapping of harvest residues density. In: *ISPRS Annals of the Photogrammetry, Remote Sensing and Spatial Information Sciences*.

Kukko A, Hyyppä J (2007) Laser scanner simulator for system analysis and algorithm development: A case with forest measurements. In: *Laser Scanning 2007 and SilviLaser 2007*.

Leica (2017) *Leica BLK360 Imaging Scanner. 3D Reality. Now.* Leica Geosystems AG, Heerbrugg, Switzerland.

Lewis P (1999) Three-dimensional plant modelling for remote sensing simulation studies using the botanical plant modelling system. *Agronomie*, **19**, 185 – 210.

Liang X, Kankare V, Hyyppä J, *et al.* (2016) Terrestrial laser scanning in forest inventories. *ISPRS Journal of Photogrammetry and Remote Sensing*, **115**, 63 – 77.

Lovell J, Jupp D, Newnham G, Coops N, Culvenor D (2005) Simulation study for finding optimal lidar acquisition parameters for forest height retrieval. *Forest Ecology and Management*, **214**, 398 – 412.

Maas HG, Vosselman G, eds. (2010) *Airborne and Terrestrial Laser Scanning*. CRC Press.

Mallet C, Bretar F (2009) Full-waveform topographic lidar: State-of-the-art. *ISPRS Journal of Photogrammetry and Remote Sensing*, **64**, 1 – 16.

Mandallaz D (2006) *Sampling Techniques for Forest Inventories*. Chapman & Hall/CRC Applied Environmental Statistics. Chapman and Hall/CRC, Boca Raton, USA.

Morsdorf F, Kükenbrink D, Schneider D, Abegg M, Schaepman ME (2018) Close-range laser scanning in forests: towards physically based semantics across scales. *Interface focus*, **8**.

Newnham G, Armston J, Muir J, *et al.* (2012) Evaluation of terrestrial laser scanner for measuring vegetation structure. *CSIRO Sustainable Agriculture Flagship*, pp. 1 – 32.

Pan Y, Birdsey RA, Fang J, *et al.* (2011) A large and persistent carbon sink in the world's forests. *Science*, **333**, 988 – 993.

R Core Team (2017) *R: A Language and Environment for Statistical Computing*. R Foundation for Statistical Computing, Vienna, Austria.

Riegl (2015) *Data Sheet, RIEGL VZ-1000*. Riegl Laser Measurement Systems GmbH, Horn, Austria.

Shvidenko A, Barber CV, Persson R (2005) *Forest and Woodland Systems*, chap. 21, pp. 585 – 621. Island Press.

Simonse M, Aschoff T, Spiecker H, Thies M (2003) Automatic determination of forest inventory parameters using terrestrial laser scanning. In: *Proceedings of the ScandLaser Scientific Workshop on Airborne Laser Scanning of Forests*, pp. 251–257. Umeå, Sweden.

Szwarcbaum I, Shaviv G (1976) A monte-carlo model for the ratiation field in plant canopies. *Agricultural Meteorology*, **17**, 333 – 352.

Van der Zande D, Jonckheere I, Stuckens J, Verstraeten WW, Coppin P (2008) Sampling design of ground-based lidar measurements of forest canopy structure and its effect on shadowing. *Canadian Journal of Remote Sensing*, **34**, 526 – 538.

Wagner W, Ullrich A, Melzer T, Briese C, K K (2004) From single-pulse to full-waveform airborne laser scanners: Potential and practical challenges. In: *Proceedings of ISPRS XXth congress*, vol. XXXV (ed. Altan O).

Waser LT, Ginzler C, Rehush N (2017) Wall-to-wall tree type mapping from countrywide airborne remote sensing surveys. *Remote Sensing*, **9**.

Chapter

4

Tree volume estimation with terrestrial laser scanning – testing for bias in a 3D virtual environment

This chapter is based on the peer-reviewed article:
***Abegg, M.**, Bösch, R., Morsdorf, F. (under Review) Tree volume estimation with terrestrial laser scanning – testing for bias in a 3D virtual environment. Agricultural and Forest Meteorology.*
It is reprinted as the final submitted manuscript and has been modified to fit the layout of this thesis.

M.A. designed the experiments, performed the analysis and interpreted the results. R. B. contributed to the code of the laserbeam simulation, the experimental design and content of the publication. F.M. contributed to the experimental design and analysis. All authors wrote and reviewed the manuscript with main contribution of M.A.

Abstract

Tree volume is a key feature in forest monitoring, delivering information, such as wood availability or forest carbon balance. To date, tree volume cannot be measured directly with conventional tools. Terrestrial laser scanning (TLS) offers the potential to directly measure tree volume. However, its application in forest monitoring requires a profound understanding of the precision and accuracy of retrieval approaches. In this study, we present a simulation environment for evaluating TLS application in forest inventories. We investigate the influence of understorey density and scanner placement on volume estimation of tree parts of varying diameters. Using information from 18 sample plots from the Swiss NFI to simulate 102 sample trees, we evaluate three understorey densities, five scanner locations and their combinations. We show that volume estimates from point clouds are biased to certain extent: from 25% for small trees to a few percent for larger trees above 40 cm diameter at breast height (DBH). Especially small tree parts (diameters $<$ 7 cm) lack precise estimation (50% mean overestimation for small trees starting with 13 cm DBH developing to 50% mean underestimation in large trees $\geq$ 75 cm DBH). Volume estimaton of small tree parts are subject to physical limits of TLS, however the estimation of volume of large tree parts could be feasible with appropriate TLS settings and field protocols. Nevertheless, tree volume estimation using TLS must be understood in greater depth before it can be applied regularly in forest inventories.

4.1 Introduction

National forest inventories (NFI) are an established process to provide data, on the national and the international level, on forests and their contribution to human welfare (FOREST EUROPE, 2015; MacDicken *et al.*, 2016). The impact of global climate change leads to greater interest in the role of forests as carbon sinks or sources (Pan *et al.*, 2011). Tree volume, which is closely connected to tree biomass and carbon stock, is one of the most important forest features forming the basis of NFI reporting. With traditional NFI tools, such as the calliper, to measure tree diameters, tree volume cannot be measured directly. Tree volume and biomass are derived with allometric models using tree diameter at breast height (DBH) as the most important explanatory variable (Chave *et al.*, 2014; Brassel & Lischke, 2001). However, these models suffer from the lack of variables describing the tree above the breast height. Sometimes tree height and the upper diameter of the tree stem can be measured in the field, providing more accurate volume estimate for the tree stem. Nonetheless, for the volume of tree branches, allometric relationships between the stem and the tree crown (branches) are applied. In Switzerland these models are based on historical destructive sampling data (Brassel & Lischke, 2001), that is not completely

representative of the whole country. Yet, from an inventory statistical point of view, calibration of volume models on trees from the representative sampling grid of the NFI would be beneficial. Further, Saarinen *et al.* (2017) point out that there is a growing interest in utilizing terrestrial laser scanning (TLS) as a basis for developing stem volume models. TLS is a technology that could provide accurate measurements of complete trees in a hight degree of detail. For inventory purposes, however, it is crucial to know the accuracy and precision of TLS-based volume estimates aiming for bias-free estimates of tree volume. Furthermore, additional measurements usually lead to additional costs. Hence, a possible improvement of volume estimations with TLS measurements compared with the current allometric approach must be proven before TLS can be implemented in the NFI workflow.

Saarinen *et al.* (2017) investigated the applicability of TLS in the development of new stem volume models (equations) based on diameter measurements through cylinder-fitting along the stem. For their workflow, they evaluated optimal scanning distances. They compared tree volume derived by TLS diameter measurements to nine destructively sampled trees (Scots pine, Norway spruce and Birch). Calders *et al.* (2015) compared biomass estimates from the application of the software treeQSM (Raumonen *et al.*, 2013) on TLS point clouds of 74 destructively sampled trees in an Australian Eucalyptus forest. Bremer *et al.* (2013) investigated the influence of various TLS scanning settings (angular resolution, single and multiple scanning) by manipulating the point cloud of one scanned tree from three different scanning locations. These studies give insight in TLS application characteristics in specific situations. However, every intended TLS application might have its own peculiarities, owing to the forest structure, the TLS device or the applied algorithms.

As destructive sampling is labour intensive, simulation of TLS could be a way of exploring its properties at a relatively low cost. LiDAR in forested environments has been simulated before (e.g. Lovell *et al.*, 2005; Lewis, 1999; Van der Zande *et al.*, 2008; Gastellu-Etchegorry *et al.*, 2015; Kukko & Hyyppä, 2007; Disney *et al.*, 2010; Morsdorf *et al.*, 2009), however, most of these approaches are focussed on airborne LiDAR simulations with different observation geometries and distances. Nevertheless some authors (e.g. Disney *et al.*, 2012; Binney & Sukhatme, 2009)), simulate TLS data of one tree (or tree part) to validate approaches of tree reconstruction from forest TLS point clouds.

As stated by various authors (e.g. Watt & Donoghue, 2005; Trochta *et al.*, 2013; Van der Zande *et al.*, 2006), occlusion is a major problem for TLS in forests. One way to overcome this problem is by combining multiple point clouds from different locations in a stand. Different scanner placement patterns are described in the literature (e.g. Watt & Donoghue, 2005; Wezyk *et al.*, 2007; Yang *et al.*, 2013; Liang *et al.*, 2016). Trochta *et al.* (2013) evaluated different distances between scanners and trees for an optimal stem recognition, whereas Van der Zande *et al.* (2008) compared three scanner position combinations in three stands. A more extensive evaluation of possible scanning positions in a wide range of stand properties was

conducted by Abegg *et al.* (2017). However, they assessed forest stands and scanner placement in terms of optimal visibility only.
For the application of TLS in forest inventories, the parameters influencing LiDAR point cloud characteristics, such as stand condition, stem and understorey density, TLS device, scanner placement and tree shape, must be understood in detail for estimates including tree volume. The added cost and complexity of introducing TLS to NFIs have to be offset by an increase in wood volume retrieval quality. The latter has the dimensions precision (variation), accuracy (bias) and extent (e.g. by sampling more trees and/or more parts of trees).
In this study, we introduced an evaluation approach for TLS applications in forest inventories. As the target variable we used tree volume. To confirm the hypothesis of Abegg *et al.* (2019), that only larger object diameters can be represented by TLS, we divided the volume of the trees into merchantable wood, which comprises all above-ground parts with a diameter ≥ 7 cm, and the wood of small branches and the tree top, which comprises the above-ground tree parts < 7 cm in diameter. Hence, the goal of this study is to: (i) implement a TLS simulation environment for forest inventories, (ii) determine the influence of object diameters on volume estimates, (iii) check whether understorey density affects the quality of tree volume estimates and (iv) test whether including multiple scanner locations improves the precision of volume estimates.

4.2 Materials and Methods

4.2.1 Simulated forest stands

4.2.1a NFI forest and tree information

The Swiss NFI collects data on a regular sampling grid with a mesh size of 1.41 km over the entire area of Switzerland. This provides data on forest stands, trees and site conditions for 6357 forest sample plots with a wide range of features. Data on trees starting at 10 cm height are measured on circular sample plots. However, the location of the trees is only recorded for the ones with a diameter at breast height (DBH) of at least 12 cm.
For our study, we used information on the trees with DBH ≥ 12 cm, which are used in the forest resources estimations. The sample plot covers a horizontal circle with an area of 200 m^2. Furthermore, we focussed on deciduous trees where the crown shape represents a complex geometry and more biomass is stored in the branches compared to coniferous trees (Brassel & Lischke, 2001). Additionally, we selected only single-layered stands, because understorey is one of the parameters influencing laser scanning. The selected sample plots for simulations consisted of only standing and living trees.

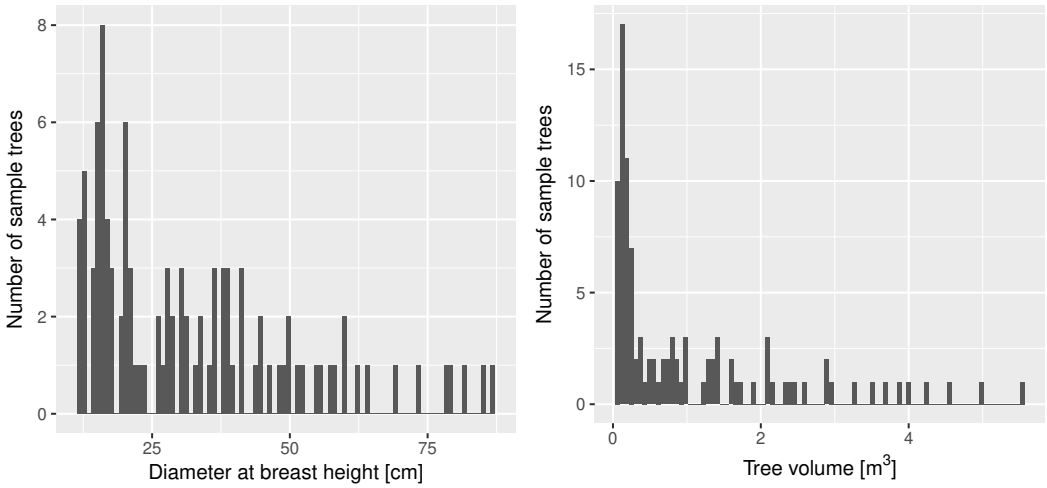

Figure 4.1: Diameter and total tree volume distribution of the scanned sample trees.

We tested three understorey densities, 0, 2800 and 8000 individuals per hectare, within each of the 18 sample plots with an overall total of 102 sample trees. The diameter distribution of the sample trees is displayed in Figure 4.1. The forest ground was defined as a horizontal and plane surface.
As tree information, we used the location of the trees on the NFI sample plots and the DBH. Tree height was derived from the estimated stand height. According to the field manual of the Swiss NFI (Keller, 2011), tree crown length is assigned to one of three classes: more than half the tree height, between half the tree height and one quarter of the tree height, and less than one quarter of the tree height). However, we limited crown length to start above the understorey and cover at least 20% of the tree height.

4.2.1b Tree model

One of the objectives of this study is to demonstrate the influence of understorey on the quality of TLS volume estimates of trees in forests. The sapling tree add-on for the software Blender is based on the work of Weber & Penn (1995). It makes it possible to generate trees of a wide range of shapes and tree crown structures. As we are interested in the occlusion effects due to understorey density and the perspective of the laser scanner on the trees, the tree shape must represent a tree like structure. The sapling tree add-on produces tree shapes with conical stems and branches up to six branching levels. The stem/branch length, curvature and direction can be specified for each branching level up to level four. The branches are distributed on a parent branch/stem in a helical way. We parametrized the tree model as displayed in Table S4.1 in the Appendix, in order to produce trees like the ones shown in Figure 4.2.

Figure 4.2: Image rendered in Blender of a simulated sample plot with trees and understorey.

4.2.2 TLS simulation and point cloud processing

4.2.2a Simulation of laser scanning with Blender

Blender (Blender Online Community, 2015), a 3D content creation suite, is designed to render images and movies of complex virtual 3D scenes. It offers a large toolbox to create 3D objects and define their light interaction properties. The add-on BlenSor (Gschwandtner *et al.*, 2011) enables access to internal parts of Blender where the interaction of light rays with 3D objects is calculated. Originally, the BlenSor add-on was designed for simulations of various vehicle-mounted sensors. Abegg *et al.* (2019) developed it further to simulate realistic properties of three state-of-the-art terrestrial laser scanners. Implemented features were the prefiltering of points, in cases where the virtual laser pulse intersects with multiple objects and the triggering of multiple echoes from one laser pulse. Furthermore, different angular resolutions, laser beam diameters upon exit from the device, and beam divergences can all be simulated.

4.2.2b Point cloud processing

The simulation of laser scanning with an angular resolution of 0.04°is computational demanding. In order to reduce the calculation time, the scan of one scene was divided into 150 longitudinal (horizontal) slices. This enables the TLS simulation

of each slice of the scene separately, via parallel processing on a high performance computer. The point cloud for one scanning position was then recomposed from the different slices using a python script. The same approach was applied to combine point clouds from multiple scanning locations. With the known positions of the trees, height of the understorey layer and extent of the tree crowns, the trees could be clipped automatically from the point cloud, without the need for an error-prone manual or automated segmentation.

4.2.3 Volume calculation

In this study, we compared the volume of the 3D tree models with the tree volumes calculated from the simulated point clouds.
The volume derivation of the 3D model works as follows: The Blender sapling tree add-on defines trees as a Bezier curve (Bézier, 1977) with diameters assigned along the curve. In Blender, the diameter, which describes a tube-like shape, is named bevel. For the processing of the tree model, each branch is labeled with a separate identifier. With a Blender native function, we converted the spline and its corresponding bevel to a closed, triangulated mesh for each tree part (stem, branches, twigs). The defined trees still had overlapping parts at each branch start (the branch is originally defined as a spline with no diameter, so the origin of a branch is always in the centre of the parent branch/stem). We removed these overlapping parts using a Blender native functionality to avoid double accounting for their volume.
To prove the influence of the object diameter on the volume estimate, the branches were cut off at 7 cm (threshold for merchantable wood). This enabled us to calculate the total tree volume, the volume of tree parts with diameters above the threshold (merchantable wood) and their difference (the volume of small tree parts). We used geometric functions to iterate through the stem and branches to search the diameter threshold.
The volume of the trees was calculated according to the procedure described by Zhang & Chen (2001): each triangle of the object's mesh structure represents a tetrahedron with the origin of the scene and a specific volume. The volume of these tetrahedrons can be positive or negative relative to the direction of the normal vector. The sum of all (positive and negative) volumes equals the volume of the whole tree. The tree volume derived from the point cloud was calculated according to Raumonen *et al.* (2011, 2013) with an open-source Matlab script called treeQSM. TreeQSM was tested with field measurements and with simulated data (Brede *et al.*, 2019; Lau *et al.*, 2019; Pitkänen *et al.*, 2019; Calders *et al.*, 2015; Disney *et al.*, 2012).

4.2.4 Workflow of simulation and analysis

4.2.4a Preparatory steps: selection of the parameters to be tested

We selected 18 sample plots which fulfil the following conditions: only deciduous, living and standing trees of various diameters (12 - 87 cm) in single-layered stands with various tree numbers per plot (2 - 17).
The five scanner locations were selected manually so that locations were equally distributed within the sample plot and covered various aspects of the trees, following the recommendations of Abegg *et al.* (2017). One scanner location was set to the centre of the sample plot.
We selected three different densities of the understorey layer: 0 (no understorey at all), 2800 and 8000 individuals per hectare. These densities were implemented on each sample plot. The height of the understorey layer was set to 4 m.
Finally, we chose the angular resolution of the scanner (0.04°) and set the signal triggering approach to be a Faro^{3D}-like behaviour (F-system) with a beam divergence of 0.19°, a beam diameter at exit of 4.24 mm ($1/e^2$ definition) and an uncertainty (standard deviation) in the distance measurement of 2 mm. The F-system is a discrete TLS system which triggers one point per laser pulse. We chose the F-system because it can perform hemispherical scans and has a scanning range of up to 120 m. When a laser pulse intersects with multiple objects, it either prefilters the signal, returning no point, or it displays two kinds of distance deviation from the actual objects, depending on the distance of the objects to each other (for details see Abegg *et al.*, 2019).

4.2.4b Preparation and measurement of 3D tree models

We extracted data on tree positions, diameters, heights and crown length classes from the NFI sample plots. Using the sapling tree add-on in Blender, we defined the tree parts as Bezier curves with an assigned diameter (bevel). After conversion to a mesh, the trees were saved as a scene so that they could be linked to a Blender scene with the other trees of that sample plot. We calculated the 3D model volume of the whole tree and for tree parts up to a diameter threshold of 7 cm as described in Section 4.2.3.

4.2.4c Preparation and scanning of 3D sample plot

The 3D scene to be scanned was composed of the tree models which were linked to the scene and a forest ground containing the understorey as a particle system. The particle system is a Blender functionality, similar to linking existing tree models to a scene, defining the random location of instances of any previously defined object. This reduces memory demand considerably, allowing scenes to consist of more than 10,000 objects. We used the particle system to fill the Blender forest scene with 0, 2800 and 8000 instances of three sapling trees per hectare. The sapling trees consisted of individuals with one of three branching levels (1, 2 and 3), which were

then randomly selected to compose the understorey. The understorey trees were produced with Blender's sapling tree add-on using the parameters displayed in Table S4.2 in the Appendix. The understorey height was set to 4 m. Additionally, the understorey trees were not placed within a buffer of 0.5 m around the locations of the sample trees and the scanner. Our goal was to compare TLS scans of the same scenes with and without an understorey layer (see Section 4.2.4a). For each scanner location and tested understorey density, the virtual sample plot scenes were scanned with the above-defined simulation specifications. To make use of parallel processing, the horizontal scanning was split into 150 sub-scans.

4.2.4d Preparation and analysis of point cloud

Before analysing the point cloud, the sub-scans of one sample plot scene were combined. These single scan point clouds were then registered to a multiple-scan point cloud combining the point clouds of the five scanner locations on each sample plot in the following way: combination of the two opposite scanner locations, combination of the two opposite scanner locations with the central location, combination of all scanner locations without the central location, and combination of all scanner locations.
The trees were clipped from the point clouds using the known location, height, crown base height and understorey height.
The tree point clouds were then analysed in Matlab using treeQSM (Raumonen *et al.*, 2013), providing the tree volume above and below the diameter threshold of 7 cm.

4.3 Results

4.3.1 Influence of object size on volume estimation

Figure 4.3 shows the bias of wood volume, derived by QSM, applied to the simulated point clouds of trees scanned from multiple scanning positions. For merchantable wood (diameter $\geq$ 7 cm) the QSM consistently overestimates the true volume. The bias of the volume estimate in relation to the respective tree volume is considerably high (up to a mean of 25%), especially for small trees. However, absolute values are larger for big trees. When small branches and the tree top (diameter $<$ 7 cm) are considered, the QSM derived values show over- or under-estimations, depending on the tree size. Furthermore, the variation in the bias of small branches and the tree top is higher compared with the values for merchantable wood.

4.3.2 Influence of scanning system on volume estimations

As described in Abegg *et al.* (2019), the TLS simulation environment can simulate different LiDAR echo triggering systems. For this study, we tested a Faro^{3D}-like (F-

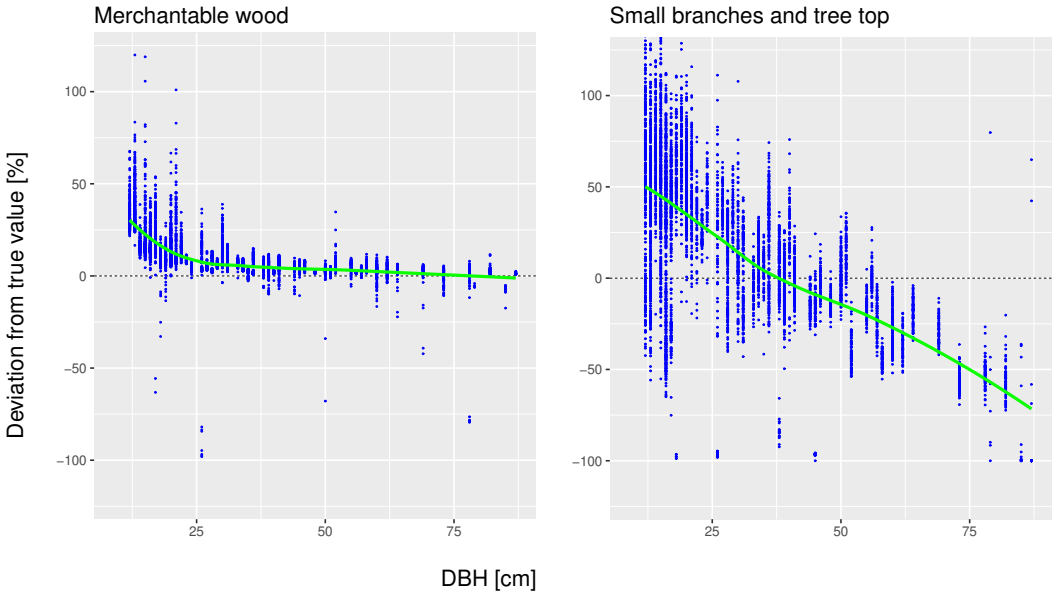

Figure 4.3: Influence of object size on the quality of volume estimations from point clouds with multiple scanning positions in simulated stands. For each tree point cloud, the range of deviation (bias) of the QSM output compared with the actual volume of the 3D model is displayed as blue dots. The green line is a "loess" smoothing line on the data (R Core Team, 2017). The left panel shows the bias of the volume estimates for merchantable wood(diameter $\geq$ 7 cm), and the right panel shows the bias of volume estimates for small branches and the tree top (diameter $<$ 7 cm).

system) echo triggering approach, which includes prefiltering LiDAR pulses reflected by multiple objects (mixed pixel effect) and distance deviation from mixed pixel effects that are not prefiltered. Additionally, we simulated geometric scanning (using an infinitesimally small laser beam) to compare the results of the F-system with a "perfect" scanning system.

Figure 4.4 shows that the QSM starting parameters similarly influence the variation in the QSM estimation for both systems, i.e. volume estimates of small trees varies more than the (true) 3D model volume. For merchantable wood (diameter $\geq$ 7 cm), the two scanning systems perform similarly, with a slightly higher variation with the F-system. Concerning the volume estimate of small branches and the tree top (tree parts with diameters $<$ 7 cm), the F-system-generated point clouds have considerably higher variation, especially for trees with DBH $<$ 30 cm. Additionally, the volume estimate from point clouds of the two systems display an offset from each other by around 50%, with the F-system point clouds consistently delivering a larger volume than geometric scanning.

4.3.3 Influence of understorey on volume estimations

Figure 4.5 shows the potential influence of understorey density on the volume estimates for point clouds from five different locations. In the simulations there seems to be no influence of the understorey, even with understorey stem densities of

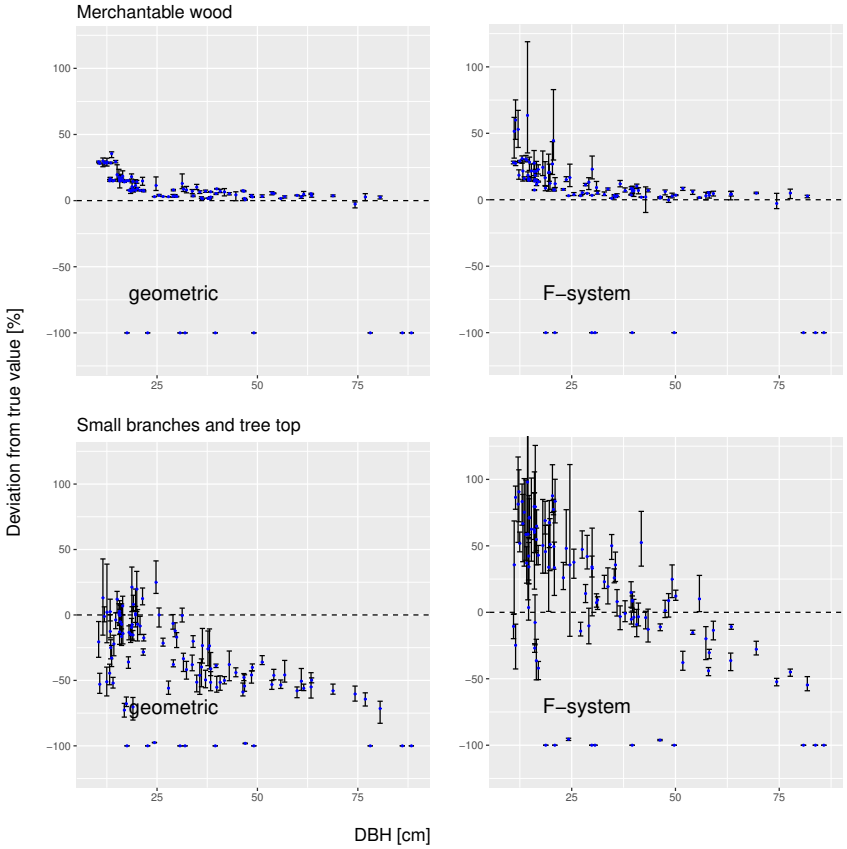

Figure 4.4: Influence of the scanning system on the quality of volume estimations from point clouds of five scanning positions in simulated forest stands with no understorey. For each tree point cloud, the deviation (bias) of the QSM outputs compared with the actual volume of the 3D tree model is displayed (black whiskers for the ranges, blue dots for the mean deviations). The upper panels show the bias of the volume estimates for merchantable wood (diameter $\geq$ 7 cm), and the lower panels show the bias of the volume for small branches and the tree top (diameter $<$ 7 cm). The left panels show the outcome of geometric scanning (with infinitesimally small laser beams), whereas the right panels show the outcome of a Faro^{3D}-like (F-system) signal triggering approach.

8000 pieces per hectare. Nevertheless, the ratio of failed volume calculations rises slightly with increasing understorey density, by about 1.2%.

4.3.4 Influence of multiple scanner positions on volume estimations

Figure 4.6 compares the volume estimates of point clouds with different numbers of combined scanner locations. Among the point clouds from multiple scanning locations there is no visible difference. Interestingly, the variation in the QSM parameters seems to lead to more variable results as more point clouds are combined. Additionally, the number of failed QSMs for single scan positions is higher than the number of failed QSMs for the combined scanner locations (14.5% vs 8.3%).

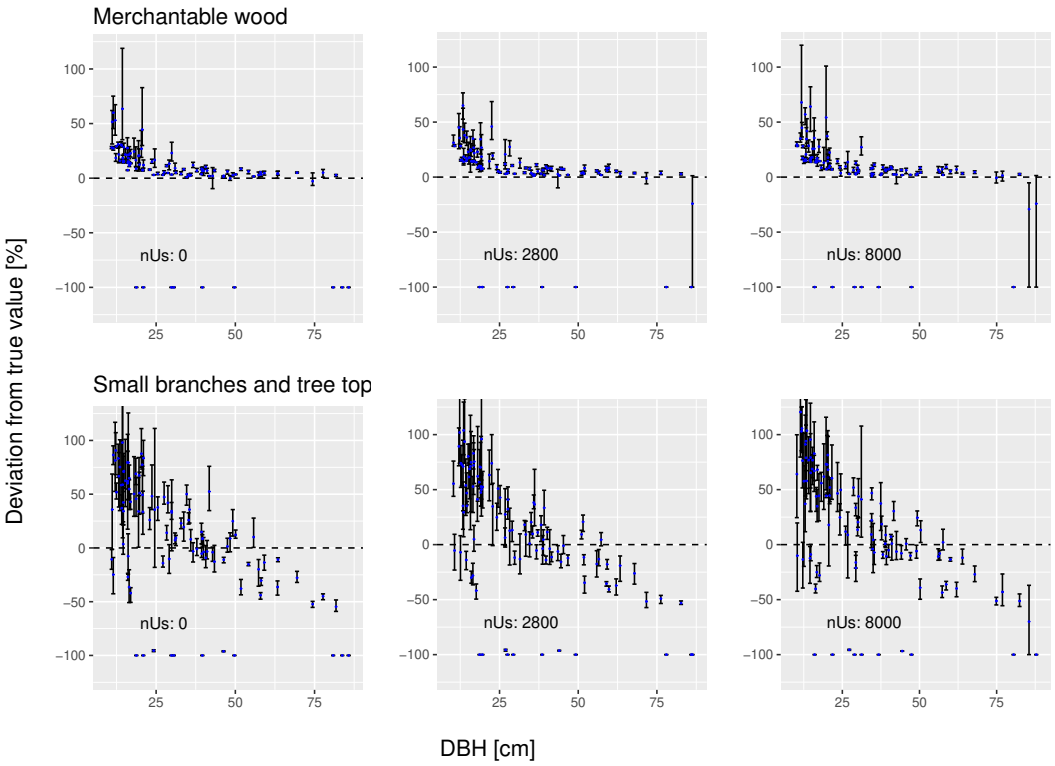

Figure 4.5: Influence of understorey density on the quality of volume estimations from point clouds. For each tree point cloud, the range of deviation (bias) of the QSM output compared with the actual volume of the 3D model is displayed. The upper panels show the bias of the volume estimates for merchantable wood (diameter $\geq$ 7 cm), and the lower panels show the bias of the volume estimates for small branches and the tree top (diameter $<$ 7 cm). From left to right, an increasing stem number (nUs) of understorey trees (4 m in height) is shown: 0, 2800 and 8000 pieces per hectare. The blue dots represent the mean deviations of QSM volume estimates based on tree point clouds, and the whiskers represent the range of volume estimates resulting from the use of different QSM starting parameters.

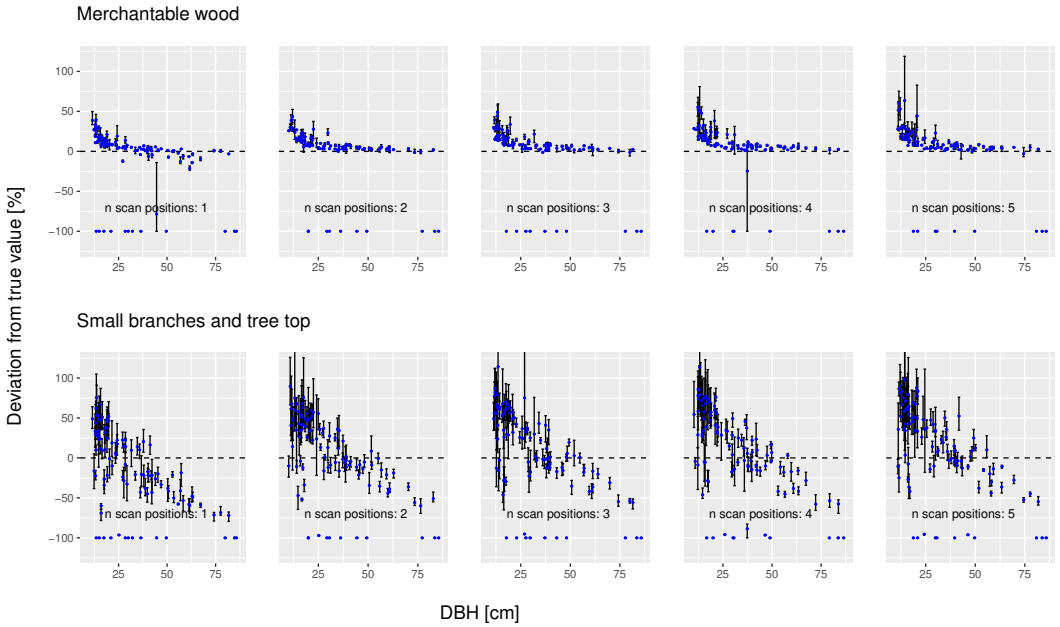

Figure 4.6: Relative bias of QSM volume estimates in simulated forest environments with different numbers of combined scanning locations, for merchantable wood ($\geq$ 7 cm diameter) and small branches/tree top ($<$ 7 cm diameter). The blue dots represent the mean deviations of QSM volume estimates based on tree point clouds and the whiskers represent the range of volume estimate resulting from the use of different QSM starting parameterss

4.4 Discussion

In this study, we present a simulation approach which enables the evaluation of the performance when TLS is applied in forest inventories. As an example, we investigate the influence of understorey density and scanner placement on the quality of tree volume estimates in deciduous forest stands without foliage.
A wide variety of possible TLS applications in forest inventories can be tested with the presented simulation environment. In particular, specific situations can be investigated under different conditions, e.g. with and without understorey or with different TLS devices. Another advantage of the simulation is the availability of a perfect "ground truth", i.e. the exact volume of the used tree models is known.
Nevertheless, simulating realistic forest environments can be very complex and the implementation effort is considerable. Simulations are always an abstraction of reality, and the results of such simulations should therefore be interpreted carefully. For this study, we chose an easily parametrizable tree model to be used within the 3D content creation suite Blender. It enables influencing a wide range of tree properties, such as diameter, tapering, length, curvature and orientation of the stem and branches. However, the difference to real tree structures is its helical branch placement on parent branches/stems. This structure is encountered in real trees as well (alternate branching), but does not cover all existing branching structures (e.g., opposite branching, whorled branching). Nevertheless, also with the helical branching structure any branch density can be emulated. Furthermore, treeQSM is designed to estimate the volume (and other parameters) of any kind of tree-like structure, without constraints on a specific structure. Hence, we are confident that the findings concerning limitations of volume estimation with TLS are realistic within our study constraints (e.g., tree model, stand structure and scanning system).
Computing resources for these TLS simulations were considerably high, in a way that access to a high-performance computer is a requirement when calculation time should not exceed months.
The simulations show that the scanning system has a large influence on the volume estimates of the tree models. Furthermore, we could observe a bias in all volume estimates, which seems to be related to tree size and the size of the estimated tree part (see Figure 4.3). Most notably, the estimate of merchantable wood (diameter $\geq$ 7 cm) is considerably more precise (less variation) and accurate (less bias) than the volume estimation of small tree parts (small branches and tree top). As for the precision of the estimates, Disney *et al.* (2012) and Calders *et al.* (2015) similarly report variation in the volume estimate which is dependent on the starting parameters of the treeQSM approach. In the case of accuracy, Raumonen *et al.* (2013) described an overestimation resulting from the treeQSM approach, whereas Calders *et al.* (2015) observed this effect when comparing volume estimates with measurements of destructively sampled trees. Possibly, the overestimation originates from an

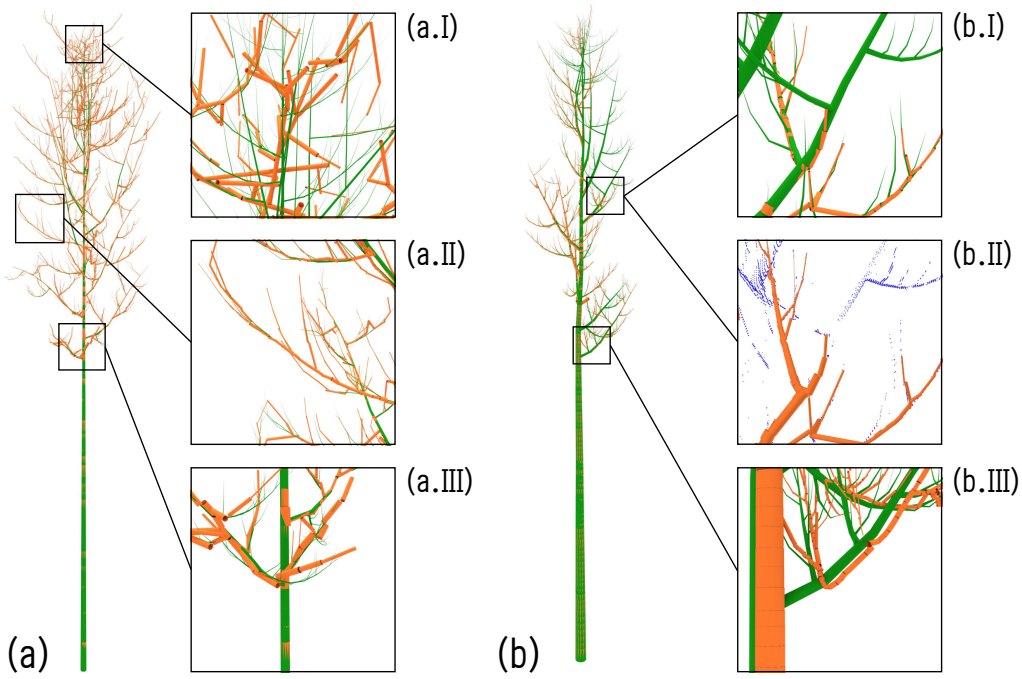

Figure 4.7: Comparison of 3D tree model (green), QSM output (orange) and points (blue dots in panel b.II). (a) shows a tree with 12 cm DBH, a tree height of 14 m and a total tree volume of 0.07 m^3. The QSM estimation of small tree parts deviate by 65% from the (true) model volume and from the merchantable wood volume by 27%. (b) shows a tree with 69 cm DBH, a tree height of 41 m and a total tree volume of 5.5 m^3. The QSM estimation of small tree parts deviate by -51% from the (true) model volume and by -3% from the merchantable wood volume. Panel (a.I) show erroneous QSM cylinder fittings, (a.II) and (a.III) show that fitted cylinders are often slightly larger than the small branches, both due to a lack of sufficient points representing the branches. Panel (b.I) and (b.II) show the influence of occlusion, which leads to difficulties in consequtive cylinder fitting. In panel (b.III) the tree model and the QSM cylinders are slightly shifted for a better comparison between the tree model and the QSM output.

overestimation of small tree parts. This is supported in our study by the fact that the volume of small trees, composed mostly of small tree parts, is clearly overestimated. The overestimation is even stronger for the volume of small tree parts (small branches and tree top; see Figure 4.3). A visual analysis of the overlay of the 3D tree model with QSM cylinders, as displayed in the panels (a.I) to (a.II) in Figure 4.7 support this hypothesis. Often cylinders are relatively large compared to the branches they represent, possibly because small branches are represented by very few point. Large trees, on the other hand, produce more occlusion within the tree crown, possibly leading to an underestimation of the volume of small branches and the tree top (see right panel in Figure 4.3). Figure 4.7 with panels (b.I) and (b.II) shows an example where the gap in a point cloud leads to a stop in cylinder fitting, leaving a whole branch not considered by the QSM. The distance to “jump” over such gaps are part of the QSM parametrisation. These hypotheses for over- and underestimamtion are further supported by the analysis of Abegg *et al.* (2019), exploring the interaction of laser beam diameter and object size in TLS applications. The study demonstrated that small objects often lack a sufficient representation in the point cloud. Additionally,

noise effects increase when scanning small objects, owing to the common occurrence of edge effects, i.e. a laser pulse intersecting with multiple objects and therefore possibly producing points not on an object's surface. Such additional noise could lead to volume overestimations, because the branch diameter appears to be larger with noise. Furthermore, the study of Abegg *et al.* (2019) demonstrated that small objects are often invisible, especially when situated at a large distance to the scanner and in a high density (e.g. in the tree crown). However, small tree parts contribute far less to the total tree volume, reducing their biasing influence on the total tree volume (see left panel in Figure 4.3).

We were not able to see an effect of understorey density on the quality of the volume estimates from TLS point clouds, even with high densities of 8000 understorey trees per hectare. However, the number of failed volume estimations is slightly higher when understorey is present. The possible influence of understorey on the applied TLS (F-system) is either occlusion, prefiltering, small distance deviation (some centimetres) on objects edges, or large distance deviation of the triggered laser echoes. The last of these effects arises when laser beams intersect with multiple objects with nearly the same amount of energy. As the setup of the forest scenes in this study was designed to allow an automatic clipping of the tree point clouds from the rest of the scene (i.e. clear separation of understorey layer from tree crowns), noise points, far from the tree, were mostly clipped from the tree point cloud. Therefore, a fraction of the distance noise could not interfere with the treeQSM for the volume estimation. The effect of occlusion and prefiltering (removing points based on ambiguous distance measurements), on the other hand, was not strong enough to reduce the quality of volume estimation systematically, especially when point clouds from multiple scanner locations were combined. However, real forest environments might consist of coniferous understorey and scanning is sometimes performed during the vegetation period; one would expect considerably stronger occlusion effects in such cases.

The combination of point clouds from multiple scanning locations has a favourable effect on the bias of the volume estimates, especially for larger trees. However, the variability in the volume estimates increases as the number of combined scanning locations increases. As Figures S4.1, S4.2, S4.3 and S4.4 in the Appendix show, the increasing variability is due to the simulated laser echo triggering system (F-system). As the F-system has a slight distance deviation at objects' edges, every additional scanning perspective adds noise according to the respective scanning direction to the object. This effect was described by Binney & Sukhatme (2009) and is observed by many TLS practitioners. This additional noise in interaction with the treeQSM parameters influences the outcome of the volume estimation, i.e., by connecting point cloud patches over "false" gaps (see Figure 4.7). Furthermore, additional points from different scanner locations increase the density of noise, which could be interpreted as proper points from objects instead of being filtered out by the treeQSM algorithm. The implemented F-system is based on laboratory experiments investigating the beha-

viour of TLS scanners when scanning edges of objects (Abegg *et al.*, 2019). However, under real conditions there are many more factors influencing laser scanning, such as reflectance properties of the scanned objects, movement of the scanned trees and more complex "mixed pixel" situations than tested in the laboratory, some of them leading to noise effects in the point cloud. We assume that in comparison with point clouds from real forest scenes retrieved with a real Faro^{3D} scanner, that the simulated point cloud is relatively clean. Hence, noise effects on volume estimation in real forests might be possibly even higher than in this study.
The tree models used here do not represent the variety of existing trees, but rather a deciduous-tree-like structure without leaves. An application of TLS in forest inventories has to additionally handle coniferous trees and different branching structures. Additionally, the stand structure in Switzerland, and elsewhere, can be far more complex than the single or double layered structure considered in this study, with an upper layer of adult trees and an understorey layer. The negative effects of TLS applications observed here are possibly even stronger when TLS is applied in a forest inventory. Nevertheless, we assume that occlusion effects and noise effects influencing the performance of treeQSM in volume estimation, as tested for stand and TLS specifications within this study, are similar to those observed in reality.
Nevertheless, volume estimates for merchantable wood of larger trees seems to be estimated with a small bias of a few percent of the total tree volume. Large trees (and large tree parts) contribute most to wood volume and biomass of forests, e.g. in Switzerland 79% of the stem volume of living trees is accounted for trees with DBH $>$ 30 cm (Abegg *et al.*, 2014). If the pending questions concerning a TLS application for tree volume estimation can be addressed, e.g., in future simulation studies, and explanations for biased volume estimates are found, TLS has the potential to become integrated in future NFI field campaigns.

The following abbreviations are used in this article:

cm	Centimetre
CPU	central processing unit
DBH	Diameter at breast height
LiDAR	Light detection and ranging
NFI	National Forest Inventory
TLS	Terrestrial laser scanning

4.5 Supplementary Material

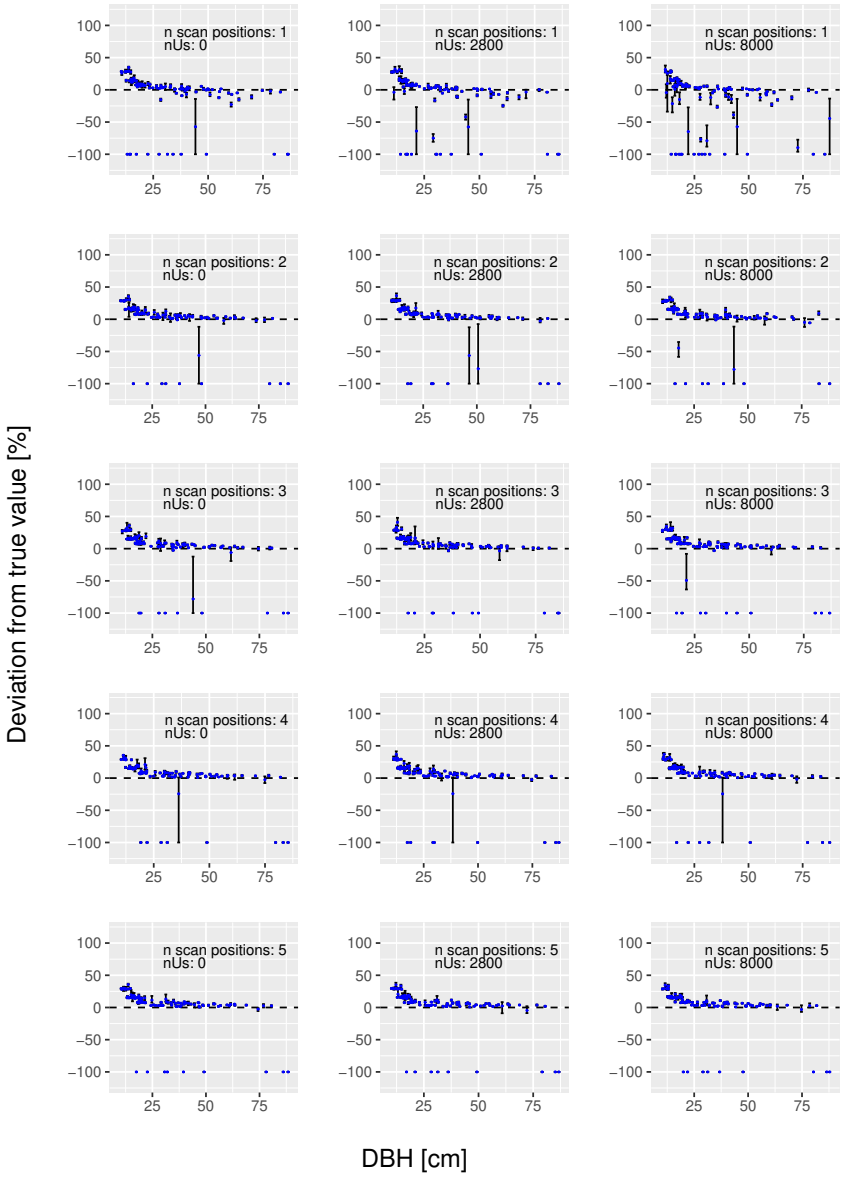

Figure S4.1: Bias of QSM in simulated forest environments with geometric scanning for merchantable wood. The blue dots represent the mean deviations of QSM volume estimates based on tree point clouds and the whiskers represent the range of volume estimates resulting from the use of different QSM starting parameters.

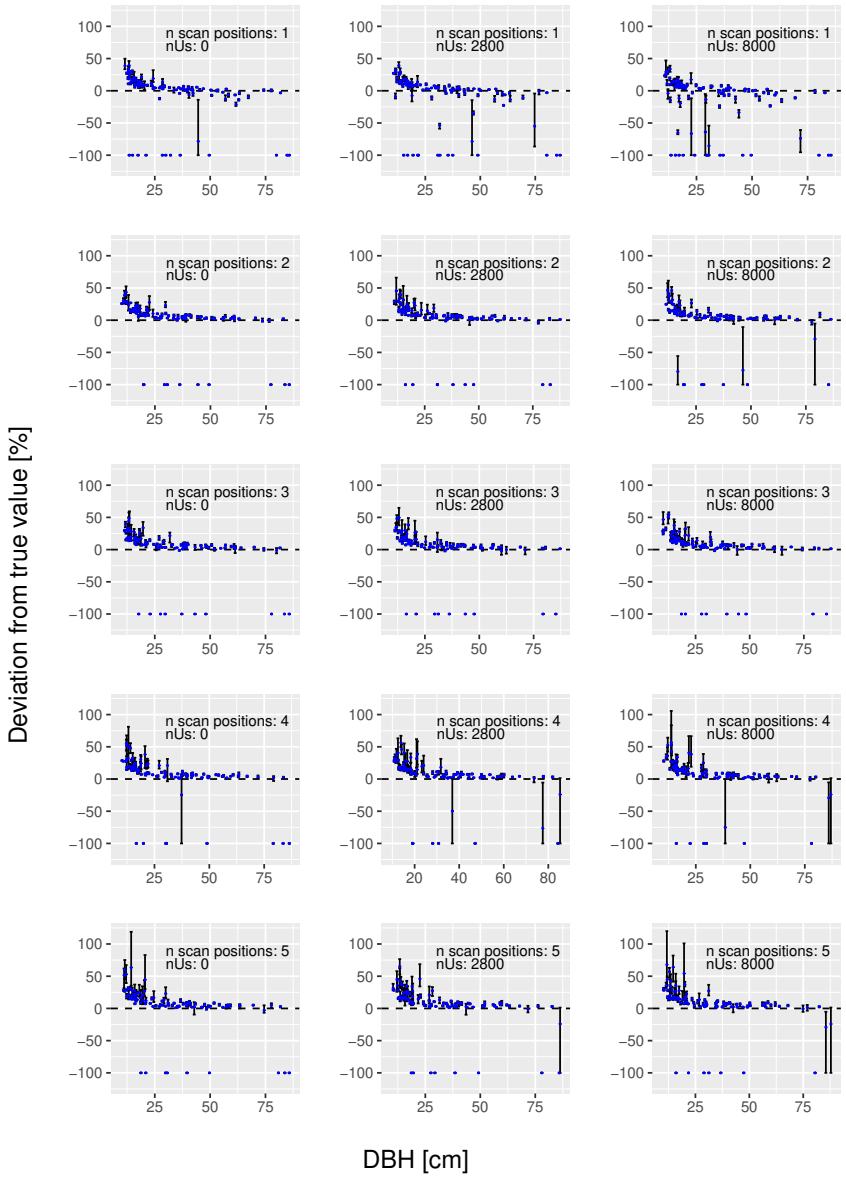

Figure S4.2: Bias of QSM in simulated forest environments with F-system scanning for merchantable wood. The blue dots represent the mean deviations of QSM volume estimates based on tree point clouds and the whiskers represent the range of volume estimates resulting from the use of different QSM starting parameters.

Table S4.1: Parameters used to define the tree model (description according to Weber & Penn (1995) and the add-on documentation).

Parameter	Value	Parameter description
prune	True	boolean parameter indicating whether the tree should be pruned at a defined envelope
levels	4	number of branching levels
length	1, 0.3, 0.6, 0.45	relative length of child branch
lengthV	0, 0.05, 0.1, 0.02	variation in the relative length
branches	0, 30, 10, 10	number of branches per parent element on each level
curveRes	10, 7, 7, 3	curvature resolution of a tree element
curve	0, -50, 0, 0	angle of the end of the branch
curveV	10, 50, -30, 0	variation of curve
curveBack	0	curvature parameter to produce s-shaped branches
baseSplits	0	number of splits of the stem
segSplits	0	number of splits per branch
splitAngle	10, 10, 10, 0	angle of the branch splitting
splitAngleV	0	variation in the branch splitting
scale	from NFI data	tree height
scaleV	0	variation in the tree height
attractUp	-2	upward growth tendency
shape	8	general tree shape id
baseSize	from NFI data	fractional branchless area at tree base
ratio	from NFI data	ratio of the radius of the stem base to the tree height
taper	1	tapering of the stem and branches
ratioPower	1.2	reduction of the child branch diameter compared to parent branch/stem
downAngle	45, 45, 90, 45	angle between the child branch and the parent branch/stem
downAngleV	0, -50, 10, 10	variation in downAngle
rotate	140, 140, 140, 77	the angle of the child branch around the axis of the parent branch/stem
rotateV	20, 20, 20, 20	variation in rotate
scale0	1	trunk scaling
scaleV0	0.2	variation in scale0
pruneWidth	from NFI data	ratio of crown diameter to the tree height
pruneWidthPeak	0.2	location of the largest crown diameter
prunePowerHigh	0.05	shape of the upper part of the tree crown
prunePowerLow	1	shape of the lower part of the tree crown
pruneRatio	1	strength of pruning
bevelRes	4	the bevel resolution of the curves
resU	4	the resolution along the curves
startCurv	0	the angle between vertical and the starting direction

Table S4.2: Parameters used to define the regeneration tree model (description according to Weber & Penn (1995) and the add-on documentation) for the understorey layer.

Parameter	Value	Parameter description
prune	True	boolean whether the tree should be pruned at a defined envelope
levels	1, 2, 3	number of branching levels
length	1, 0.3, 0.6, 0.45	relative length of child branch
lengthV	0, 0, 0, 0	variation in the relative length
branches	0, 30, 10, 10	number of branches per parent element on each level
curveRes	10, 7, 7, 3	curvature resolution of a tree element
curve	0, -50, 0, 0	angle of the end of the branch
curveV	90, 90, -30, 0	variation in curve
curveBack	0	curvature parameter to produce s-shaped branches
baseSplits	0	number of splits of the stem
segSplits	0, 0, 0, 2	number of splits per branch
splitAngle	10, 10, 10, 10	angle of the branch splitting
splitAngleV	0	variation in the branch splitting
scale	defined as parameter	tree height
scaleV	0	variation in the tree height
attractUp	0.8	upward growth tendency
shape	7	general tree shape id
baseSize	0.5	fractional branchless area at tree base
ratio	0.03/10	ratio of the radius of the stem base to the tree height
taper	1	tapering of the stem and branches
ratioPower	1.2	reduction of the child branch diameter compared to parent branch/stem
downAngle	45, 45, 90, 45	angle between the child branch and the parent branch/stem
downAngleV	0, -50, 10, 10	variation in downAngle
rotate	140, 140, 140, 77	the angle of the child branch around the axis of the parent branch/stem
rotateV	0, 0, 10, 0	variation in rotate
scale0	1	trunk scaling
scaleV0	0.2	variation in scale0
pruneWidth	0.2	ratio of crown diameter to the tree height
pruneWidthPeak	0.2	location of the largest crown diameter
prunePowerHigh	0.05	shape of the upper part of the tree crown
prunePowerLow	1	shape of the lower part of the tree crown
pruneRatio	1	strength of pruning
bevelRes	5	the bevel resolution of the curves
resU	4	the resolution along the curves
startCurv	0	the angle between vertical and the starting direction

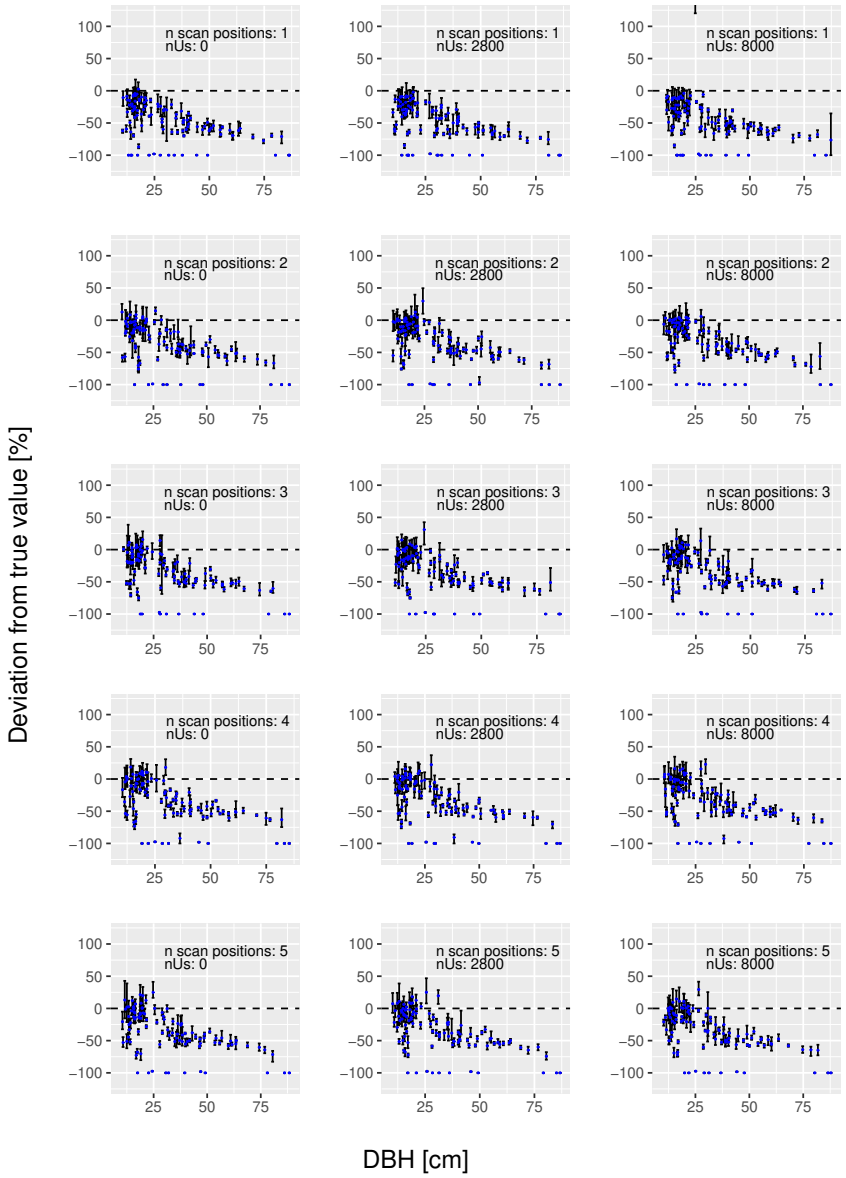

Figure S4.3: Bias of QSM in simulated forest environments with geometric scanning for small tree parts (< 7 cm diameter). The blue dots represent the mean deviations of QSM volume estimates based on tree point clouds and the whiskers represent the range of volume estimates resulting from the use of different QSM starting parameters.

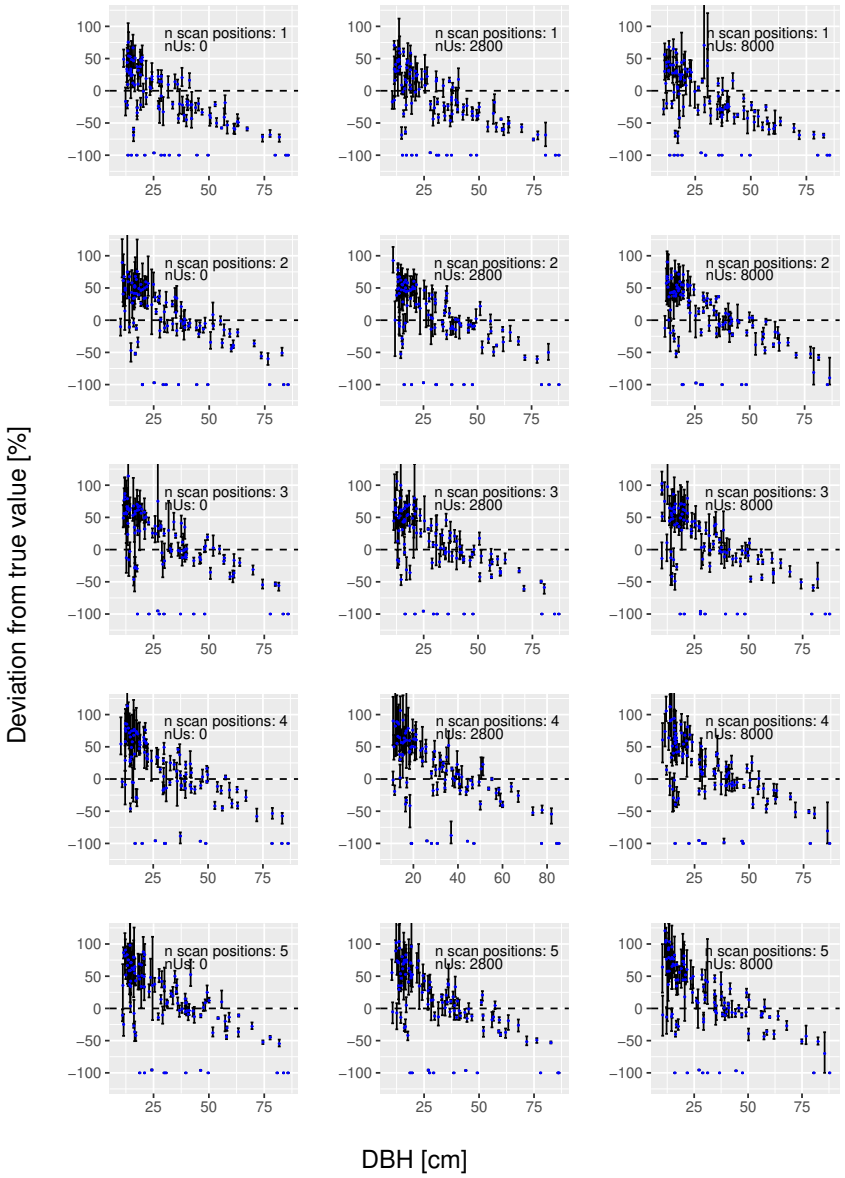

Figure S4.4: Bias of QSM in simulated forest environments with F-system scanning for small tree parts (< 7 cm diameter). The blue dots represent the mean deviations of QSM volume estimates based on tree point clouds and the whiskers represent the range of volume estimates resulting from the use of different QSM starting parameters.

4.6 References

Abegg M, Bösch R, Schaepman ME, Morsdorf F (2019) Impact of beam diameter and scanning approach on point cloud quality of terrestrial laser scanning in forests. *IEEE Transactions on Geoscience and Remote Sensing*, **(in Review)**.

Abegg M, Brändli UB, Cioldi F, *et al.* (2014) Viertes schweizerisches landesforstinventar - ergebnistabellen und karten im internet zum lfi 2009-2013 (lfi4b).

Abegg M, Kükenbrink D, Zell J, Schaepman ME, Morsdorf F (2017) Terrestrial laser scanning for forest inventories - tree diameter distribution and scanner location impact on occlusion. *Forests*, **8**, 1 – 29.

Bézier P (1977) *Essai de définition numérique des courbes et des surfaces expérimentales : contributions à l'étude des propriétés des courbes et des surfaces paramétriques polynominales à coefficients vectoriels*. Paris, Univ. Pièrre et Marie Curie.

Binney J, Sukhatme GS (2009) 3d tree reconstruction from laser range data. In: *Robotics and Automation, ICRA'09 IEEE international Conference*. Kobe, Japan.

Blender Online Community (2015) *Blender - a 3D modelling and rendering package*. Blender Foundation, Blender Institute, Amsterdam.

Brassel P, Lischke H (2001) *Swiss National Forest Inventory: Methods and Models of the Second Assessment*. WSL Swiss Federal Research Institute, Birmensdorf, Switzerland.

Brede B, Calders K, Lau A, Raumonen P, Bartholomeus H, Herold M, Kooistra L (2019) Non-destructive tree volume estimation through quantitative structure modelling: Comparing uav laser scanning with terrestrial lidar. *Remote Sensing of Environment*, **233**.

Bremer M, Rutzinger M, Wichmann V (2013) Derivation of tree skeleton and error assessment using lidar point cloud data of varying quality. *ISPRS Journal of Photogrammetry and Remote Sensing*, **80**, 39 – 50.

Calders K, Newnham G, Burt A, *et al.* (2015) Nondestructive estimates of above-ground biomass using terrestrial laser scanning. *Methods in Ecology and Evolution*, **6**, 198 – 208.

Chave J, Réjou-Méchain M, Búrquez A, *et al.* (2014) Improved allometric models to estimate the aboveground biomass of tropical trees. *Global Change Biology*, **20**.

Disney M, Kalogirou V, Lewis P, Prieto-Blanco A, Hancock S, Pfeifer M (2010) Simulating the impact of discrete-return lidar system and survey characteristics over young conifer and broadleaf forests. *Remote Sensing of Environment*, **114**, 1546 – 1560.

Disney M, Lewis P, Raumonen P (2012) Testing a new vegetation structure retrieval algorithm from terrestrial lidar scanner data using 3d models. In: *Silvilaser 2012*, SL2012-049. Vancouver, Canada.

FOREST EUROPE (2015) *State of Europe's Forests 2015*. FOREST EUROPE.

Gastellu-Etchegorry JP, Yin T, Lauret N, *et al.* (2015) Discrete anisotropic radiative transfer (dart 5) for modeling airborne and satellite spectroradiometer and lidar acquisitions of natural and urban landscapes. *Remote Sensing*, **7**, 1667–1701.

Gschwandtner M, Kwitt R, Uhl A, Pre W (2011) Blensor: Blender sensor simulation toolbox. In: *Advances in Visual Computing: 7th International Symposium (ISVC 2011)*, vol. Volume 6939/2011 (eds. Bebis R, Boyle B, Parvin D, Koracin R, Chung, Hammoud R), pp. 199 – 208. Springer Verlag, Las Vegas, USA.

Keller M (2011) *Swiss National Forest Inventory. Manual of the Field Survey 2004 - 2007*. Swiss Federal Research Institute WSL, Birmensdorf, Switzerland.

Kukko A, Hyyppä J (2007) Laser scanner simulator for system analysis and algorithm development: A case with forest measurements. In: *Laser Scanning 2007 and SilviLaser 2007*.

Lau A, Christopher M, Batholomeus H, *et al.* (2019) Estimating architecture-based metabolic scaling exponents of tropical trees using terrestrial lidar and 3d modelling. *Forest Ecology and Management*, **439**, 132 – 145.

Lewis P (1999) Three-dimensional plant modelling for remote sensing simulation studies using the botanical plant modelling system. *Agronomie*, **19**, 185 – 210.

Liang X, Kankare V, Hyyppä J, *et al.* (2016) Terrestrial laser scanning in forest inventories. *ISPRS Journal of Photogrammetry and Remote Sensing*, **115**, 63 – 77.

Lovell J, Jupp D, Newnham G, Coops N, Culvenor D (2005) Simulation study for finding optimal lidar acquisition parameters for forest height retrieval. *Forest Ecology and Management*, **214**, 398 – 412.

MacDicken K, Jonsson O, Piña L, *et al.* (2016) *Global Forest Resources Assessment 2015: How are the world's forests changing?* Food and Agriculture Organistation of the United Nations (FAO), Roma, Italy.

Morsdorf F, Nichol C, Malthus T, Woodhouse IH (2009) Assessing forest structural and physiological information contentof multi-spectral lidar waveforms by radiative transfermodelling. *Remote Sensing of Environment*, **113**, 2152 – 2163.

Pan Y, Birdsey RA, Fang J, *et al.* (2011) A large and persistent carbon sink in the world's forests. *Science*, **333**, 988 – 993.

Pitkänen TP, Raumonen P, Kangas A (2019) Measuring stem diameter with tls in boreal forests by complementary fitting procedure. *ISPRS Journal of Photogrammetry and Remote Sensing*, **147**, 294 – 306.

R Core Team (2017) *R: A Language and Environment for Statistical Computing*. R Foundation for Statistical Computing, Vienna, Austria.

Raumonen P, Kaasalainen M, Akerblom M, *et al.* (2013) Fast automatic precision tree models from terrestrial laser scanner data. *Remote Sensing*, **5**, 491–520.

Raumonen P, Kaasalainen S, Kaasalainen M, Kaartinen H (2011) Approximation of volume and branch size distribution of trees from laser scanner data. In: *ISPRS Workshop Laser Scanning 2011*, vol. XXXVIII-5/W12 of *International Archives of the Photogrammetry, Remote Sensing and Spatial Information Sciences*, pp. 79–84. Calgary, Canada.

Saarinen N, Kankare V, Vastaranta M, *et al.* (2017) Feasibility of terrestrial laser scanning for collecting stem volume information from single trees. *ISPRS Journal of Photogrammetry and Remote Sensing*, **123**, 140 – 158.

Trochta J, Kral K, Janik D, Adam D (2013) Arrangement of terrestrial laser scanner positions for area-wide stem mapping of natural forests. *Canadian Journal of Forest Research*, **43**, 355 – 363.

Van der Zande D, Hoet W, Jonckheere I, van Aardt J, Coppin P (2006) Influence of measurement set-up of ground-based lidar for derivation of tree structure. *Agricultural and Forest Meteorology*, **141**, 147 – 160.

Van der Zande D, Jonckheere I, Stuckens J, Verstraeten WW, Coppin P (2008) Sampling design of ground-based lidar measurements of forest canopy structure and its effect on shadowing. *Canadian Journal of Remote Sensing*, **34**, 526 – 538.

Watt PJ, Donoghue DNM (2005) Measuring forest structure with terrestrial laser scanning. *International Journal of Remote Sensing*, **26**, 1437 – 1446.

Weber J, Penn J (1995) Creation and rendering of realistic trees. In: *SIGGRAPH '95 Proceedings of the 22nd annual conference on Computer graphics and interactive techniques*, pp. 119 – 128.

Wezyk P, Koziol K, Glista M, Pierzchalski M (2007) Terrestrial laser scanning versus traditional forest inventory. first result from the polish forests. In: *ISPRS Workshop on Laser Scanning 2007 and SilviLaser 2007*, pp. 424 – 429.

Yang X, Strahler AH, Schaaf CB, *et al.* (2013) Three-dimensional forest reconstruction and structural parameter retrievals using a terrestrial full-waveform lidar instrument (echidna). *Remote Sensing of Environment*, **135**, 36 – 51.

Zhang C, Chen T (2001) Efficient feature extraction for 2d/3d objects in mesh representation. *Proceedings 2001 International Conference on Image Processing*.

Chapter

5

Synthesis

Forest inventories rely on representative and bias-free data on forests. To date, there is no method to efficiently measure accurate tree volume on sample plots. Terrestrial laser scanning has the potential to close this gap. However, detailed understanding of scanning setups, point cloud evaluation approaches, TLS device and stand properties is needed before an integration of TLS for forest inventories, to ensure accurate (bias free) and precise (low variation) estimates on tree volume.

In this chapter, we provide a thorough overview and discussion of our findings, general contributions to the research field and suggestions for future research, bringing us one step closer to an application of terrestrial laser scanning for forest inventories.

5.1 Main findings

The thesis is structured by three main research questions (RQ) formulated in chapter 3.1 and addressed in chapters 2 to 4:

> I. How do the properties of a forest stand, the placement of the laser scanner and the combination of scanner placements influence the technically unblocked observable area of a sample plot?
>
> II. How do laser scanners handle echoes from multiple objects and what is the influence of such echo-handling (signal triggering) in combination with the laser beam diameter and the (scanned) object size on the quality of the point cloud?
>
> III. What can we learn from the implementation of a simulation environment for TLS applications for forest inventories in terms of the influence of scanner placement and understorey density on the quality of tree volume estimation from point clouds?

In the following three subsections, the main findings of the three research questions are presented and discussed.

5.1.1 How do the properties of a forest stand, the placement of the laser scanner and the combination of scanner placements influence the technically unblocked observable area of a sample plot?

Many authors state (e.g. Morsdorf *et al.*, 2018; Saarinen *et al.*, 2017; Wilkes *et al.*, 2017; Liang *et al.*, 2016; Calders *et al.*, 2015) that terrestrial laser scanning has the potential to complement traditional measurement approaches for forest inventories. However, occlusion is one of the key factors that limits the potential of TLS (Watt & Donoghue, 2005; Trochta *et al.*, 2013; Van der Zande *et al.*, 2006). Occlusion is caused by objects shadowing each other, so that parts of the objects of interest are not visible to the TLS device. The effect of occlusion is usually mitigated by combining TLS scans from different locations (Hilker *et al.*, 2012; Ehbrecht *et al.*, 2016). However, for a possible applications of TLS in forest inventories, the methods need to have a proven high performance in a larger range of forest stand conditions. The decision maker of a forest inventory needs a fundamental understanding of the influencing factors regarding the quality of the point clouds generated by TLS and possible constraints on operational applications. The analysis of visibility can contribute to quantifying the expected quality of TLS acquisitions in terms of completeness.
We derived 2740 stand parameters from Swiss national forest inventory sample plots. Based on these parameters, we defined virtual scenes of forest plots with the software Blender. Using Blender's ray-tracing features, we assessed the 2D visibility properties for each of the virtual plots with different scanner placement schemes. We showed that the number of trees has the strongest influence on visibility on a sample plot, in addition with the Weibull shape parameter describing a stand and the mean diameter of the dominant 100 trees per hectare. Furthermore, we showed the effectiveness and the efficiency of 40 scanner location patterns, disentangling the influence of scanner location and the number of combined scanning positions on a square sample plot with edge length of 50 m. Scanner location in the centre of the sample plot provide a better visual coverage of the sample plot. Furthermore, additional scanner locations improve the visibility. However, we constated a saturation effect, mitigating the additional gain in visibility with each additional scanning location. Patterns with a regular distribution of the scanner location within the sample plot, with equal distance to each other and the sample plot edge perform the best. Slight movements of scanner locations however do not worsen the visibility notably.
The reason for the lower visibility performance of scanners, located at the edge of the sample plot, is the longer travelling distance of a laser pulse through the sample plot. Long travelling distances increase the probability of a laser pulse to be intercepted by a tree, occluding parts of the sample plot behind the tree. If the scanner is moved only slightly, the influence of the surrounding trees is probably higher than the effect of the longer travelling distance of a laser pulse on the sample plot.
The simulations are performed with geometric scanning with an infinitesimally small laser beam and a very high angular resolution. Especially when small objects are

scanned with an inappropriate angular resolution, a fraction of these objects would theoretically be invisible for the laser scanner. Additionally, laser pulses intersecting small objects, often intersect with additional objects due to the diameter of the laser beam. This might lead to noise effects in point clouds. On real sample plots, additional effects might interfere with visibility, such as a rough terrain. Moreover effects due to a different positional distribution of the stems on the sample plot, instead of Poisson-distribution, might lead do different results. However, with the number of simulated sample plots a wide range of possible tree distributions are covered.
The main finding on the first research question is, that for best visibility on a sample plot the scanner locations should be placed regularly on the sample plot with equal distances to each other and the sample plot edge.

5.1.2 How do laser scanners handle echoes from multiple objects and what is the influence of such echo-handling (signal triggering) in combination with the laser beam diameter and the (scanned) object size on the quality of the point cloud?

In recent years, portable laser scanning devices and their applications in the context of forest inventories were subject to rapid methodological and technological developments. Devices have become smaller, lighter and more affordable, whereas new data-driven methods and software packages facilitate the derivation of information from the point clouds. Thus, terrestrial laser scanning (TLS) is now well established and laser - object interactions have been studied using theoretical-, modelling- and experimental approaches. Still, little is known on the influence of TLS scan and survey properties on point clouds in complex scattering environments such as forests. However, the representation of scanned objects in terms of accuracy and completeness is a key factor for successful feature extraction.
We analysed three state-of-the-art terrestrial laser scanners in terms of effects when their laser beams intersect with multiple objects along range. We described the observed signal triggering effects mathematically for each device and generalised them to handle laser pulse intersections with multiple objects. We use the results of the analysis for a simulation study to investigate the effects of laser beam diameter and signal triggering on point cloud quality when scanning in forest environments. For this purpose, we used the same simulated stands with 684 diameter distributions described by Weibull-distributions based on NFI sample plots (see chapter 2).
The lab experiments displayed two effects of deviation of scan points from an object's surface, one perpendicular, the other parallel to the laser beam. The perpendicular deviation is an effect of multiple signal triggering, which produces points along the central axis of the laser beam. Thus, if a beam touches an object at its edge, the point's possible distance to the object is directly dependent on the diameter of the laser. Concerning the distance deviation parallel to the laser beam, it appears that

the phase-shift system (Faro) performs differently compared to time-of-flight systems (Riegl and Leica). The phase-shift system struggles with ambiguity problems due to the combination of intensity modulations in the laser beam to measure a range. Therefore, depending on the distance of the scanned obstacles to each other, it can either remove points that are clearly problematic (prefiltering) or display a distance deviation which is sinusoidally weighted by the distance between the obstacles. In any case, some ambiguities cannot be resolved and produce severe distance deviations. It seems that time-of-flight systems do not struggle with this kind of problem, due to their ability to evaluate the whole reflected laser energy pattern over time. Furthermore, for a scanning device, there is no way of perfectly resolving all types of objects of any shape, since one object with an inclined surface may reflect the same light pattern as two separate objects. There are only two available options, either to prefilter or provide some kind of average distance to the objects. The Riegl and Faro scanners do not separate obstacles that are close to each other, while the Leica scanner solves the problem by prefiltering these points.

The simulation study shows the limitations in depicting small objects precisely in a point cloud. Either they are not visible or have only very few points due to their size. Especially, when a scanner prefilters the point cloud, almost no points are left on small objects. It appears that triggering multiple signals alleviates this effect. However, the points are at a certain distance from the object surface which can lead to erroneous object reconstructions. Another effect that can be observed, is that objects appear flattened in the point cloud with increasing beam diameters. This effect is due to the laser beam working like a moving window, averaging the ranges measured within its footprint.

The signal triggering of laser scanning systems is influenced by many factors, such as the object shape, its surface, the reflectance of the object, the constellation of multiple objects, and even the atmospheric conditions play a role. In addition, the scanner settings (adjustable or not) have an influence on the point cloud. However, reverse-engineering signal-triggering functionalities without any detailed manufacturer's information on the devices, is a huge effort. Nevertheless, we were able to cover some important effects observed in point clouds.

The effects observed with the two-obstacle lab setting had to be generalised for cases when a laser pulse hits more than two objects. Hence, the effects, caused by such settings, most likely do not match reality exactly. Prefiltering effects are assumed to be reproduced in a realistic way, and surely provide realistic implications for the effects of prefiltering. The primary objective of the simulation study was not to reproduce exactly the same scanning results of the three devices investigated, but to allow general conclusions to be drawn, regarding the effects of different signal triggering approaches. Nevertheless, the effect of the laser beam size is based on realistic assumptions, since the effect of its size is precisely reproducible.

There are various effects that could additionally be implemented in the simulation approach used in this study, such as considering the intensity of the reflected light,

multiple reflectance of the photons of the laser pulse or errors in the range measurement of the different devices.
An important finding of the present study for forest inventory applications is that small objects lack appropriate representation in point clouds of the signal triggering approaches investigated in this study, in that either points are prefiltered or subject to a deviation from the object's surface. Information on small objects deteriorates even more with increasing distance to the scanner, especially in environments with a high density of objects. This implies that scanning small branches (e.g., less than 2 cm in diameter) in tree crowns (large distance to the scanner) with plenty of small branches (high density) will be nearly impossible when tree crown reconstruction is the objective of the application. In such a situation, scanners with small laser beam diameters perform slightly better. On the other hand, larger laser beam diameters, especially in combination with multiple triggering, deliver more points per object. In addition to these technical limitations, even slight wind would add further noise to the point cloud. Larger branch diameters (e.g., up to 6 cm) are also difficult to represent, depending on the application. Another problem occurring with large laser beam diameters is that the object shape tends to be flattened. This could lead to a bias in diameter estimation when applying the widely used Hough transform (e.g., Simonse *et al.*, 2003; Hough, 1962; Bienert *et al.*, 2007; Heinzel & Huber, 2017) approach to fit circles or cylinders in the point cloud.

5.1.3 What can we learn from the implementation of a simulation environment for TLS applications for forest inventories in terms of the influence of scanner placement and understorey density on the quality of tree volume estimation from point clouds?

National forest inventories are an established process to monitor forest development, delivering information on forests ecosystem services, such as wood availability or forest carbon balance. Even though, tree volume can not be measured directly with conventional tools, it is one of the most important variables for NFIs. As stated by many authors (e.g., Morsdorf *et al.*, 2018; Calders *et al.*, 2015; Wilkes *et al.*, 2017), terrestrial laser scanning has the potential to directly measure tree volume. However, an application for forest inventories needs profound understanding of precision and accuracy of tools and models used. A wide variety of possible TLS applications in forest inventories can be tested with the presented simulation environment. The advantage of simulation is the availability of a perfect "ground truth", i.e. the volume of the used tree models is exactly known. The simulations show, that the scanning system has an influence on the volume estimation of the tree models. Furthermore, we could observe a bias in all volume estimates, which seems to be related to the tree size and the size of the estimated tree part. Raumonen *et al.* (2013) already describe this effect when introducing their approach (treeQSM), whereas Calders *et al.* (2015) observe this effect when comparing the volume estimations to destructively sampled

trees. Possibly, an overestimation originates from an overestimation of small tree parts in cases of low occlusion. In large trees, which have more occluded parts, e.g., due to large branches, small tree parts are underestimated. Additionally, Disney *et al.* (2012) or Calders *et al.* (2015) discuss the variation in the volume estimation which is dependent on the starting parameters of the treeQSM approach, which is observed in the simulated data as well.

For this study, we chose an easy parametrisable tree model for a Blender application. Even though the tree model used for this thesis can be parametrised to a wide range of tree properties, such as branch level, branch angle and diameter, it can only place branches in a helical way on a parent branch/stem. This structure is encountered in real trees as well (alternate branching), but does not cover all existing branching structures (e.g., opposite branching, whorled branching). On the other hand, treeQSM is designed to estimate the volume (and other tree parameters) of any kind of tree like structure, without constraints on a specific structure. Hence, we assume the findings concerning limitations of volume estimation with TLS to be realistic.

The estimates of merchantable wood (diameter $\geq$ 7 cm) are considerably more precise (less variation) than the volume estimates of tree parts with small diameters (small branches and tree top). This finding is supported by the findings in chapter 3. The reason is, that small diameters often lack a sufficient representation in the point cloud due to the angular resolution of the scanner and, in trees, are often situated in a distance to the scanner and a high density of objects (e.g., in the tree crown). Furthermore noise effects increase when scanning small objects due to the high occurrence of edge effects, i.e. a laser pulse intersecting with multiple objects and therefore possibly producing points not lying on an object surface.

In this study, we could not observe an effect of understorey on the quality of the volume estimation from TLS point clouds, even with high densities of 8000 sapling trees per hectare. However, the number of failed volume estimations is slightly higher with understorey. The possible influence of understorey for the applied TLS system (in this case a Faro 3D like signal triggering) is either occlusion, prefiltering, small distance deviation (some centimetres) on objects edges, or large distance deviation of the triggered laser echoes due to the laser beam intersecting multiple objects with nearly the same amount of energy. Since the setup of the forest scenes in this study was designed to enable an automatic clipping of the tree point clouds from the rest of the scene (i.e. clear separation of shrub layer and tree crowns), noise points with large distance deviation were mostly clipped from the tree point cloud. Therefore a part of the distance noise could not interfere with the treeQSM for the volume estimation. The effect of occlusion and prefiltering (removing points based on ambiguous distance measurements) due to understorey on the other hand, was not strong enough to reduce the quality of volume estimation systematically, especially when point clouds from multiple scanner locations were combined. However, real forest environments might consist of coniferous understorey or scanning is performed during vegetation period which would lead to considerably stronger occlusion effects.

The combination of point clouds from multiple scanning locations has a favourable effect on the bias of the volume estimations, especially for larger trees. However, the variability in the volume estimations is increased with an increasing number of combined scanning locations. The higher variability is due to the simulated laser echo triggering system (F-system). Since the F-system has a slight distance deviation at objects' edges, every additional scanning perspective adds noise according to the respective scanning direction to the object. This effect is also described by Binney & Sukhatme (2009) and observed by every TLS practitioner. This additional noise in interaction with the treeQSM parameters influences the outcome of the volume estimation. Furthermore, additional points from different scanner locations increase the density of noise, which consequently could be processed as proper points from objects instead of being filtered by the treeQSM algorithm.

The simulated scanning system (F-system) is based on laboratory experiments investigating the behaviour of TLS scanners when scanning edges of objects (Abegg *et al.*, 2019). However, under real conditions there are many more factors leading to noise effects in the point cloud, e.g., movement of the scanned trees or more complex "mixed pixel" situations than tested in the laboratory. We assume, in comparison with point clouds from real forest scenes, retrieved with a Faro 3D scanner, that the simulated point cloud is relatively clean. Hence noise effects of volume estimation in real forests are possibly even higher than in this study.

The tree models used in this study do not represent existing trees, but a deciduous tree like structure without leaves. An application of TLS for forest inventories has to handle coniferous trees as well and branching structure might be different (more dense than the 4 branching levels of this study). Additionally the stand structure, e.g., in Switzerland, is far more complex and not just single, respectively double layered as in this study with a tree layer and a understorey layer. Nevertheless, we assume occlusion effects and noise effects influencing the performance of treeQSM in volume estimation are very similar to those in reality. The weakness of TLS applications observed here, are possibly even stronger, when applying TLS in a forest inventory.

Taking into account the paramount importance of bias free estimates for a forest inventory, there are still pending questions concerning an application of TLS in volume estimation for forest inventories. In future, explanations for biased volume estimations must be identified, using simulations and destructive sampling, so that the favours of TLS can be of use for forest inventories.

5.2 General contributions

Literature on terrestrial laser scanning reveals a wealth of methods and approaches to measure tree or forest features, such as tree volume (e.g. Raumonen *et al.*, 2013; Hackenberg *et al.*, 2014), stand structural parameters (e.g. Côté *et al.*, 2011; Ehbrecht *et al.*, 2016), tree species (Akerblom *et al.*, 2017), tree microhabitats (Rehush *et al.*, 2018) and many more. Some authors even describe methods pointing to a possible application TLS for forest inventories (e.g. Bienert *et al.*, 2006; Aijazi *et al.*, 2017). However, up to now there is no country retrieving forest information from TLS campaigns on a regular basis. As pointed out in section 1.4, it is crucial for an NFI to rely on unbiased measurements. Therefore, thorough evaluation of new procedures is highly important.

5.2.1 Simulation of terrestrial laser scanning

In chapter 2, we introduce an approach based on Blender (Blender Online Community, 2015; Gschwandtner *et al.*, 2011) that is able to simulate geometric rays to evaluate visibility and TLS coverage in a virtual 3D environment. In chapter 3, we describe an adaptation of the LiDAR simulation code of Gschwandtner *et al.* (2011) enabling it to simulate LiDAR pulses with a specific diameter, beam divergence and signal triggering approach, based on laboratory experiments with three state-of-the-art TLS devices. In chapter 4, we introduce a workflow to simulate TLS measurements in forest stands with dense understorey.

Even though the presented TLS simulation environment is an abstraction of real laser scanners and of real forest stands, it helps to understand the interaction of TLS device and scanned objects in different environments. We assume that certain effects, e.g., due to occlusion or laser beam diameter, can be simulated in a realistic way. The implemented signal triggering approaches, even though based on observations from real scanners, do not exactly behave like actual scanners which are influenced by many additional factors. Nevertheless, these implemented signal triggering approaches have clear properties, which are understood (and occur in real scanner as well).

Hence, simulation will help to understand the impact of such differences in signal triggering approaches on assessed forest features. These approaches can be compared with each other in exactly the same situations. Furthermore, the forest features based on 3D models (e.g., trees or leaves) used in the simulation are usually exactly known, unlike a “ground truth” based on measurements in a real forest, which are always subject to measuring errors as well. Consequently, evaluations comparing the known (true) properties with such derived from simulated point clouds are straight forward. Even more, error sources in a TLS-to-forest-feature-workflow can

be easily switched on or off, e.g., in a workflow, as described in chapter 4 to estimate tree volume, a virtual tree could be scanned without noise (geometric scan) from any perspective (from below or above the tree), delivering a perfect point cloud of a tree, which is assessed by a QSM. Thus, possible error sources, inherent to the QSM model, can be detected. Similarly, different point cloud processing approaches targeting the same forest feature can be compared directly in a benchmarking process, similar to the RAMI exercise for airborne LiDAR (Widlowski *et al.*, 2007). We recommend to evaluate new TLS derived forest features within a simulation environment if possible. This would at least allow finding suitable scanner settings (e.g., angular resolution, scanner placement) before going to the field. Furthermore, new approaches for feature extraction from point clouds could be evaluated with a simulation environment, as demonstrated in this thesis. Even more, due to Blenders wide range of modelling tools, the 3D scenes as presented here, could be adapted, e.g., to simulate inclined or uneven terrain.

5.2.2 Limitations in object size

The simulation experiments disclosed several limitations of terrestrial laser scanning. The most important finding is that size (of the object of interest) matters. Chapter 2 discusses, that small objects in a certain distance to the scanner might be invisible, due to the scanners angular resolution, leading to objects possibly lying between two laser pulses. A simple model to calculate the number of "hits" on an object is provided. In chapter 3, we demonstrated with a simulation of different signal triggering approaches and laser beam diameters that the smaller the objects, the less they are visible in a forest environment, especially in dense stands. Furthermore, even if they are intersected by laser pulses, the number of hits usually is very small. This could lead to problems when a geometric reconstruction is targeted. In chapter 4, we demonstrate that volume estimation of tree parts with diameter < 7 cm, scanned in a 3D forest environment, are subject to high variation and bias.

5.2.3 Scanner placement

The analysis of scanner placement on a sample plot, as in chapter 2, indicates that each additional TLS scan enhances visibility on the sample plot. If the scanner locations are regularly distributed within the sample plot, an optimal visibility is reached. However, as we discovered in chapter 4, additional scans not necessarily lead to better results. The findings of that chapter indicate that there are unwanted effects, due to edge noise effects, leading to higher variability in the volume estimation with the tested QSM approach. Hence, scanner placement has to be evaluated deliberately concerning the targeted variable and the used point cloud evaluation approaches

(such as point cloud filtering, segmentation or QSM).

5.2.4 Tree volume estimation with TLS

If volume estimates of tree stem and large branches ($\geq$ 7 cm in diameter) is targeted, the simulations show that the QSM delivers biased estimates. Nevertheless, the relative bias is dependent on the DBH of the tree, with a high relative overestimation in small trees and a small overestimation in large trees. Furthermore, the volume of small tree parts ($<$ 7 cm diameter) is strongly overestimated (+ 50%) in small trees and underestimated (-50%) in large trees. These results point to a possible source of bias in the estimation of small tree parts, since their ratio is higher in small trees than in large trees. A direct comparison of the tree model and the QSM output shows that cylinders fitted on small branches are mostly too large possibly due to the small number of points representing the branch shape, leading to problems in fitting cylinders properly, and overestimating the actual branch diameter. The underestimation of small branches in large trees, compensating the overestimation to a certain extent, are due to gaps in the point cloud from occlusion. The variation in the estimates are due to the starting parameters of the QSM model, mastering shortcomings of the point cloud more or less successful. For an NFI point of view it is crucial to understand the actual source of the error (bias) and to know the extent of it. The latter could be compared to the errors inherent to the currently used allometric models, which allow decisions on a TLS implementation in the NFI framework.

5.3 Final considerations and future directions

The findings in the framework of this thesis help to understand details of TLS applications for forest inventories. TLS still seems a promising technology to enhance traditional forest inventory methods. However, the thesis points to further knowledge gaps not yet investigated. In the following sections, certain open issues and potential future directions are discussed.

5.3.1 Open issues

Our evaluations show that there is no simple rule on how to apply TLS for tree volume estimation in an NFI, there is not a unique scanner setup or TLS device to be used. An actual application has to be evaluated deliberately, considering the objectives of the measurements. Open questions for a TLS application in NFIs are: What is an optimal scanning density of trees, chosen for a volume measurement (number of scans, scanner location, angular resolution of the scan)? Which laser scanner is

suitable to achieve the objectives of the volume estimations most efficiently? Which might be the appropriate QSM approach for volume estimation? What would be a suitable workflows for TLS application in an NFI (scanner setup, tree type, object size to be measured, TLS device, tree segmentation algorithm, QSM approach)? And finally, how can we handle bias emerging from such a scanning workflow?
Beyond these questions for an upcoming TLS implementation, a simulation environment can play an important role for long-term monitoring issues with TLS, such as changing devices. Consistent long-term time series of data on forest is one key aspect that makes NFI data specifically valuable. Unlike measuring tapes and calliper, TSL devices will undergo further development in the future. Considering recent development in TLS and keeping in mind that the Swiss NFI has a measuring cycle of 9 years, we expect significant changes TLS technology within every measuring cycle. Such technological changes usually lead to a change in newly acquired TLS data. Hence, causes and effects due to "improved" scanner generations or new devices and scan settings must be understood in detail to allow bridge building between data sets from different points in time, sustaining a time-series character in TLS data. Simulation environments, such as the presented in this thesis, can serve as a basis to such a bridge building, allowing the direct comparison of "old" and "new" TLS data. For this purpose, nearly all effects leading to noise in TLS data should be infered from laboratory experiments and implemented in a simulation environment. Additionally more realistic forest scenes could be generated, to compare the technological differences. Nevertheless, the implementation of perfect simulations is impossible, which does not prevent project leaders from considerations on expenses (for lab tests and implementation) and benefit (confidence in time series, derivation of change estimates based on TLS data).

5.3.2 Integration of TLS in NFI tree volume estimation

As demonstrated by many authors (e.g., Raumonen *et al.*, 2013; Hackenberg *et al.*, 2014; Côté *et al.*, 2011) TLS is capable of delivering unprecedented information on trees. However, handling biased predictions, as indicated in chapters 3.1 and 4, poses the major challenge, towards an introduction of TLS for forest inventories. Therefore, we need to find a way to either produce a perfect tree volume estimation with appropriate laser scanners and QSMs (still to be found) or we improve our understanding of the emergence of bias.
Nevertheless, bias is inherent in every model, also in the allometric models to predict tree volume, as currently used in today's NFIs. However, if such models are fitted with completely representative data, we can assume estimates for the represented area are unbiased as well. If that is not possible, the origin of bias has to be understood, at least up to a tolerable level for the NFI.
The models currently used in NFIs are often fitted on large series of measurements, comprising of several tens of thousands of trees, originating from times, when human

labour was less expensive. Even though, these measurements are spread all over the country area of Switzerland, they are not completely representative and hence possibly subject to a small but existing bias. Large scale destructive sampling is nowadays not realisable any more, due to financial restrictions. Hence, the emergence of bias from TLS tree volume estimation has to be understood in detail, enabling TLS as standard tool for tree volume estimation. Possible sources of bias are most likely interactions of laser scanner, tree segmentation algorithms, point cloud filtering approaches and applied QSM. Therefore, future simulation experiments should aim at understanding these interactions.

The portrayed simulation workflow in chapter 4 has the potential to allow thorough testing of tree volume estimation with TLS in various forest environments. However, in that study only a few variations in the workflow were tested, namely the scanner placement, one signal triggering approach compared with geometric scanning, relatively homogeneous stands with deciduous trees and three understorey densities and one QSM approach.

As for the scanner placement, we see no further need for changes, which allows the comparison of five different scanner placement settings. Whereas, in a future study, all available signal triggering approaches, including distance measurement uncertainties, should be investigated. Additionally, other available QSM approaches could be tested, e.g., as presented by Hackenberg *et al.* (2014). Furthermore, tree shapes can be varied to a coniferous tree appearance with added needle like objects. This would deliver more realistic forest environments with higher occlusion, as encountered in real forests. From the findings in chapter 4, we concluded that the diameter of tree parts have an influence on the bias of the QSM volume estimation. Therefore, additional diameter thresholds should be implemented in the simulation to allow separate analysis for different tree parts.

Furthermore, as indicated in section 5.2.1 the QSMs could be tested on a perfect point cloud, generated from completely covered tree models with multiple geometric scanning. Such tests allow further visual inspections in an overlay of the derived cylinder model from the QSM and the point cloud, pointing to possible sources of QSM errors.

Another direction of integrating TLS in a forest inventory is the usage of information delivered by TLS e.g., for an evolved generation of allometric models. They might allow the integration of high quality information in the models, such as volume of variable parts of the trees, such as the visible part by TLS, enabling more precise predictions of tree features on the sample plot.

Such further experiments will help to decide on suitable scanning protocols and allow the selection of the most satisfactory point cloud processing procedures and not least support decision-making on sampling design, e.g., sampling on a sub-grid and/or sampling a sub-sample of the tally trees in a two stage approach (see section 1.1). But either way or the other, certain destructive sampling of real trees is probably

needed to proof the applicability of TLS tree volume estimation in an NFI.

5.4 References

Abegg M, Bösch R, Schaepman ME, Morsdorf F (2019) Impact of beam diameter and scanning approach on point cloud quality of terrestrial laser scanning in forests. *IEEE Transactions on Geoscience and Remote Sensing*, **(in Review)**.

Aijazi AK, Checchi P, Malaterre L, Trassoudaine L (2017) Automatic detection and parameter estimation of trees for forest inventory applications using 3d terrestrial lidar. *remote sensing*, **9**.

Akerblom M, Raumonen P, Mäkipää R, Kaasalainen M (2017) Automatic tree species recognition with quantitative structure models. *Remote Sensing of Environment*.

Bienert A, Scheller S, Keane E, Mohan F, Nugent C (2007) Tree detection and diameter estimations by analysis of forest terrestrial laserscanner point clouds. In: *ISPRS Workshop on Laser Scanning 2007 and SilviLaser 2007*, vol. XXXVI-3/W52 of *International Archives of the Photogrammetry, Remote Sensing and Spatial Information Sciences*, pp. 50 – 55.

Bienert A, Scheller S, Keane E, Mullooly G, Mohan F (2006) Application of terrestrial laser scanners for the determination of forest inventory parameters. In: *Commission V Symposium 'Image Engineering and Vision Metrology'*, vol. XXXVI part 5 of *International Archives of the Photogrammetry, Remote Sensing and Spatial Information Sciences*, p. 5. Dresden, Germany.

Binney J, Sukhatme GS (2009) 3d tree reconstruction from laser range data. In: *Robotics and Automation, ICRA'09 IEEE international Conference*. Kobe, Japan.

Blender Online Community (2015) *Blender - a 3D modelling and rendering package*. Blender Foundation, Blender Institute, Amsterdam.

Calders K, Newnham G, Burt A, *et al.* (2015) Nondestructive estimates of above-ground biomass using terrestrial laser scanning. *Methods in Ecology and Evolution*, **6**, 198 – 208.

Côté JF, Fournier RA, Egli R (2011) An architectural model of trees to estimate forest structural attributes using terrestrial lidar. *Environmental Modelling & Software*, **26**, 761–777.

Disney M, Lewis P, Raumonen P (2012) Testing a new vegetation structure retrieval algorithm from terrestrial lidar scanner data using 3d models. In: *Silvilaser 2012*, SL2012-049. Vancouver, Canada.

Ehbrecht M, Schall J, Juchheim J, Ammer C, Seidel D (2016) Effective number of layers: A new measure for quantifying three-dimensional stand structure based on sampling with terrestrial lidar. *Forest Ecology and Management*, **380**, 212 – 223.

Gschwandtner M, Kwitt R, Uhl A, Pre W (2011) Blensor: Blender sensor simulation toolbox. In: *Advances in Visual Computing: 7th International Symposium (ISVC 2011)*, vol. Volume 6939/2011 (eds. Bebis R, Boyle B, Parvin D, Koracin R, Chung, Hammoud R), pp. 199 – 208. Springer Verlag, Las Vegas, USA.

Hackenberg J, Morhart C, Sheppard J, Spiecker H, Disney M (2014) Highly accurate tree models derived from terrestrial laser scan data: A method description. *Forests*, **5**, 1069 – 1105.

Heinzel J, Huber MO (2017) Tree stem diameter estimation from volumetric tls image data. *remote sensing*, **9**.

Hilker T, Coops NC, Culvenor DS, Newham G, Wulder MA, Bater CW, Siggins A (2012) A simple technique for co-registration of terrestrial LiDAR observations for forestry applications. *Remote Sensing Letters*, **3**, 239–247.

Hough PVC (1962) Method and means for recognizing complex patterns.

Liang X, Kankare V, Hyyppä J, *et al.* (2016) Terrestrial laser scanning in forest inventories. *ISPRS Journal of Photogrammetry and Remote Sensing*, **115**, 63 – 77.

Morsdorf F, Kükenbrink D, Schneider D, Abegg M, Schaepman ME (2018) Close-range laser scanning in forests: towards physically based semantics across scales. *Interface focus*, **8**.

Raumonen P, Kaasalainen M, Akerblom M, *et al.* (2013) Fast automatic precision tree models from terrestrial laser scanner data. *Remote Sensing*, **5**, 491–520.

Rehush N, Abegg M, Waser LT, Brändli UB (2018) Identifying tree-related microhabitats in tls point clouds using machine learning. *remote sensing*, **10**.

Saarinen N, Kankare V, Vastaranta M, *et al.* (2017) Feasibility of terrestrial laser scanning for collecting stem volume information from single trees. *ISPRS Journal of Photogrammetry and Remote Sensing*, **123**, 140 – 158.

Simonse M, Aschoff T, Spiecker H, Thies M (2003) Automatic determination of forest inventory parameters using terrestrial laser scanning. In: *Proceedings of the ScandLaser Scientific Workshop on Airborne Laser Scanning of Forests*, pp. 251–257. Umeå, Sweden.

Trochta J, Kral K, Janik D, Adam D (2013) Arrangement of terrestrial laser scanner positions for area-wide stem mapping of natural forests. *Canadian Journal of Forest Research*, **43**, 355 – 363.

Van der Zande D, Hoet W, Jonckheere I, van Aardt J, Coppin P (2006) Influence of measurement set-up of ground-based lidar for derivation of tree structure. *Agricultural and Forest Meteorology*, **141**, 147 – 160.

Watt PJ, Donoghue DNM (2005) Measuring forest structure with terrestrial laser scanning. *International Journal of Remote Sensing*, **26**, 1437 – 1446.

Widlowski JL, Taberner M, Pinty B, *et al.* (2007) Third radiation transfer model intercomparison (rami) exercise: Documenting progress in canopy reflectance models. *Journal of Geophysical Research*, **112**.

Wilkes P, Sarmiento AL, Disney M, *et al.* (2017) Data acquisition considerations for terrestrial laser scanning of forest plots. *Remote Sensing of Environment*.

Publications

Abegg, M. (2019): Coordination of the national forest inventory data analysis system. In Swiss National Forest Inventory – Methods and Models of the Fourth Assessment; Fischer, C.; Traub, B. (eds.) Managing Forest Ecosystems. *Springer, Cham. 405-415. doi: 10.1007/978-3-030-19293-8_24*

Lanz, A.; Fischer, C.; **Abegg, M.** (2019): Sampling Design and Estimation Procedures. In Swiss National Forest Inventory – Methods and Models of the Fourth Assessment; Fischer, C.; Traub, B. (eds.) Managing Forest Ecosystems. *Springer, Cham. 39-92. doi: 10.1007/978-3-030-19293-8_2*

Steidiger, B. S.; Crowther, T. W.; Liang, J.; Van Nuland, M. E.; Werner, G. D. A; Reich, P. B.; Nabuurs, G.; de-Miguel, S.; Zhou, M.; Picard, N.; Herault, B.; Zhao, X.; Zhang, C.; Routh, D.; **Abegg, M.**; . . . Peay, K. G. (2019): Climatic controls of decomposition drive the global biogeography of forest-tree symbioses. *Nature. 569: 404 - 408. doi: 10.1038/s41586-019-1128-0*

Morsdorf, F., Kükenbrink, D., Schneider, F.D., **Abegg, M.**, & Schaepman, M.E. (2018). Close-range laser scanning in forests - towards physical-based semantics across scales. *Interface Focus 8 (2), 1-10. doi: 10.1098/rsfs.2017.0046*

Rehush, N.; **Abegg, M.**; Waser, L. T.; Brändli, U.-B. (2018): Identifying tree-related microhabitats in TLS point clouds using machine learning. *Remote Sensing 10 (1735). doi: 10.3390/rs10111735*

Feil, F.; **Abegg, M.**; Abegg, M. (2018): Timing of concurrent visual stimuli determines modulation of saccadic amplitude. *Journal of Vision. Vol. 18(11): 8. doi: 10.1167/18.11.8*

*__Abegg, M.__, Kükenbrink, D., Zell, J., Schaepman, M.E., & Morsdorf, F. (2017). Terrestrial laser scanning for forest inventories-tree diameter distribution and scanner location impact on occlusion. *Forests 8, 1-29. doi: 10.3390/f8060184*

Lanz, A.; **Abegg, M.**; Brändli, U.-B.; Camin, P.; Cioldi, F.; Ginzler, C.; Fischer, C. (2016) Switzerland. [Chap. 43] In: Vidal, C.; Alberdi, I.; Hernández, L.; Redmond, J. (eds.) National forest inventories. Assessment of wood availability and use. *Springer, Cham. 783-805*.

Etzold, S.; Wunder, J.; Braun, S.; Rohner, B.; Bigler, Ch.; **Abegg, M.**; Rigling, A. (2016): Mortalität von Waldbäumen: Ursache und Trends. In: Pluess, A. R.; Augustin, S.; Brang, P. (eds.), Wald im Klimawandel. Grundlagen für Adaptionsstrategien. *Bundesamt für Umwelt BAFU, Bern; Eidg. Forschungsanstalt WSL, Birmensdorf; Haupt, Bern, Stuttgart, Wien. 177-198*.

Zellweger, F; Braunisch, V.; Morsdorf, F.; Baltensweiler, A.; **Abegg, M.**; Roth, T.; Bugmann, H.; Bollmann, K. (2015): Disentangling the effects of climate, topography, soil and vegetation on stand-scale species richness in temperate forests. *Forest Ecology and Management. doi: 10.1016/j.foreco.2015.04.008*

Articles to be published

* **Abegg, M.**, Bösch, R., Schaepman M.E., & Morsdorf F. (under Review). Tree volume estimation with terrestrial laser scanning – testing for bias in a 3D virtual environment. *Agricultural and Forest Meteorology*.

*__Abegg, M.__, Bösch, R., Schaepman M.E., & Morsdorf F. (under Review). Impact of Beam Diameter and Scanning Approach on Point Cloud Quality of Terrestrial Laser Scanning in Forests. *IEEE Transactions on Geoscience and Remote Sensing.*

*Content directly related to this thesis.

*Content directly related to this thesis.

Conference Talks

Abegg, M. (2018). Terrestrisches Laserscanning für Waldinventuren. *Fernerkundung und Wald – Update Grundlagen und Werkzeuge. 16 November. Birmensdorf, Switzerland.*

Abegg, M. (2017). Terrestrial Laser Scanning for Forest Inventories – Influence of laser beam properties on point cloud quality. *CARISMA workshop. 21-23 August. Helsinki, Finland.*

Abegg, M. (2017). Influence of stand parameters and scanner positioning on occlusion. *TLS RCN Meeting. 1 March. London, UK.*

Abegg, M. (2016). Forest inventory and TLS. *Tree data and modelling workshop. 7 - 9 June. Tampere, Finland.*

Abegg, M. (2016). TLS Forschung im LFI. *Jahrestreffen ARE-Agroscope-BAFU-BFS-WSL. 2 June. Neuenburg, Switzerland.*

Abegg, M. (2016). TLS for Forest Inventories. *WSL/SLF – RSL Remote Sensing Workshop. 9 December. Birmensdorf, Switzerland.*

Acknowledgements

First of all, I would like to thank Urs-Beat Brändli and Ruedi Bösch who made this PhD possible. Urs-Beat gave me the freedom to dive into research and work flexibly for the NFI and the PhD. Ruedi always found solutions, whenever I had any (!) kind of software problem. Additionally, he patiently supported me in programming, explaining me concepts of software development and discussing possible solutions with me whenever needed. I would like to thank Felix Morsdorf for supporting my ideas of research, guiding me through my PhD and giving our papers the final touch. I would like to thank Michael Schaepman for accepting a forester in the remote sensing world and keeping my PhD focussed. I would like to thank Ross Purves for his support and advices for my PhD. Furthermore, I would like to thank all my colleagues in the Swiss NFI team for their support over these years and the RSL team for its warm welcome at the University and for many interesting discussions on remote sensing.

I would like to thank Daniel Kükenbrink and Jonas Böhler for keeping me company through our PhDs, our discussions and giving me insights in remote sensing. I would like to thank Natalia Rehush for our fruitful exchange on the subject of laser scanning and her supportive attitude towards my research ideas. Furthermore, I would like to thank my other office mates at RSL: Fabian, Marta, Carla, Liv, Isabelle, Marius. It was always a pleasure to be part of their team as well.

A great and warm thank goes to my mother Susanne, my sister Maria and my mother in law Edith, who kept our family running in times of excessive workload. What would I (we) have done without them? And a special thank (high five!) goes to my kids Oliver and Pascal, sharing beautiful moments with me, keeping me rooted in real life and sometimes even listen to my research (and other nerdy) ideas.